Representation of Vector-Controlled Induction Motor Drive Load in Electro-Magnetic Transient and Positive Sequence Transient Stability Simulators

by

Yuan Liu

A Dissertation Presented in Partial Fulfillment
of the Requirements for the Degree
Doctor of Philosophy

Approved July 2016 by the
Graduate Supervisory Committee:

Vijay Vittal, Chair
John Undrill
Raja Ayyanar
Jiangchao Qin

ARIZONA STATE UNIVERSITY

August 2016

ABSTRACT

This dissertation presents innovative techniques to develop performance-based models and complete transient models of induction motor drive systems with vector controls in electro-magnetic transient (EMT) and positive sequence transient stability (PSTS) simulation programs. The performance-based model is implemented by obtaining the characteristic transfer functions of perturbed active and reactive power consumptions with respect to frequency and voltage perturbations. This level of linearized performance-based model is suitable for the investigation of the damping of small-magnitude low-frequency oscillations. The complete transient model is proposed by decomposing the motor, converter and control models into *d-q* axes components and developing a compatible electrical interface to the positive-sequence network in the PSTS simulators. The complete transient drive model is primarily used to examine the system response subject to transient voltage depression considering increasing penetration of converter-driven motor loads.

For developing the performance-based model, modulations are performed on the supply side of the full drive system to procure magnitude and phase responses of active and reactive powers with respect to the supply voltage and frequency for a range of discrete frequency points. The prediction error minimization (PEM) technique is utilized to generate the curve-fitted transfer functions and corresponding bode plots. For developing the complete drive model in the PSTS simulation program, a positive-sequence voltage source is defined properly as the interface of the model to the external system. The *dc*-link of the drive converter is implemented by employing the average model of the PWM converter, and is utilized to integrate the line-side rectifier and machine-side inverter.

Numerical simulation is then conducted on sample test systems, synthesized with suitable characteristics to examine performance of the developed models. The simulation results reveal that with growing amount of drive loads being distributed in the system, the small-signal stability of the system is improved in terms of the desirable damping effects on the low-frequency system oscillations of voltage and frequency. The transient stability of the system is also enhanced with regard to the stable active power and reactive power controls of the loads, and the appropriate VAr support capability provided by the drive loads during a contingency.

ACKNOWLEDGMENTS

I would like to first and foremost express my sincerest gratitude to my advisor, Dr. Vijay Vittal, whose encouragement, guidance and support have motivated me to make significant progress on the research and complete my dissertation. I also attribute the success of my research work to Dr. John Undrill for his extensive input on both my research topic and the practical issues associated with the phenomenon. I also want to express my gratitude to Dr. Raja Ayyanar and Dr. Jiangchao Qin for the time and consideration in being members of my graduate supervisory committee.

I especially want to thank my parents in China and my wife Tongxin Zhu for their support and understanding of my higher education. I also would like to thank my friends who encouraged me.

TABLE OF CONTENTS

Page

CHAPTER Page

CHAPTER Page

LIST OF TABLES

Table Page

LIST OF FIGURES

Figure Page

Figure Page

Figure Page

Figure Page

Figure Page

NOMENCLATURE

A/C	Air-conditioner
ac	Alternating current
AI	Artificial intelligence
CFLs	Compact fluorescent lamps
dc	Direct current
D-STATCOMs	Distribution static VAr compensators
DTC	Direct torque control
DTFC	Direct torque (and flux) control
DPC	Direct power control
DSA	Dynamic security assessment
DSP	Digital signal processing
EMTDC	Electro-magnetic transients including direct current
EMTP	Electro-magnetic transients program
EMT	Electro-magnetic transient
EPCL	Engineer program control language
EPRI	Electric Power Research Institute
ETMSP	Extended transient/midterm stability program
FACTS	Flexible *ac* transmission system
FC	Fuel cell
FIDVR	Fault-induced delayed voltage recovery
FOC	Field oriented control

GE	General Electric
HVDC	High voltage direct current
LBNL	Lawrence Berkeley National Laboratory
LSE	Least square estimation
LTI	Linear time invariant
MRAS	Model reference adaptive system
MVA	Mega volt ampere
MVWG	Modeling and validation work group
MW	Mega watt
PEM	Prediction error minimization
PLL	Phase locked loop
PSCAD	Power systems computer aided design
PSLF	Positive sequence load flow
PSS/E	Power system simulator for engineering
PSTS	Positive sequence transient stability
P-O-W	Point-on-wave
PWM	Pulse width modulation
PV	Photovoltaic
R&D	Research and development
RTDS	Real time digital simulator
SPIM	Single phase induction motor
SPWM	Sinusoidal pulse width modulation

SSAT	Small signal analysis tool
SVC	Static VAr compensator
TSAT	Transient security assessment tool
UDM	User defined model
UPS	Uninterruptible power supply
VSDs	Variable speed drives
VVVF	Variable voltage variable frequency
WECC	Western Electricity Coordinating Council
ω_e	Electrical speed of rotating reference frame
ω_m	Mechanical speed of rotor shaft
ω_r	Electrical speed of rotor shaft
ω_{sl}	Slip frequency in rad/s
ω_B	Base angular frequency
θ_e	Angular displacement between stationary d^s-q^s axes and rotating *d*-*q* axes reference frames
σ_s	Intermediate variable defined by (3.46)
ψ_{dm}, ψ_{qm}	Air-gap flux linkages relative to rotating *d*-*q* axes
ψ_{ds}, ψ_{qs}	*d*-*q* axes stator flux linkages in rotating reference frame
ψ_{dr}, ψ_{qr}	*d*-*q* axes rotor flux linkages in rotating reference frame
ψ_r	Amplitude of rotor flux linkage
$\phi_{pv}\ \phi_{qv}\ \phi_{pf}\ \phi_{qf}$	Relative phase shifts of measured *P*-*Q* perturbations compared to *V*-*f* perturbations

$A_{pv}\ A_{qv}\ A_{pf}\ A_{qf}$	Relative magnitudes of measured *P*-*Q* perturbations compared to *V*-*f* perturbations
B_c	Susceptance of *dc*-link capacitor
C	Capacitance of *dc*-link capacitor
d_a, d_b, d_c	Three-phase instantaneous duty ratios
e_d, e_q	*d*-*q* axes internal voltages of the PSLF voltage source interface
e_r, e_i	Real and imaginary components of grid-side voltage of the PSLF voltage source interface
f_a^s, f_b^s, f_c^s	Instantaneous *a*- *b*- *c*- phase electrical variables such as voltage, current or flux
$\overline{\mathbf{f}_{\mathbf{dq}}^{\mathbf{s}}}, \overline{\mathbf{f}_{\mathbf{dq}}}$	Space vectors of electrical variables in the form of complex number in stationary d^s-q^s axes and rotating *d*-*q* axes reference frames
$\mathbf{f}_{\mathbf{abc}}^{\mathbf{s}}, \mathbf{f}_{\mathbf{dq}}^{\mathbf{s}}, \mathbf{f}_{\mathbf{dq}}$	Electrical variables in the form of matrix in stationary *a*-*b*-*c* phases, stationary d^s-q^s axes and rotating *d*-*q* axes reference frames
f_p (or ω_p)	Perturbation frequency in Hz or rad/s
G	Inverter gain
H	Inertia constant
i_{as}, i_{bs}, i_{cs}	*ac*-side three-phase currents of converter (also known as three-phase stator currents of the inverter-supplied motor)
i_{ds}, i_{qs}	*d*-*q* axes stator currents in rotating reference frame

i_{dr}, i_{qr}	*d*-*q* axes rotor currents in rotating reference frame
i_{tr}, i_{ti}	Real and imaginary components of grid-side current of the PSLF voltage source interface
$\overline{\mathbf{i}_{\mathbf{fe}}^{\mathbf{s}}}$, $\overline{\mathbf{i}_{\mathbf{fe}}}$	Drive *ac*-side line currents in the forms of complex number in stationary and rotating reference frames
i_{fed}, i_{feq}	Drive grid-side *d*-*q* axes line currents
i_{dc}	*dc*-link input current
i_l	*dc*-link load current (*dc*-link output current)
$\mathbf{K_{r1}}$	*abc*-to-*dq* transformation matrix
$\mathbf{K_{r2}}$ (or $\mathbf{K_p}$)	*dq*-to-*abc* transformation matrix
L_{ls}, L_{lr}	Stator and rotor leakage inductances
L_m	Mutual inductance
L_s	Stator synchronous inductance
L_{src}	Inductance of the PSLF voltage source interface
L_r	Rotor synchronous inductance
L_{fe}	Drive *ac*-side line inductance
R_s, R_r	Stator and rotor resistances
R_{fe}	Drive *ac*-side line resistance
R_{src}	Resistance of the PSLF voltage source interface
T_e	Electro-magnetic torque
T_L	Mechanical load torque
v_{as}, v_{bs}, v_{cs}	*ac*-side three-phase voltages of converter

$v_{as}^*, v_{bs}^*, v_{cs}^*$	Normalized three-phase reference voltages of converter
v_{ds}, v_{qs}	*d-q* axes stator voltages in rotating reference frame
v_{ds}^*, v_{qs}^*	*d-q* axes reference voltages
v_{dr}, v_{qr}	*d-q* axes rotor voltages in rotating reference frame
V_{dc}^*	Reference *dc*-link voltage
V_{dc}	*dc*-link voltage
$\overline{\mathbf{V_{ac}^s}}, \overline{\mathbf{V_{ac}}}$	Grid-side voltage vectors in the forms of complex number in stationary and rotating reference frames
$\overline{\mathbf{V_{fe}^s}}, \overline{\mathbf{V_{fe}}}$	Converter-side voltage vectors in the forms of complex number in stationary and rotating reference frames
V_{acd}, V_{acq}	Grid-side *d-q* axes voltages in rotating reference frame
v_{acd}, v_{acq}	Grid-side *d-q* axes voltages of the PSLF voltage source interface
V_{fed}, V_{feq}	Converter-side *d-q* axes voltages in rotating reference frame
X_{src}	Reactance of the PSLF voltage source interface

Chapter 1. INTRODUCTION OF RESEARCH

1.1 Background

The art of load representation in power systems for dynamic performance analysis has been a topic of research interest for decades. In performing accurate power systems studies, models must be systematically developed for all pertinent components, including generating units, transmission systems and VAr supporting devices, distribution equipment and load devices. Much attention has been paid to the generation and transmission system modeling. Recent industrial testing results [1] reveal that precise load representation is becoming more and more essential for system stability analysis. Generic models of dynamic loads have to be proposed to investigate the active and reactive power consumptions in response to different categories of disturbances in a multi-machine power system. The most commonly considered disturbances in the power systems are fault-induced voltage depression and low-frequency oscillation.

Fault-induced voltage depression is a phenomenon of propagation of low voltage over the system caused by single-phase or multi-phase short circuit contingency at a given location. The depth of the voltage magnitude depression depends on the electrical distance of the investigated area to the fault location, and it also depends on the strength of external grid. Typical voltage depression persists from several cycles to tens of cycles [1]. Recent research efforts also discovered that irreversibly stalled single-phase induction motors could prolong the voltage depression and decelerate the voltage recovery [1] – [3].

The ability of synchronous machines in an interconnected system to remain in synchronism after being subjected to a small disturbance is known as small-signal stability [4]. The small-signal stability depends on the ability to maintain equilibrium between

electro-magnetic and mechanical torques of each synchronous machine connected to the system. The change in electro-magnetic torque of a synchronous machine following a perturbation or disturbance can be resolved into two components, which are a synchronizing torque component in phase with rotor angle deviation and a damping torque component in phase with speed deviation. The larger synchronizing torque the machine is able to provide, the smaller damping torque it will result in, and vice versa. Insufficient synchronizing torque results in aperiodic instability, whereas insufficient damping torque engenders low-frequency oscillations [5].

Low-frequency oscillations are mostly generator rotor angle oscillations ranging between 0.1 - 2.0 Hz [5], [6]. The rudimentary cause of electrical power oscillations are the unbalance between power demand and power generation in one period. Oscillations are classified as local mode if a small group of adjacent generators (sometimes a single generator) oscillates with respect to the rest of the system. Typical local mode frequencies occur in the range from 0.7 to 2.0 Hz [6]. Oscillations can also occur between swing generating units in one part of the system and machines in other parts. This type of oscillation is referred to as inter-area oscillation, which usually has a frequency range of 0.1 to 0.8 Hz [6]. Additionally, the actions of generation controllers such as exciters and governors can also induce low-frequency oscillations in some situations [4].

Modeling of loads is somewhat complicated because a typical load bus is composed of a large number of devices such as fluorescent and incandescent lamps, refrigerators, heaters, compressor motors and so on. The fractional composition of the load components is also different at each specific load bus and sometimes is seasonal. The class of loads embraces industrial, commercial and residential usage [7]. Aggregation and simplification

are two primary rules for load representation in power systems stability analysis. Traditionally load models are classified into two broad categories: static models and dynamic models [4], [7].

A static load model represents the characteristics of the load, mainly active and reactive power withdrawal, as algebraic functions of bus voltage magnitude and frequency at any instant of time. Two generic models of static loads, called exponential model and polynomial model, are classical representations [4]. Considering the frequency dependency, the exponential model can be expressed by (1.1) and (1.2) while the polynomial model (also known as *ZIP* model) can be given by (1.3) and (1.4). A combination of these two models forms a general load model used in extended transient/midterm stability program (ETMSP) released by Electric Power Research Institute (EPRI) [4], [7], [8].

$$P_{ex} = P_0 \left(V / V_0 \right)^{np} \left(1 + K_{pf} \Delta f \right) \tag{1.1}$$

$$Q_{ex} = Q_0 \left(V / V_0 \right)^{nq} \left(1 + K_{qf} \Delta f \right) \tag{1.2}$$

$$P_{zip} = P_0 \left[p_1 \left(V / V_0 \right)^2 + p_2 \left(V / V_0 \right) + p_3 \right] \left(1 + K_{pf} \Delta f \right) \tag{1.3}$$

$$Q_{zip} = Q_0 \left[q_1 \left(V / V_0 \right)^2 + q_2 \left(V / V_0 \right) + q_3 \right] \left(1 + K_{qf} \Delta f \right) \tag{1.4}$$

where P and Q are active and reactive components of the load when the bus voltage magnitude is V. The subscript 0 indicates the values of power and voltage magnitude at the initial steady state operating condition.

Static models reflect the instantaneous power drawn by the load at a specific time instant. The power is not associated with the previous behavior of the electrical variables.

Nevertheless, there are hundreds of electrical components in the power system exhibiting inductive or capacitive characteristics. To accurately reproduce the dynamics of electrical components that involve differential equations the dynamic model of the associated device has to be utilized. Studies of inter-area oscillations, voltage stability, and long-term stability also require the utilization of dynamic modeling. Typical dynamic load components include three-phase and single-phase induction motors, discharging lighting and other such devices. Practically, motor loads consume 60% to 70% of the total supplied energy [4]. Hence, the dynamics of motors must be considered in characterizing the transient behavior of composite loads. The Western Electricity Coordinating Council (WECC) proposed a widely recognized composite load configuration incorporating static loads, dynamic motors and electronic loads [9], [10]. The schematic of the WECC composite load is shown in Figure 1.1.

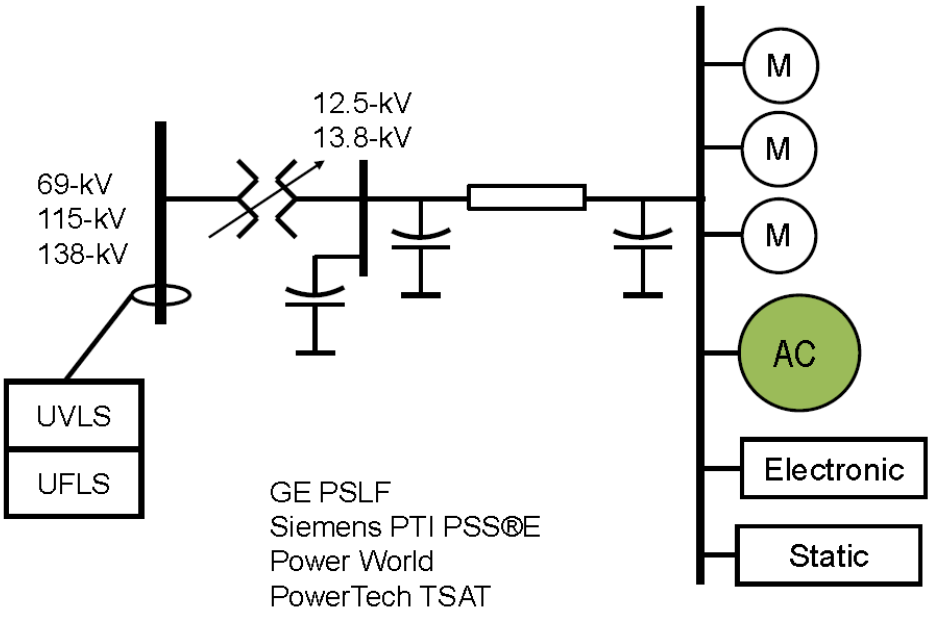

Figure 1.1 WECC Composite Load Model [9]

The dynamic transfer functions of three-phase induction motors in the positive sequence transient stability (PSTS) simulators have been repeatedly examined and widely understood in previous research work [10], [11]. The emergent technological revolution in semiconductor manufacturing has been rendering a new blueprint for the next-generation power systems, in which generating units and customer loads are broadly driven by electronic converters. According to the estimation of the EPRI, almost 70% of electricity in the U.S. flows through power electronic converters [12].

Contemporarily, with the growing penetration of renewable generation resources the stability and reliability related issues of power systems are becoming more complicated than forty years ago when the majority of electricity generation was derived from conventional generators. Nowadays, power electronics are widely used as an intermediate power conversion stage for wind farms, photovoltaic (PV) and fuel cell (FC) energy systems. Power electronics technology is also thriving in transmission infrastructures and propelling the development of high voltage dc (HVDC) transmission and the flexible *ac* transmission system (FACTS). At the user end, the application of power electronics include *dc* and *ac* regulated power supplies, uninterruptable power supply (UPS) systems, distribution static VAr compensators (D-STATCOMs), electronic controlled harmonics filters, solid state *dc* and *ac* circuit breakers, high-efficiency lighting systems (such as electronic-based compact fluorescent lamps (CFLs) and solid state LED lamps), and electronic motor drive systems.

Significant research efforts have be directed towards the design and optimization of wind and solar generation, HVDC, and FACTS controls. On the contrary, less attention has been directed towards the technological advancements at the end of the electricity

supply chain, in which the traditional direct-connected induction motors are being gradually displaced by high-efficiency converter-driven motors. As mentioned above, high-power industrial motors (such as oil compressors, large fans and pumps) represent the majority of electricity energy consumption in comparison to other forms of consumptions such as lighting and heating. Most of the industrial pumps and fans are used for control of fluid flow. It is reported that nearly 97% of such high-power traditional machines operate at fixed speed, while only 3% of them are driven by variable frequency converters [13]. In order to constantly adjust flow volume, mechanical processes such as throttling and valve controls need to be deployed to tighten or relax the fluid outlets, which will increase loss of energy in heat and friction. Being equipped with a variable frequency drive, a given motor can be commanded to pump the fluid at variable flow rate with full throttle opening and thus transport the desired amount of fluid. The efficiency could be raised by 30% at light load condition [13].

The art and science of control design for motor drives has evolved for decades. It is known that four major categories of control techniques that either have been commercialized in the industry or are being optimized in the laboratories. The open-loop V/f scalar control [14], [15], invented early in 20th century, has gradually become obsolete even though it still is utilized in some small-size residential motors. The advent of vector or field-oriented control [16] – [19] in 1971 and direct torque control (DTC) [20] – [23] in 1986 led to a new era of prosperity in the industrialization of modern high-performance *ac* drives. These two types of control methods are now being widely used in high-power drive systems and are also being implemented in medium- or low- power areas. In the 21st century, based on the development of artificial intelligence (AI) technology and modern

control theory, various adaptive-control techniques [24] have emerged. The AI control resolves the parameter volatility in real control system and it is adaptive to non-linear systems. Unfortunately, it results in big complexities for power systems engineers to incorporate this feature into simulation software because of the lack of AI models in traditional power systems simulation programs.

As engineers welcome the advances in electronic drive commercialization, a seemingly-unresolved question is posed to power systems engineers: How do we model the *ac* drives that are suitable for power systems analysis? This question is partially answered by power electronics engineers because they declare that the *ac* drives could be modeled into their device-level simulation packages such as PSPICE, PLECS and Matlab/Simulink. For the purpose of research and development (R&D), the schematics of *ac* drive circuits are usually validated in these above simulation tools. In such device-level simulations, the supply source is usually equivalenced as an infinite bus or controllable voltage source to trace the dynamic performance of the system under steady state or small disturbance. In realistic power systems studies, all electrical components are topologically interconnected to each other through the power grid. Disturbances applied to one component could alter the dynamic behaviors of the others. In the middle of 1970s, several dedicated efforts led to the development of a three-phase electro-magnetic transient program (EMTP) [25] that uses a simulation time step of several microseconds to dozens of microseconds. Commercial EMTP-level software includes EMTP/ATP, PSCAD, and EMTP-RV. The EMTP tool is primarily designed for three-phase or *dc* power systems simulations. With such a small time step, the EMTP simulator is capable of simulating the pulse gating of semiconductor switches, which enables the detailed modeling of the *ac*

drive. Nevertheless, simulating large-sized power systems with tens of *ac* drives would be a big challenge because it is time consuming to set up the circuits and it will take an unacceptably long time to run the simulations because of the small time step required.

The positive sequence transient stability (PSTS) simulators are extensively utilized for large-scale power system simulations in the industry [10]. Using a time step in the order of milliseconds, systems with thousands of buses are simulated within a reasonably short time. Commercial PSTS programs include PSS/E, PSLF, DSA Tools and PowerWorld. Assuming that *ac* drive models can be incorporated in the PSTS programs, it is conceivable that the simulation for next-generation power grids with thousands of complex dynamic loads will no longer be a dream.

1.2 Major Objectives of the Research

As mentioned in Section 1.1, the vector control and DTC are the two most prevalent control techniques that are widely accepted in present industrial applications. In this research, only vector control is considered because for DTC there is no effective approach to eradicate the switching logics, which makes it impractical to be modeled in PSTS program.

A three-phase double-sided PWM converter [14] is considered as the investigated converter structure. The entire drive system includes line-side rectifier and machine-side inverter, and is operated in motoring mode. The vector-controlled drive systems for three-phase induction motors are designed and validated in PSCAD [26]. On the machine-side, the rotor flux oriented control is a classical type of vector control for the inverter controllers. On the line-side, the line voltage vector is oriented; the *dc*-link voltage and line currents

are controlled to make the rectifier operate at desired power factor, ideally at unity power factor [14].

The average model of the three-phase sinusoidal PWM (SPWM) converter is introduced in the design of drive systems [28]. There are two significant reasons to consider the average model instead of a detailed switching model. As multi-level converters are becoming more and more popular, the generated three-phase voltages on the *ac* sides of converters are approximately sinusoidal. With appropriate current controls, the line-side and machine-side currents also approximate to sine waves. These features could be created by using a simplified average model of the converter. Given the average model, the mathematical relations between *ac*- and *dc*- side electrical variables are associated with each other through algebraic equations, and this facilitates the build-up of the system block diagrams.

Once the line-side and machine-side converter controls are established, sinusoidal perturbations are applied on terminal voltage and frequency of the *ac* drive system to obtain the perturbations of power consumption over a range of discrete frequency points. The magnitude and phase responses of perturbed active and reactive powers with respect to voltage and frequency perturbations are monitored and recorded. Using this method, a series of power-over-voltage and power-over-frequency responses are replicated and stored. Four continuous-time transfer functions characterizing the sensitivities of active and reactive powers to voltage and frequency are obtained using prediction error minimization (PEM) techniques [29]. The performance-based model of the *ac* drive systems is developed by programming these four transfer functions in association with voltage (or current) source electrical interface into the PSTS dynamic simulation routines.

This class of drive model is then used to investigate its impact on low-frequency oscillations.

The transient model of the vector-controlled *ac* drive is also implemented to investigate its dynamic responses to fault induced depression on voltage magnitude. The transient model implemented in the PSLF [10] is developed based on separate controls on the *d*- and *q*- axis. The final equivalent circuit of this model in PSLF is represented as a Thévenin voltage source, where the internal complex *d-q* axes voltage variables are manipulated by controllers to generate unity power factor.

1.3 Organization of the Dissertation

The dissertation is organized in six chapters. Chapter 1 gives a basic introduction to the research. This chapter presents the background, description of previous work and major objectives of the research.

Chapter 2 presents the literature review relating to classical and recent load modeling, and revolutions in the technologies of *ac* drives.

Chapter 3 deals with the mathematical development and simulation studies of three-phase detailed *ac* drive systems in EMT-level software packages.

Chapter 4 provides the mathematical development and simulations of performance-based model in the PSTS simulation programs.

Chapter 5 details the mathematical derivation of the transient model of drive system in PSTS simulation programs and demonstrates respective simulation cases.

The conclusions and findings of the work are provided in Chapter 6. Ideas for future work are also given in this chapter.

Chapter 2. LITERATURE REVIEW

The early exploration of load representation in power system stability studies can be traced back to the early 1970s. Reference [30] published in early 1980s summarizes the research efforts on load components characteristics until the late 1970s. The authors of [30] emphasize the importance of load composition and validation with field test data. According to the results presented in [30], the static load characteristics indicated by slopes of *dP/dV*, *dP/df*, *dQ/dV* and *dQ/df* are season and location dependent. The composition of load is also time varying. As mentioned in [30], characteristics of induction motor loads are sensitive to shaft mechanical load torque and are highly frequency dependent.

The IEEE Task Force on Load Representation for Dynamic Performance published a broadly cited journal paper in 1993 [7]. This publication reviewed the state-of-the-art of dynamic load modeling. As a supplement to [30], the authors of [7] considered frequency dependency in the polynomial and exponential formation of load representation. The standard static load model used by EPRI is also provided in [7]. The induction motor load in [7] is explicitly represented by T-shaped equivalent circuits, possibly considering mechanical dynamics and rotor or stator flux dynamics. In [7], the authors have also listed several constraints on the use of static load models in first swing transient stability analysis and investigations of inter-area modes of oscillations. The exploitation of this static model in voltage stability analysis also drew incorrect conclusions [7]. The authors of [7] also provided concise description of characteristics of various load components in a composite load model. In [7], two generic methods to obtain load model parameters were also proposed. The first option is direct measurements of voltage and frequency sensitivity of load P and Q at representative substations. The demerits of this method included

inconvenience to represent loads at different locations and inability to trace seasonal or yearly load change. The second choice was to consider the characteristics of each individual load component. The customized model was finalized by knowing the composition percentage. The advantage of this method was that the composition percentage was the only variable to the exclusion of different systems and conditions. The disadvantage was the composition percentage was usually difficult to obtain.

The same group of devoted researchers published another progress paper in 1995 documenting currently adopted standard load components for use in dynamic performance simulations [8]. In this paper, the authors sketched the prototype of the composite load structure and detailed the modeling mechanism of several included components. The authors also proposed that a satisfactory composite load model was supposed to incorporate the static load model, small and large induction motors, synchronous motors, discharge lighting, transformer saturation model, and load tap changing transformers [8]. Among these different load components, the authors stressed the importance of the modeling detail for induction motors. In the simulation of oscillation damping and motor reacceleration, the models accounting for rotor flux dynamics necessitated motor speed to automatically track system frequency, which demonstrated transcendent performance over the steady-state equivalent circuit model. The authors of [8] also conceptually raised an alternative to represent the induction motor through sensitivity analysis.

In 2001, an interim composite load model [11] containing merely static load model and dynamic induction motors was implemented to investigate system low-frequency power damping with respect to different levels of induction motor loads over the system. It was concluded from the implementation and simulation that the percentage of induction

motor loads was a dominating factor affecting the system damping. The inertia and power ratings of motors were influential, but not determining factors to calibrate the damping capability. This interim load model was also blamed for its exclusion of other types of load components.

In the early 1990s, more research efforts were dedicated to exploring the cause of fault-induced delayed voltage recovery (FIDVR) phenomenon [1], [2]. The authors of [1] believed that the FIDVR problem was inflicted by stalled single-phase induction motors that encountered voltage depression at the terminal. This finding was endorsed and substantiated by the field observation data at the Riverside 138 kV substation located in the West Miami area when subjected to a bolted three-phase fault six miles away from the observation point [2]. According to the slip-torque curve of the single-phase induction motor, if the voltage dropped below 60% of the nominal value, even the peak electro-magnetic torque could not overcome the mechanical torque, causing the rotor to remain stationary and locked. Several remedial actions to FIDVR problems were proposed in [1] including dropping stalled motor loads during fault, initiating fast fault clearing, and expanding the transmission corridor to minimize grouping of prone-to-stall air-conditioner loads. Recent explorations on the motor stalling issues discovered that the stalling of the small induction motors in residential air-conditioners was dependent not only on the depth and duration of the supply voltage dip, but also on the point on the supply voltage wave at which the dip was initiated [3]. Dynamically a small-size motor could stall in a few cycles. The implementation of a single-phase induction motor model in [3], gave convincing simulation results. This model however was developed for three-phase EMT programs. It was not desirable for system operation engineers to perform batch simulations on a large-

scale power system. A load modeling progress paper was completed by Kosterev and Meklin in 2006 [31]. This paper urged the accurate representation of air-conditioner compressors into the composite load model used for simulating the WECC interconnected system. The performance-based single-phase motor load exhibited relatively approximate dynamic behaviors compared to field test data, and it was programmed into the composite load structure in several PSTS simulation programs such as PSS/E and PSLF. The contemporary composite load structure was finalized in 2008 [32]. In terms of the authors' statement, this refurbished model was a great improvement over the previously mentioned interim load model. Some other efforts [33], [34] were focused on integrating the rotor dynamics of single-phase motor into the PSTS simulation program. Authors of [33] and [34] introduced a dynamic phasor model for single-phase motors. This model was not widely used because of occasional stability problems.

According to a technical report [35] released by Lawrence Berkeley National Laboratory (LBNL) in 2010, more and more large industrial motor drive systems were coupled with power electronic converters, which assured motor loads to achieve a low-voltage ride-through capability to some extent. The employment of the electronic converter drive gradually penetrated into low-voltage level applications, especially residential single-phase pumps, fans and air-conditioner compressors. Equipped with an electronic drive, prone-to-stall single-phase motors could receive fast-response voltage support from inverter controls and the *dc*-link capacitor [36]. With more and more power electronics load devices emerging in power systems, the traditional beliefs related to system oscillation damping and system transient stability could be reshaped.

According to [12], the Electric Power Research Institute (EPRI) of the USA publicized a statistical report proclaiming that nearly 60%–65% of grid-generated energy in the USA was consumed by electrical motor loads, and 75% of these were pump, fan, and compressor-type motors. Nevertheless, 96% of the motors were directly connected to the grid and operated at constant speed. This data yielded encouraging news that there was still significant scope for the commercialization of modern variable speed drives (VSDs). There are several prevailing control techniques for induction motor drives, including open- or closed- loop scalar control, vector control, direct torque and flux control, and adaptive control.

The most straightforward scalar control was the open loop Volts/Hz control [14]. A speed command was fed into the controller to ramp up the motor speed and create a growing reference voltage command. The stator flux was maintained unchanged during the reference voltage ramp-up and was weakened after the reference voltage saturated. Since there was no speed control loop in this simple controller, the rotor speed could not be regulated if load torque increased. This problem was combated by adding a speed droop corrector to the control.

An improved Volt/Hz controller that introduced closed-loop speed control and slip regulation was proposed in [37]. The demerit of this control was the flux drift caused by stator voltage variation because of the absence of closed-loop flux control.

Two other advanced scalar controls were speed-controlled inverter drive with closed-loop torque and flux controls, and voltage-fed current-regulated inverter drive with closed-loop torque and flux controls [14], [15]. The former inverter drive had an outer speed control loop and an inner torque control loop. The output of the torque controller

generated a reference frequency for the inverter. The separate flux controller generated the reference voltage. The latter inverter drive contained outer flux and torque controls and inner current control. The outputs of the flux and torque controllers constituted reference three-phase current commands that were fed into inner current control loop. The drawback of both the drives was the sluggish torque response caused by coupling effects at the reference voltage or current during the frequency ramp-up period. This problem was explained and reconciled in [15].

Field oriented control (FOC), also termed vector control, was invented at the beginning of 1970s, and has been extensively utilized by the *ac* drive industry. Based on whether the speed sensor exists at the shaft end, the vector control includes sensor control and sensorless control. Based on the class of field orientation, the vector control could be divided into rotor flux oriented control and stator flux oriented control. Moreover, the rotor flux oriented control could be further sub-divided into direct (or feedback) and indirect (or feedforward) rotor flux oriented controls [14]. The conventional sensor control required a measured rotational speed from motor shaft as a signal fed to the speed control loop. It was also possible to estimate the speed signal from motor terminal voltages and currents with the aid of DSP chips [38]. The authors of [39] described a novel model-reference adaptive system (MRAS) to estimate the motor speed from measured terminal voltages and currents. The extended Kalman filter was employed to identify the motor speed and rotor flux based on the measurements of stator currents and *dc*-link voltage [40]. Rotor flux oriented control was more widely used than stator flux oriented control. With this type of control, the *d*-axis of the synchronously rotating reference was artificially aligned with the rotor flux vector [19]. Similarly, the *d*-axis of the rotating reference was oriented in the same

direction as the stator flux vector for the stator flux oriented control [41]. Specific decoupling compensation designed to minimize the coupling effects in the stator flux controller was necessitated to improve the dynamic performances of stator flux oriented control [41]. In contrast, for rotor flux oriented control, there were no coupling effects in the rotor flux controller [14], [19]. There were two subcategories of rotor flux oriented control. The difference between these two controls was the method to obtain the speed of the synchronously rotating reference frame. The direct rotor flux oriented control computed the speed by measuring terminal voltages and utilizing the related flux linkage equations [17]. In the indirect rotor flux oriented control, the synchronous speed was the summation of the estimated slip frequency and measured rotor speed. The slip frequency was estimated with the help of measured currents and current-slip relation [16].

Another advanced scalar control invented in the mid-1980s was direct torque (and flux) control (DTFC or DTC) [42]. The DTC scheme employed a hysteresis-band width controller to create an optimal switching logic table for the PWM inverter. The desirable voltage vector was procured by different combinations of switching operations based on the output of flux and torque hysteresis-band controllers. The voltage vector was used to change the stator flux and electro-magnetic torque to the extent that the magnitudes of stator flux and torque were held constant within a reasonable bandwidth. With this type of control, the rotor flux remained constant. The controller design was simplified because of the absence of feedback current controls. The torque response was also faster than vector control.

A linear control system with invariant plant parameters could be handily designed with classical techniques. However, in some industrial applications, the system parameters

could change substantially from offline to online operation. This situation required the control system to include parameterization, self-tuning, and tracking capability [43]. For special induction motor drives, such as escalator drives, the inertia of the electric motor with mechanical load attached or detached could be largely different. Under this circumstance, adaptive control could be deployed to operate the system at different working conditions. The adaptive control techniques could be generally classified as self-tuning control, MRAC, sliding mode or variable structure control, expert system control, fuzzy control, and neural control [13], [14].

The above discussions covered reviews of control design on machine-side inverter. There were also several advanced control schemes for the line-side controllable PWM rectifier. The decoupled control of active and reactive power based on the phasor diagram employed PI controllers to establish *dc*-link voltage, active power and reactive power control loops [44]. In contrast, the direct power control (DPC) introduced hysteresis-bandwidth modulator and switching table logic module to substitute the PI controller and acquired similar power and voltage controls [45]. Comparing these two control schemes, the decoupled control manifested itself with less sampling frequency; the DPC scheme benefitted from its fast response and the absence of decoupling compensation.

Chapter 3. THREE-PHASE EMT DRIVE MODEL

3.1 Introduction

The effort devoted to the development of vector-controlled drive system for induction motors in three-phase EMT programs is worthy before implementing the system into positive-sequence simulation programs. The characteristics of the three-phase control system will be thoroughly investigated and validated.

In this chapter, the design of the detailed vector control system of three-phase induction motor drives will be elaborated in a progressive manner. First, the theory of reference frame orientation will be introduced. Following that, the dynamic differential equations related to the electrical variables of a single-cage induction motor will be formulated. The derivation of these differential equations evolves into the motor model in rotor-flux (or field) coordinates. After the above preparations, the rotor flux oriented control for the machine-side inverter and the vector control for the grid-side rectifier will be devised separately in detail. Finally, the average model of the three-phase PWM converter will be addressed and considered as an appropriate replacement for the switching and gating model of the realistic converter in the pursuit of high simulation speed.

3.2 Understanding the Reference Frame Transformation

For a symmetrical three-phase induction motor system, at any moment, the three-phase stator voltages, currents or flux sum to zero. It also applies to rotor variables. Consequently, the three-phase voltage, current or flux can be expressed in a space vector form [19]. The general expression is given by (3.1) and (3.2).

$$f_a^s + f_b^s + f_c^s = 0 \tag{3.1}$$

$$\overline{\mathbf{f}_{\mathbf{dq}}^{\mathbf{s}}} = f_a^s + f_b^s \cdot e^{j120^\circ} + f_c^s \cdot e^{j240^\circ} \tag{3.2}$$

In which, f_a^s, f_b^s and f_c^s represent instantaneous *a- b- c* phase electrical variables such as voltage, current or flux; $\overline{\mathbf{f}_{\mathbf{dq}}^{\mathbf{s}}}$ represents space vector of electrical variables in the form of complex number in stationary d^s-q^s axes reference frame.

The transformation from stationary d^s-q^s to rotating *d-q* axes frames is depicted in Figure 3.1. According to Figure 3.1, and the transformation from d^s-q^s to *d-q* axes reference frames can be written as (3.3). Combining and expanding (3.1) - (3.3) result in (3.4) – (3.9).

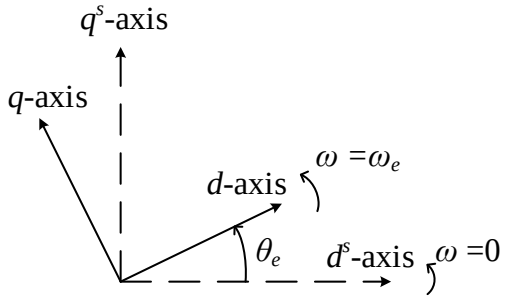

Figure 3.1 Space Vector Diagram of Stationary d^s-q^s Axes and Rotating *d-q* Axes Reference Frames

$$\overline{\mathbf{f}_{\mathbf{dq}}} = \overline{\mathbf{f}_{\mathbf{dq}}^{\mathbf{s}}} \cdot e^{-j\theta_e} \tag{3.3}$$

$$\overline{\mathbf{f}_{\mathbf{dq}}^{\mathbf{s}}} = f_d^s + j \cdot f_q^s = \frac{3}{2} f_a^s + j\left(\frac{\sqrt{3}}{2} f_b^s - \frac{\sqrt{3}}{2} f_c^s \right) \tag{3.4}$$

$$\overline{\mathbf{f}_{\mathbf{dq}}} = f_d + j \cdot f_q = \left(\cos\theta_e \cdot f_d^s + \sin\theta_e \cdot f_q^s \right) + j\left(-\sin\theta_e \cdot f_d^s + \cos\theta_e \cdot f_q^s \right) \tag{3.5}$$

$$\mathbf{f}_{\mathbf{dq}}^{\mathbf{s}} = \begin{bmatrix} f_d^s \\ f_q^s \end{bmatrix} = \begin{bmatrix} \frac{3}{2} & 0 & 0 \\ 0 & \frac{\sqrt{3}}{2} & -\frac{\sqrt{3}}{2} \end{bmatrix} \begin{bmatrix} f_a^s \\ f_b^s \\ f_c^s \end{bmatrix} \tag{3.6}$$

$$\mathbf{f}_{\mathbf{dq}} = \begin{bmatrix} f_d \\ f_q \end{bmatrix} = \begin{bmatrix} \cos\theta_e & \sin\theta_e \\ -\sin\theta_e & \cos\theta_e \end{bmatrix} \begin{bmatrix} f_d^s \\ f_q^s \end{bmatrix} \tag{3.7}$$

$$\mathbf{f}_{\mathbf{abc}}^{\mathbf{s}} = \begin{bmatrix} f_a^s \\ f_b^s \\ f_c^s \end{bmatrix} = \begin{bmatrix} \frac{2}{3} & 0 \\ -\frac{1}{3} & \frac{\sqrt{3}}{3} \\ -\frac{1}{3} & -\frac{\sqrt{3}}{3} \end{bmatrix} \begin{bmatrix} f_d^s \\ f_q^s \end{bmatrix} \tag{3.8}$$

$$\mathbf{f}_{\mathbf{dq}}^{\mathbf{s}} = \begin{bmatrix} f_d^s \\ f_q^s \end{bmatrix} = \begin{bmatrix} \cos\theta_e & -\sin\theta_e \\ \sin\theta_e & \cos\theta_e \end{bmatrix} \begin{bmatrix} f_d \\ f_q \end{bmatrix} \tag{3.9}$$

In the above equations, $\overline{\mathbf{f}_{\mathbf{dq}}^{\mathbf{s}}}$ represents the space vector of electrical variables in the form of a complex number in the stationary d^s-q^s reference frame. $\overline{\mathbf{f}_{\mathbf{dq}}}$ represents the same space vector in the rotating d-q reference frame. $\mathbf{f}_{\mathbf{dq}}^{\mathbf{s}}$ and $\mathbf{f}_{\mathbf{dq}}$ represent the matrix forms of vector in both d^s-q^s and d-q reference frames.

3.3 Dynamic Equations of Induction Motor in Rotor-Flux Coordinates

The three-phase induction motor is modeled at the level of detail that represent electro-magnetic transients. The schematic of the stator and rotor a-b-c phase windings is shown in Figure 3.2. The three stator windings are identical and it is the same for the three rotor windings. The mutual inductances between the stator and rotor coils vary sinusoidally with the angular position of the rotor. The flux linkage differential equation [46] in matrix form is given by (3.10), and the calculation of flux linkages from stator and rotor currents and inductance matrices is presented by (3.11).

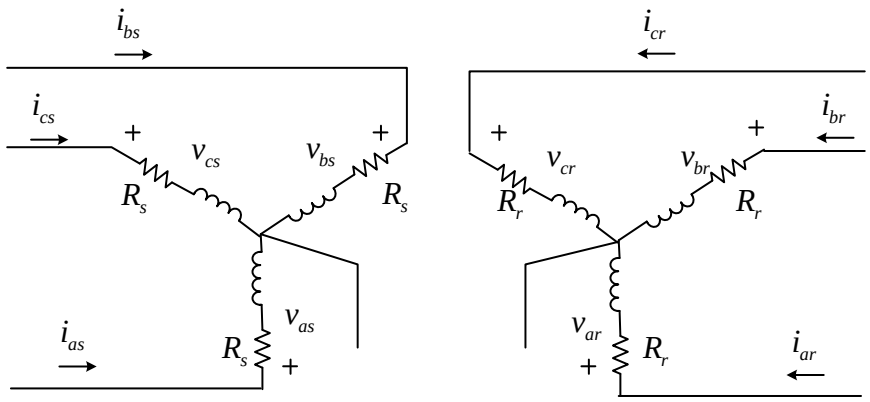

Figure 3.2 Schematic of Stator and Rotor *a-b-c* Phase Windings

$$\begin{bmatrix} \mathbf{v}_{\mathbf{abcs}} \\ \mathbf{v}_{\mathbf{abcr}} \end{bmatrix} = \begin{bmatrix} \mathbf{R}_{\mathbf{s}} & \mathbf{0} \\ \mathbf{0} & \mathbf{R}_{\mathbf{r}} \end{bmatrix} \begin{bmatrix} \mathbf{i}_{\mathbf{abcs}} \\ \mathbf{i}_{\mathbf{abcr}} \end{bmatrix} + \frac{\mathbf{d}}{\mathbf{dt}} \begin{bmatrix} \boldsymbol{\psi}_{\mathbf{abcs}} \\ \boldsymbol{\psi}_{\mathbf{abcr}} \end{bmatrix} \tag{3.10}$$

$$\begin{bmatrix} \boldsymbol{\psi}_{\mathbf{abcs}} \\ \boldsymbol{\psi}_{\mathbf{abcr}} \end{bmatrix} = \begin{bmatrix} \mathbf{L}_{\mathbf{s}} & \mathbf{L}_{\mathbf{sr}} \\ \left(\mathbf{L}_{\mathbf{sr}}\right)^{\mathbf{T}} & \mathbf{L}_{\mathbf{r}} \end{bmatrix} \begin{bmatrix} \mathbf{i}_{\mathbf{abcs}} \\ \mathbf{i}_{\mathbf{abcr}} \end{bmatrix} \tag{3.11}$$

where

$$\left(\mathbf{f}_{\mathbf{abcs}}\right)^{\mathbf{T}} = \begin{bmatrix} f_{as} & f_{bs} & f_{cs} \end{bmatrix} \qquad \left(\mathbf{f}_{\mathbf{abcr}}\right)^{\mathbf{T}} = \begin{bmatrix} f_{ar} & f_{br} & f_{cr} \end{bmatrix} \tag{3.12}$$

In (3.12), **f** denotes **Ψ**, **i** or **v** in (3.10) and (3.11); the *s* and *r* subscripts denote variables and parameters associated with the stator and rotor circuits respectively. $\mathbf{R_s}$ and $\mathbf{R_r}$ represent stator and rotor resistance matrices, both of which are diagonal with equal nonzero elements. It is convenient to define intermediate matrices to transform variables between the *a-b-c* phases and the rotating *d-q* axes reference frame. According to (3.6) - (3.9), the transition matrices are derived to be (3.13a) and (3.13b).

$$\mathbf{K}_{\mathbf{r1}} = \begin{bmatrix} \cos\theta_e & \sin\theta_e \\ -\sin\theta_e & \cos\theta_e \end{bmatrix} \begin{bmatrix} \frac{3}{2} & 0 & 0 \\ 0 & \frac{\sqrt{3}}{2} & -\frac{\sqrt{3}}{2} \end{bmatrix} \tag{3.13a}$$

$$\mathbf{K_{r2}} = \begin{bmatrix} \frac{2}{3} & 0 \\ -\frac{1}{3} & \frac{\sqrt{3}}{3} \\ -\frac{1}{3} & -\frac{\sqrt{3}}{3} \end{bmatrix} \begin{bmatrix} \cos\theta_e & -\sin\theta_e \\ \sin\theta_e & \cos\theta_e \end{bmatrix} \tag{3.13b}$$

$$\mathbf{f_{dq}} = \mathbf{K_{r1}} \mathbf{f_{abc}^{s}} \tag{3.14}$$

$$\mathbf{f_{abc}^{s}} = \mathbf{K_{r2}} \mathbf{f_{dq}} \tag{3.15}$$

Apply the reference frame transformations (3.14) and (3.15) to (3.10) and (3.11) for stator and rotor associated variables. According to the derivation in [46], the formation of flux differential equations in arbitrary rotating reference frame can be written as

$$v_{ds} = R_s i_{ds} - \omega_e \psi_{qs} + \frac{d\psi_{ds}}{dt} \tag{3.16}$$

$$v_{qs} = R_s i_{qs} + \omega_e \psi_{ds} + \frac{d\psi_{qs}}{dt} \tag{3.17}$$

$$v_{dr} = R_r i_{dr} - (\omega_e - \omega_r)\psi_{qr} + \frac{d\psi_{dr}}{dt} \tag{3.18}$$

$$v_{qr} = R_r i_{qr} + (\omega_e - \omega_r)\psi_{dr} + \frac{d\psi_{qr}}{dt} \tag{3.19}$$

The associated flux linkages can be calculated by

$$\psi_{ds} = L_{ls} i_{ds} + L_m (i_{ds} + i_{dr}) = L_s i_{ds} + L_m i_{dr} \tag{3.20}$$

$$\psi_{qs} = L_{ls} i_{qs} + L_m (i_{qs} + i_{qr}) = L_s i_{qs} + L_m i_{qr} \tag{3.21}$$

$$\psi_{dr} = L_{lr} i_{dr} + L_m (i_{ds} + i_{dr}) = L_r i_{dr} + L_m i_{ds} \tag{3.22}$$

$$\psi_{qr} = L_{lr} i_{qr} + L_m (i_{qs} + i_{qr}) = L_r i_{qr} + L_m i_{qs} \tag{3.23}$$

$$\psi_{dm} = L_m \left(i_{ds} + i_{dr} \right) \tag{3.24}$$

$$\psi_{qm} = L_m \left(i_{qs} + i_{qr} \right) \tag{3.25}$$

$$L_s = L_{ls} + L_m \tag{3.26}$$

$$L_r = L_{lr} + L_m \tag{3.27}$$

In the above equations, v_{ds} and v_{qs} denote the stator *d*-*q* axes voltages in rotating reference frame. v_{dr} and v_{qr} denote the rotor *d*-*q* axes voltages in the same frame. The same subscript conventions are also applicable to the currents and flux linkages. L_{ls} and L_{lr} indicate stator and rotor leakage inductances; L_m is the mutual inductance; ω_e and ω_r are electrical speeds of the rotating reference frame and rotor shaft; ψ_{dm} and ψ_{qm} are air-gap flux linkages relative to *d*-*q* axes. The equivalent circuit of this dynamic *d*-*q* model in the synchronously rotating reference frame is presented by Figure 3.3. The electro-magnetic torque can be expressed by the following equations:

$$T_e = \frac{2}{3}\left(\psi_{dm} i_{qr} - \psi_{qm} i_{dr} \right) \tag{3.28}$$

$$= \frac{2}{3}\left(\psi_{dm} i_{qs} - \psi_{qm} i_{ds} \right) \tag{3.29}$$

$$= \frac{2}{3}\left(\psi_{ds} i_{qs} - \psi_{qs} i_{ds} \right) \tag{3.30}$$

$$= \frac{2}{3} L_m \left(i_{qs} i_{dr} - i_{ds} i_{qr} \right) \tag{3.31}$$

$$= \frac{2}{3}\left(\psi_{dr} i_{qr} - \psi_{qr} i_{dr} \right) \tag{3.32}$$

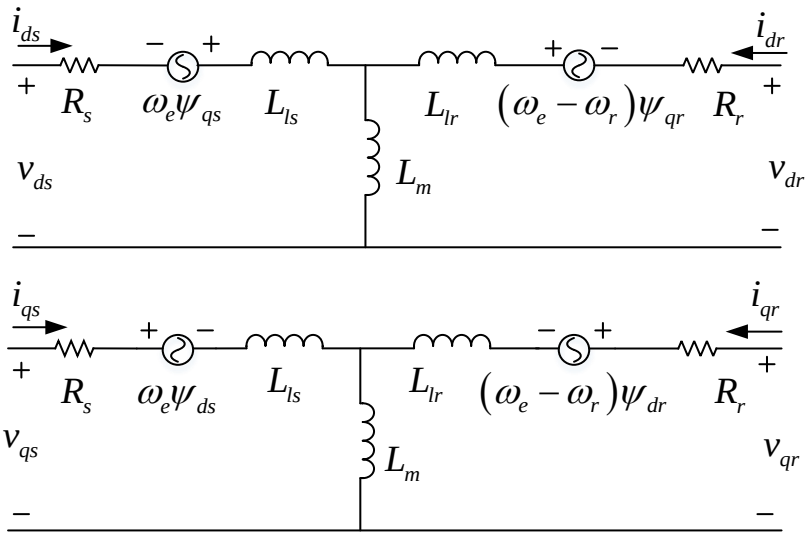

Figure 3.3 Equivalent Circuit of Dynamic *d-q* Axes Motor Model [14]

The speed-torque differential equation representing the mechanical characteristics of the induction motor can be written by

$$T_e = T_L + 2H \cdot \frac{d\omega_r}{dt} \tag{3.33a}$$

in which, T_L is the mechanical load torque of the motor. ω_r is the speed of rotor shaft as mentioned above. H is the inertia constant of the mass attached to the rotor.

The mechanical load torque is assumed to be proportional to the square of the rotor speed, which is given by (3.33b).

$$T_L = k \cdot \omega_r^2 \tag{3.33b}$$

Where, k is a constant coefficient.

It is a routine to revolve the *d-q* axes reference frame at synchronous speed corresponding to the frequency of the supply voltage, which is also congruous to the electrical speed of the rotating rotor flux vector. In the rotor flux coordinates, the *d*-axis of the rotating reference frame coincides with the rotor flux vector. This orientation removes

the *q*-axis component of the rotor flux, which results in a proportional relationship between slip frequency and stator *q*-axis current given a constant (or well-regulated) rotor flux. The introduction of rotor flux coordinates is the foundation for developing the rotor flux oriented control on machine-side inverter.

The development begins with reorganizing (3.22) and (3.23):

$$i_{dr} = \frac{1}{L_r}\psi_{dr} - \frac{L_m}{L_r} i_{ds} \tag{3.34}$$

$$i_{qr} = \frac{1}{L_r}\psi_{qr} - \frac{L_m}{L_r} i_{qs} \tag{3.35}$$

Substituting (3.34) and (3.35) into (3.18) and (3.19), assuming short circuit on rotor windings, results in:

$$\frac{d\psi_{dr}}{dt} + \frac{R_r}{L_r}\psi_{dr} - \frac{L_m}{L_r} R_r i_{ds} - \omega_{sl}\psi_{qr} = 0 \tag{3.36}$$

$$\frac{d\psi_{qr}}{dt} + \frac{R_r}{L_r}\psi_{qr} - \frac{L_m}{L_r} R_r i_{qs} + \omega_{sl}\psi_{dr} = 0 \tag{3.37}$$

$$\omega_{sl} = \omega_e - \omega_r \tag{3.38}$$

where ω_{sl} is the slip frequency.

The alignment of the *d*-axis of the synchronously rotating reference frame with the rotor flux vector naturally effaces the decomposed component of rotor flux on *q*-axis. Figure 3.1 can be amended and shown by Figure 3.4. In this coordinate system, the following equations are valid:

$$\psi_{qr} = 0 \tag{3.39}$$

$$\frac{d\psi_{qr}}{dt} = 0 \tag{3.40}$$

$$\psi_{dr} = \psi_r \tag{3.41}$$

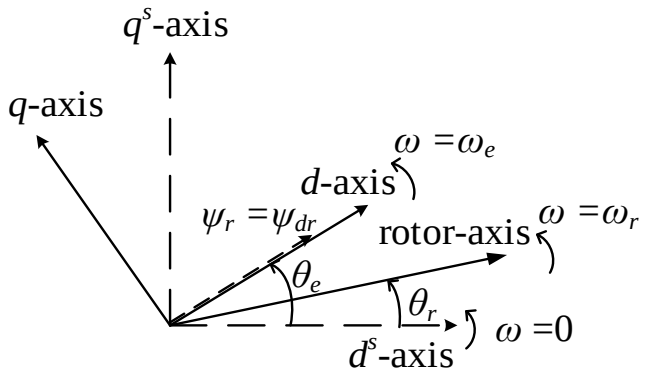

Figure 3.4 Phasor Diagram of Rotor Flux Orientation

Substituting (3.39) – (3.41) into (3.36) and (3.37) gives:

$$\frac{L_r}{R_r}\frac{d\psi_r}{dt} + \psi_r = L_m i_{ds} \tag{3.42}$$

$$\omega_{sl} = \frac{L_m R_r}{\psi_r L_r} i_{qs} \tag{3.43}$$

Again, substituting (3.34) and (3.35) into (3.20) and (3.21) leads to:

$$\psi_{ds} = \left(L_s - \frac{L_m^2}{L_r} \right) i_{ds} + \frac{L_m}{L_r}\psi_{dr} = \sigma_s L_s i_{ds} + \frac{L_m}{L_r}\psi_{dr} \tag{3.44}$$

$$\psi_{qs} = \left(L_s - \frac{L_m^2}{L_r} \right) i_{qs} + \frac{L_m}{L_r}\psi_{qr} = \sigma_s L_s i_{qs} + \frac{L_m}{L_r}\psi_{qr} \tag{3.45}$$

$$\sigma_s = 1 - \frac{L_m^2}{L_s L_r} \tag{3.46}$$

Substituting (3.44) and (3.45) into (3.16) and (3.17), and combining (3.39) – (3.41), results in

$$v_{ds} = R_s i_{ds} + \sigma_s L_s \frac{di_{ds}}{dt} - \omega_e \sigma_s L_s i_{qs} + \frac{L_m}{L_r} \frac{d\psi_r}{dt} \tag{3.47}$$

$$v_{qs} = R_s i_{qs} + \sigma_s L_s \frac{di_{qs}}{dt} + \omega_e \sigma_s L_s i_{ds} + \frac{\omega_e L_m}{L_r} \psi_r \tag{3.48}$$

The *dc*-machine like electro-magnetic torque can be calculated from (3.31), (3.34), (3.35), (3.39), and (3.41) as

$$T_e = \frac{2}{3} \cdot L_m \left[i_{qs} \left(\frac{1}{L_r} \psi_r - \frac{L_m}{L_r} i_{ds} \right) - i_{ds} \left(-\frac{L_m}{L_r} i_{qs} \right) \right]$$

$$= \frac{2}{3} \cdot \frac{L_m}{L_r} \psi_r i_{qs} \tag{3.49}$$

3.4 Rotor Flux Oriented Control

In this section, the indirect rotor flux oriented control is considered and will be discussed in details. The speed of the synchronously rotating reference frame, noted by ω_e, is estimated from measured motor terminal currents and angular velocity of the rotor shaft (ω_r). The angular displacement of the reference frame used for *abc-dq* transformation, denoted by θ_e, is integrated from the estimated synchronous speed ω_e.

For the induction motor model in rotor flux coordinates, there are four major differential equations that describe the speed, flux and stator currents dynamics of the motor given by (3.33a), (3.33b), (3.42), (3.47) and (3.48), respectively. Generally, the machine-side inverter controller includes speed, flux and stator *d-q* axes currents controls. The entire rotor flux oriented control system for the machine-side inverter is shown in Figure 3.5.

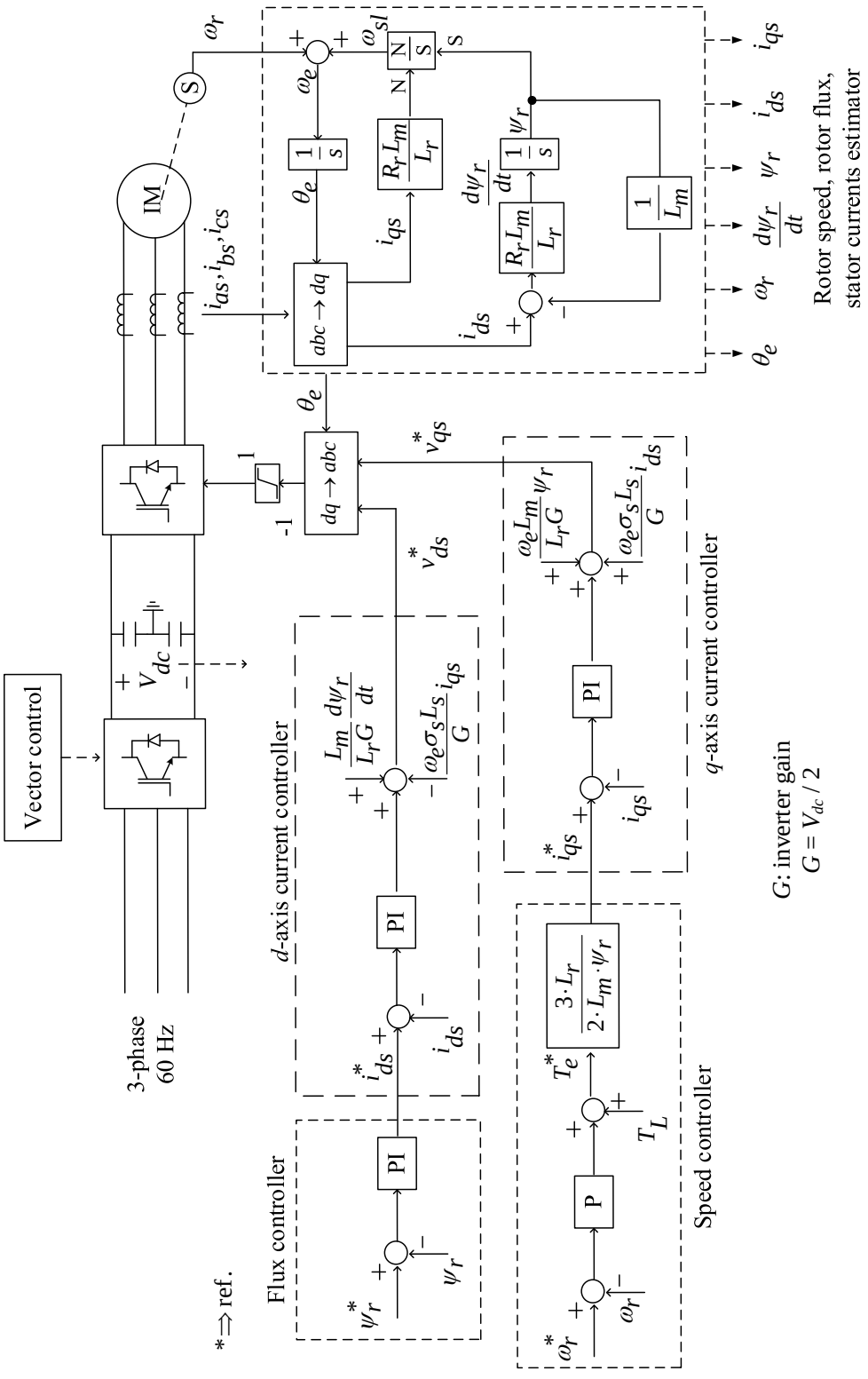

Figure 3.5 Rotor Flux Oriented Control System for the Machine-Side Inverter

The induction motor has a tachometer located on the rotor shaft to measure the rotor velocity and send the signal to an estimator. Meanwhile, the three-phase current meters installed at the motor terminal transmit current measurements to the estimator. The estimator takes advantage of the feedback logic to observe the angular displacement of the reference frame (θ_e), synchronous speed of the reference frame (ω_e), rotor angular velocity (ω_r), rotor flux (ψ_r), derivative of rotor flux, and stator *d*-*q* axes currents. The outputs from the estimator will be sent as inputs to inverter controller chip.

3.5 Vector Control for the Line-Side Rectifier

The line-side rectifier in a double-sided PWM converter system can be vector-controlled to regulate the active power and reactive power independently. Under optimal control, the drive system consumes zero reactive power. Another benefit introduced by the controlled rectifier is the capability to provide voltage support during a fault contingency. Considering all the above benefits and requirements, the active and reactive currents controllers and *dc*-link voltage controller are configured and implemented in the control design. The schematic of the line-side rectifier is given in Figure 3.6.

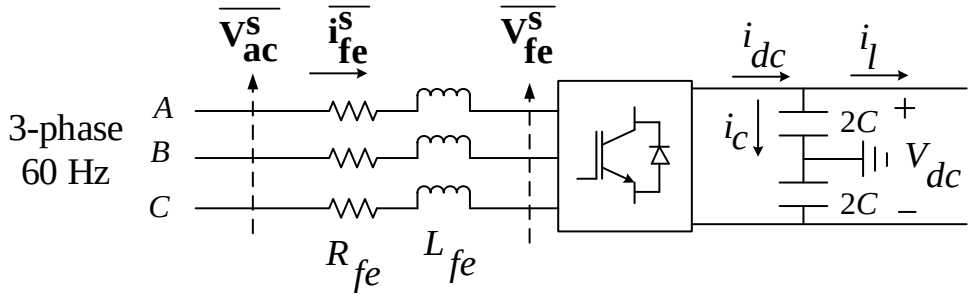

Figure 3.6 Schematic of Line-Side Rectifier

On the *ac* side of the rectifier shown in Figure 3.6, the line current differential equation in space vector form can be written as:

$$\overline{\mathbf{V}_{\mathbf{ac}}^{\mathbf{s}}} = \overline{\mathbf{V}_{\mathbf{fe}}^{\mathbf{s}}} + R_{fe}\overline{\mathbf{i}_{\mathbf{fe}}^{\mathbf{s}}} + L_{fe}\frac{d\overline{\mathbf{i}_{\mathbf{fe}}^{\mathbf{s}}}}{dt} \tag{3.50}$$

Where, $\overline{\mathbf{V}_{\mathbf{ac}}^{\mathbf{s}}}$, $\overline{\mathbf{V}_{\mathbf{fe}}^{\mathbf{s}}}$ and $\overline{\mathbf{i}_{\mathbf{fe}}^{\mathbf{s}}}$ are voltage and current vectors defined in the same form of (3.2). $\overline{\mathbf{V}_{\mathbf{ac}}^{\mathbf{s}}}$ represents the source-side voltage vector, and $\overline{\mathbf{V}_{\mathbf{fe}}^{\mathbf{s}}}$ denotes the converter-side voltage vector, both are on the grid-side and located at the two terminals of the series-connected lateral impedance.

The rule of reference frame transformation portrayed by Figure 3.1 also applies to the grid-side electrical variables of the rectifier. Replicating the reference frame transformation indicated by (3.3) on the voltage and current vectors in (3.50) results in:

$$\overline{\mathbf{V}_{\mathbf{ac}}^{\mathbf{s}}} = \overline{\mathbf{V}_{\mathbf{ac}}} \cdot e^{j\theta_e} = \left(V_{acd} + j \cdot V_{acq}\right) \cdot e^{j\theta_e} \tag{3.51}$$

$$\overline{\mathbf{V}_{\mathbf{fe}}^{\mathbf{s}}} = \overline{\mathbf{V}_{\mathbf{fe}}} \cdot e^{j\theta_e} = \left(V_{fed} + j \cdot V_{feq}\right) \cdot e^{j\theta_e} \tag{3.52}$$

$$\overline{\mathbf{i}_{\mathbf{fe}}^{\mathbf{s}}} = \overline{\mathbf{i}_{\mathbf{fe}}} \cdot e^{j\theta_e} = \left(i_{fed} + j \cdot i_{feq}\right) \cdot e^{j\theta_e} \tag{3.53}$$

Substituting (3.51) – (3.53) into (3.50) gives:

$$V_{acd} = V_{fed} - \omega_e L_{fe} i_{feq} + L_{fe}\frac{di_{fed}}{dt} + R_{fe} i_{fed} \tag{3.54}$$

$$V_{acq} = V_{feq} + \omega_e L_{fe} i_{fed} + L_{fe}\frac{di_{feq}}{dt} + R_{fe} i_{feq} \tag{3.55}$$

Since the frequency of the source-side voltage is deemed equal to the speed of synchronously rotating reference, it is advisable to direct the *d*-axis of the rotating reference frame onto the source-side rotating voltage vector, which eliminates the *q*-axis component of the voltage vector. The space vector diagram is shown in Figure 3.7.

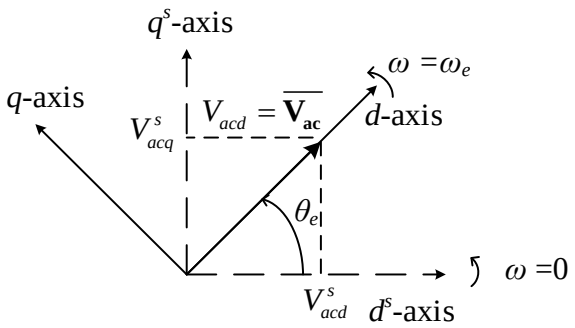

Figure 3.7 Orientation of Source-Side Voltage Vector

From Figure 3.7 it can be seen that,

$$V_{acq} = 0 \tag{3.56}$$

$$V_{acd} = \sqrt{\left(V_{acd}^s\right)^2 + \left(V_{acq}^s\right)^2} \tag{3.57}$$

$$\sin\theta_e = \frac{V_{acq}^s}{V_{acd}} \tag{3.58}$$

$$\cos\theta_e = \frac{V_{acd}^s}{V_{acd}} \tag{3.59}$$

According to the power balance equation [47] and assuming negligible loss on the line-side resistance, the following relation is valid,

$$V_{acd} i_{fed} + V_{acq} i_{feq} = V_{dc} i_{dc} \tag{3.60}$$

There is also a differential equation pertaining to the *dc*-link capacitor, which is,

$$i_{dc} = 2C \frac{d\left(V_{dc}/2\right)}{dt} + i_l \tag{3.61}$$

Combining (3.56) and substituting (3.61) into (3.60) provide,

$$\frac{V_{acd}}{V_{dc}} i_{fed} = C \frac{dV_{dc}}{dt} + i_l \tag{3.62}$$

The three differential equations associated with the currents and voltage controllers are presented by (3.54), (3.55) and (3.62). The control system associated with these three differential equations is shown in Figure 3.8. At the source-side, the three-phase voltages and currents are measured and fed into an estimator to generate *d-q* axes voltages and currents quantities, which are used as inputs by the voltage and currents controllers. The estimator calculates the angular displacement of the synchronous reference frame through (3.57) – (3.59). This function can also be implemented by the phase locked loop (PLL) module [48].

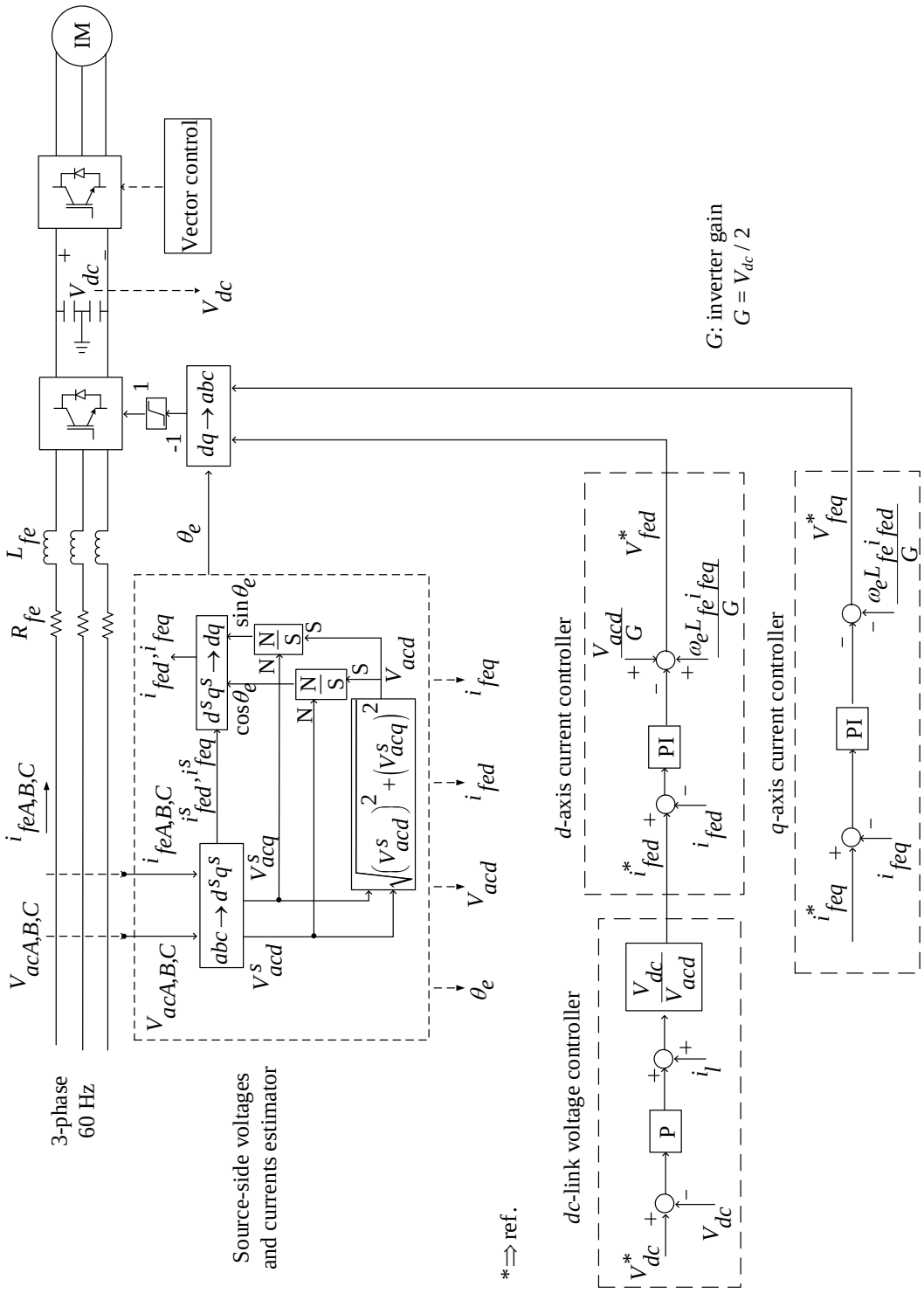

Figure 3.8 Vector Control of Line-Side Rectifier

3.6 Average Model of the Three-Phase PWM Converter

A general three-phase PWM converter has three arms and six semiconductor-based switches. A realistic converter model considering gating frequency, firing sequence and firing instants of all the switches is called a switch model. In some analyses, the switching effects and harmonics production are purposely omitted. Only the average voltages and currents on the *ac*-side are of concern. An average model of the three-phase PWM converter is appropriately proposed to cater to the needs for simplified modeling and integration of multiple devices into the circuit network, which may require a relatively large simulation time step. The average model also genuinely emulates the characteristics of the latest multi-level PWM converters [49], which eliminates low-order voltages and currents harmonics and produces stepped sinusoidal waves.

The switch model of single-phase power pole with SPWM control is depicted in Figure 3.9.

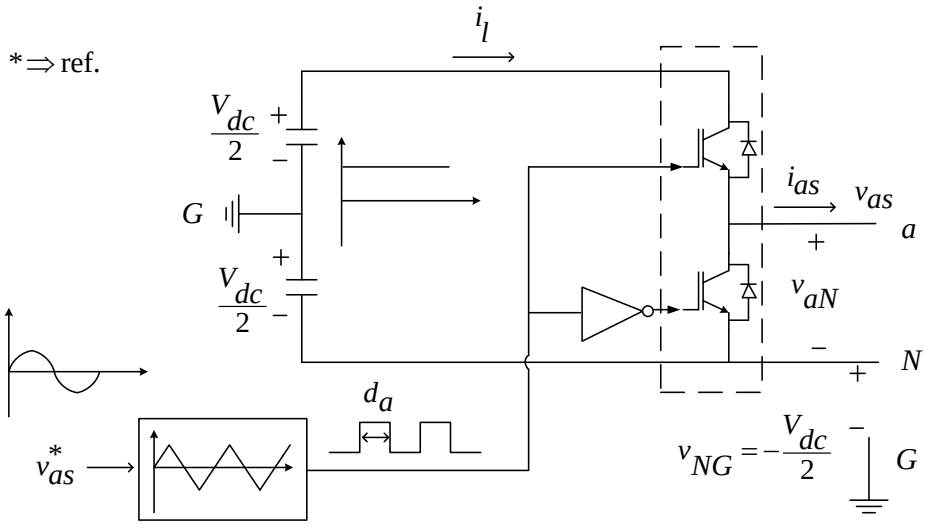

Figure 3.9 Single-Phase Power Pole with SPWM Control

The average model of the single-phase SPWM power pole [28] shown inside the dashed rectangle in Figure 3.9 is depicted in Figure 3.10.

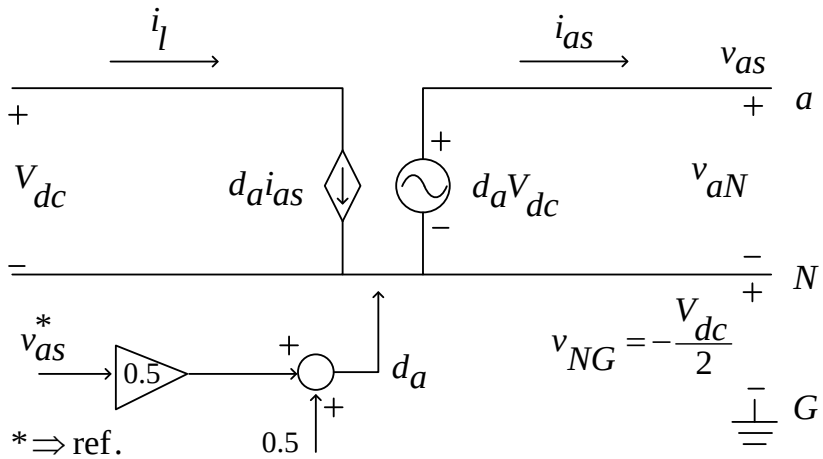

Figure 3.10 Average Model of Single-Phase PWM Power Pole

In Figure 3.10, v_{as}^* is the sinusoidal carrier (reference) wave generated by controller. This normalized reference wave is used to control the amplitude and frequency of the output *ac*-side line-to-ground voltage (v_{as}). d_a is the average value of the instantaneous duty ratio. v_{aN} and v_{as} are the average values of the line-to-neutral and line-to-ground voltages. i_{as} is the average value of the *ac*-side line current. According to Figure 3.10,

$$d_a = \frac{1}{2} + \frac{1}{2} v_{as}^* \tag{3.63}$$

$$i_l = d_a i_{as} \tag{3.64}$$

$$v_{aN} = d_a V_{dc} \tag{3.65}$$

$$v_{NG} = -\frac{V_{dc}}{2} \tag{3.66}$$

Combining (3.63) – (3.66), the line-to-ground voltage v_{as} can be calculated by

$$v_{as} = v_{aN} + v_{NG} = \frac{V_{dc}}{2} \cdot v_{as}^* \tag{3.67}$$

A three-phase PWM converter comprises of three parallel-connected single-phase power poles. The three power poles share the same *dc*-link. The switch model and average model of the three-phase converter are shown in Figure 3.11 and Figure 3.12.

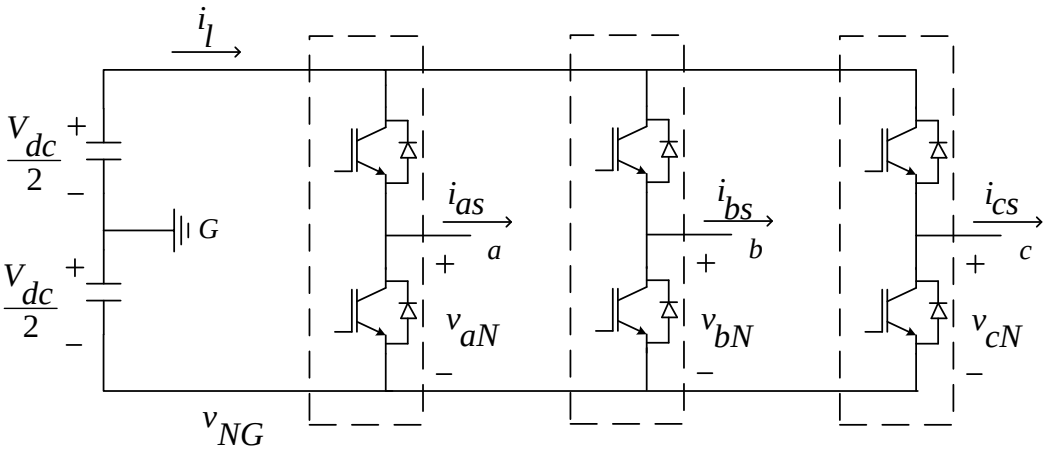

Figure 3.11 Switch Model of a Three-Phase PWM Converter

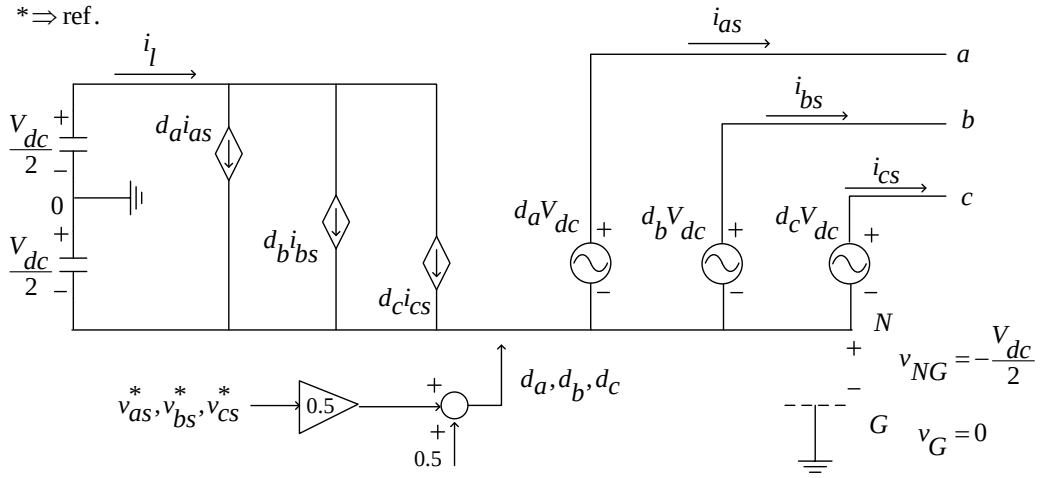

Figure 3.12 Average Model of the Three-Phase PWM Converter with Grounded *dc*-link

According to Figure 3.12, the three-phase line-to-ground voltages can be calculated by (3.68) – (3.70).

$$v_{as} = v_{aN} + v_{NG} = \left(\frac{V_{dc}}{2} + \frac{V_{dc}}{2} v_{as}^*\right) - \frac{V_{dc}}{2} = \frac{V_{dc}}{2} v_{as}^* = G \cdot v_{as}^* \qquad (3.68)$$

$$v_{bs} = \frac{V_{dc}}{2} v_{bs}^{*} = G \cdot v_{bs}^{*} \tag{3.69}$$

$$v_{cs} = \frac{V_{dc}}{2} v_{cs}^{*} = G \cdot v_{cs}^{*} \tag{3.70}$$

$$G = \frac{V_{dc}}{2} \tag{3.71}$$

In (3.68) – (3.71), v_{as}^{*}, v_{bs}^{*} and v_{cs}^{*} are normalized three-phase reference voltage signals generated by the controllers and eventually sent to the PWM converters. *G* is defined as the gain of the converter. The *dc*-link output current is calculated as

$$i_l = d_a i_{as} + d_b i_{bs} + d_c i_{cs} \tag{3.72}$$

The average model of the PWM converter is comprehensively utilized for the machine-side inverter and the grid-side rectifier throughout this research. The reason for using the average model is that it builds up an arithmetic linkage between the *dc*-link and *ac*-side electrical variables, which makes it possible to develop the transient motor drive model in PSTS simulators. This will be discussed in details in Chapter 6.

3.7 Simulation of the EMT Drive

This section presents a set of simulation results to exhibit the performance of the designed vector-controlled drive system. The system parameters are provided in Table A.0.1. This simulation considers decelerating the motor from its rated to 50% rated speed. The motor speed, motor and drive terminal voltages and currents, stator *d-q* axes currents and rotor flux are plotted in Figure 3.13 through Figure 3.19.

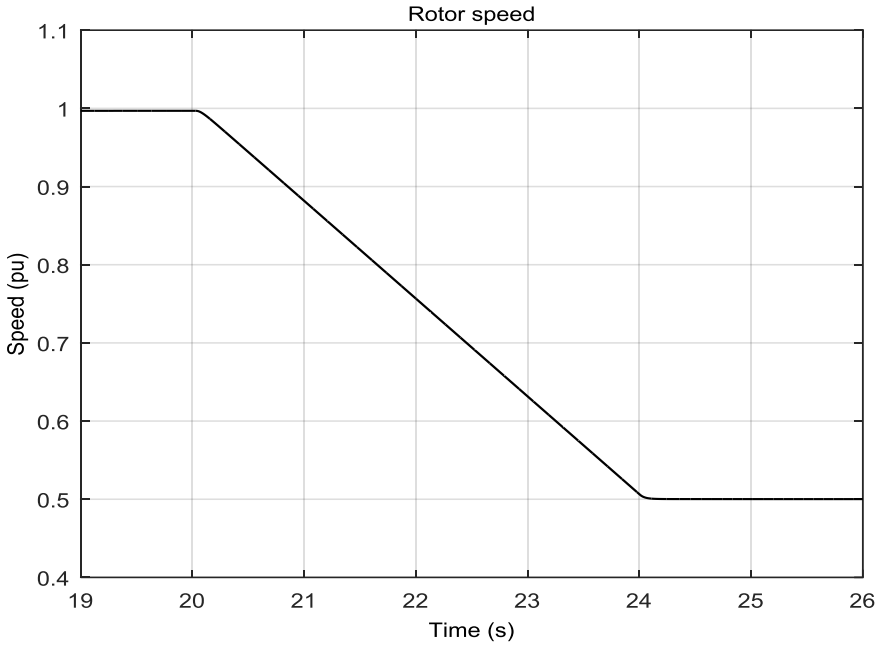

Figure 3.13 Rotor Speed of the Motor behind Drive

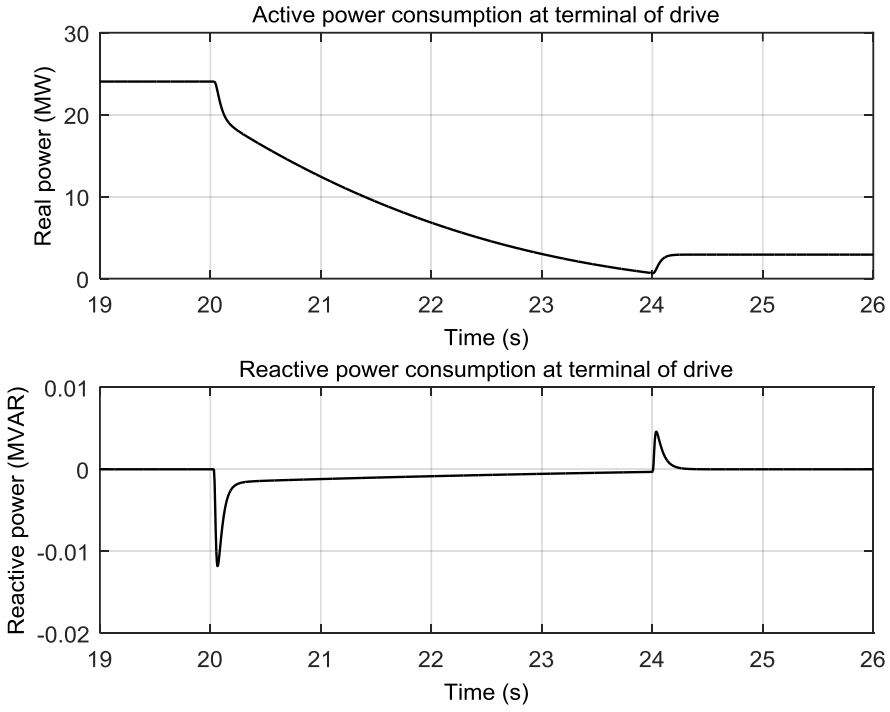

Figure 3.14 Active and Reactive Power Consumptions at the Terminal of Drive

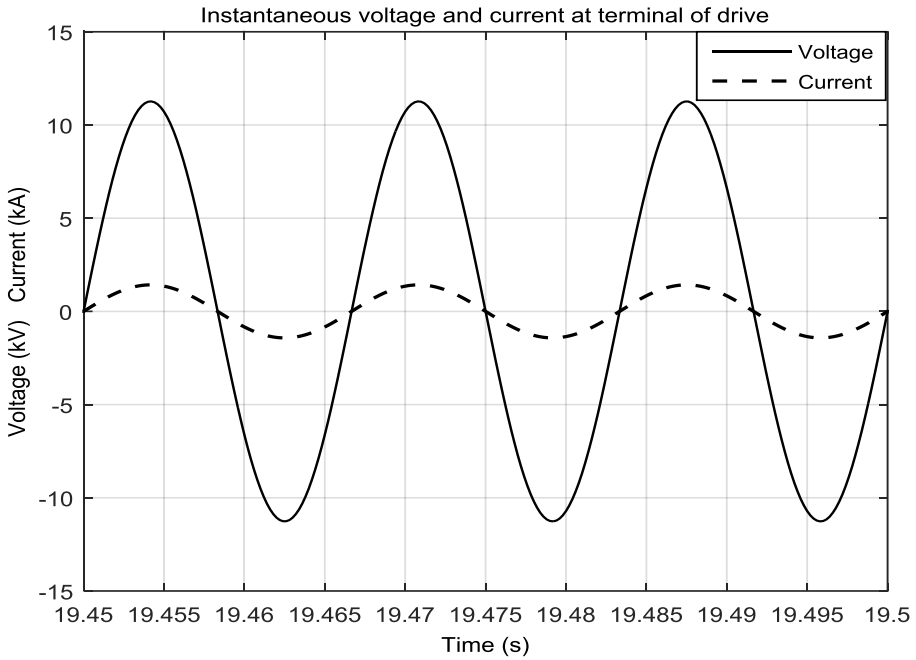

Figure 3.15 Instantaneous Voltage and Current at the Terminal of the Drive

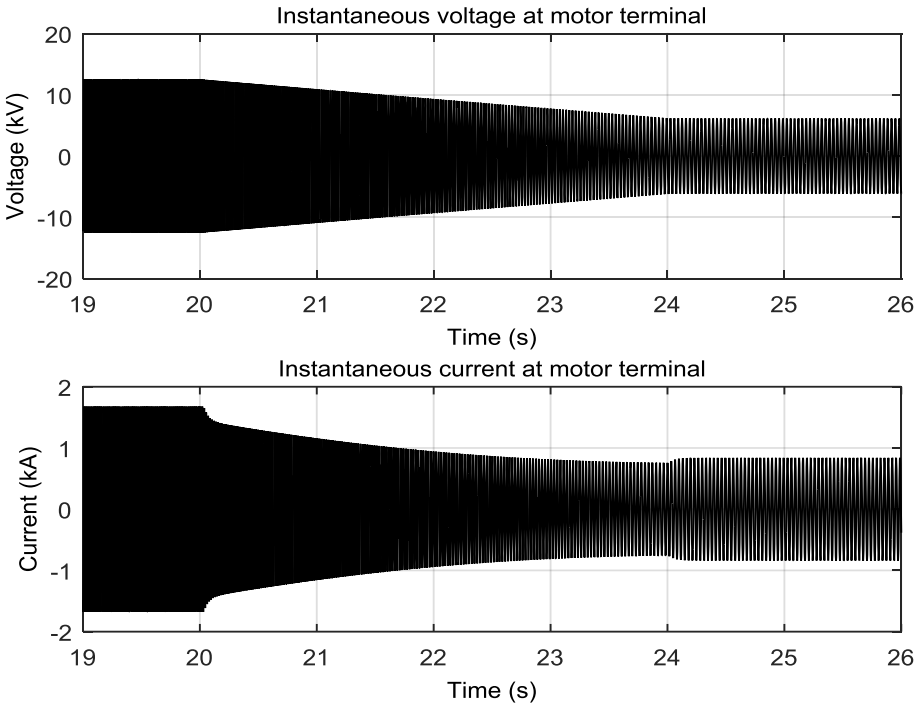

Figure 3.16 Instantaneous Voltage and Current at the Terminal of the Motor

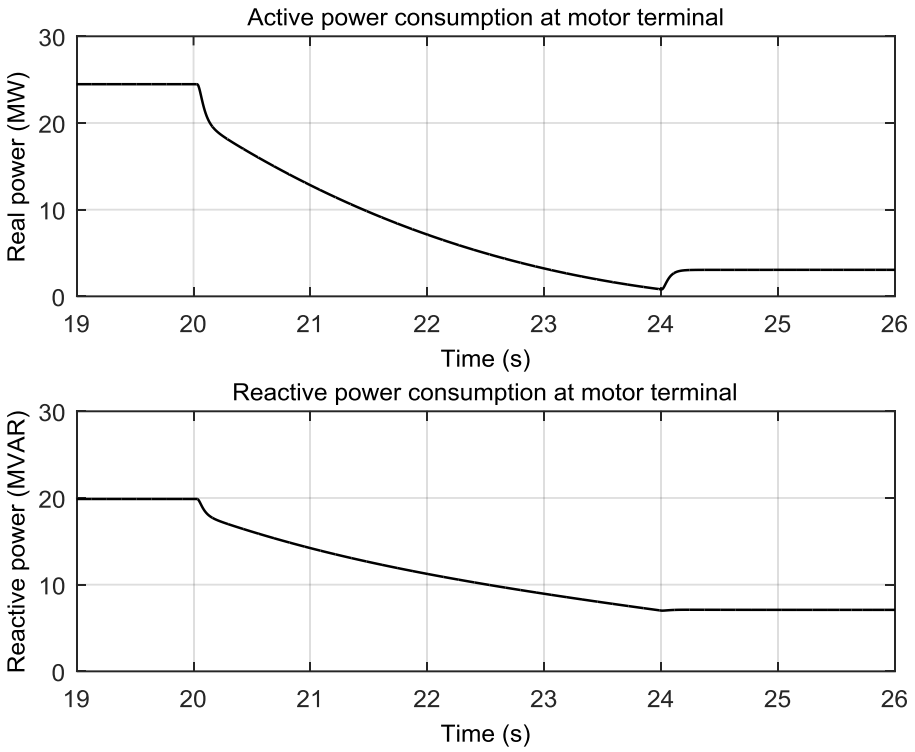

Figure 3.17 Active and Reactive Power at the Terminal of the Motor

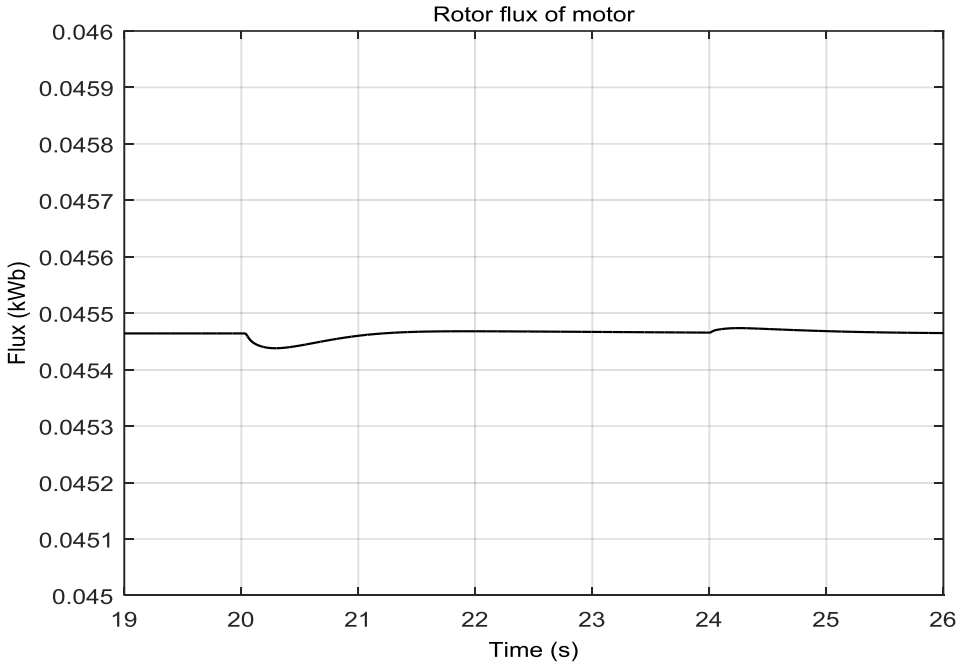

Figure 3.18 Rotor Flux of the Motor behind the Drive

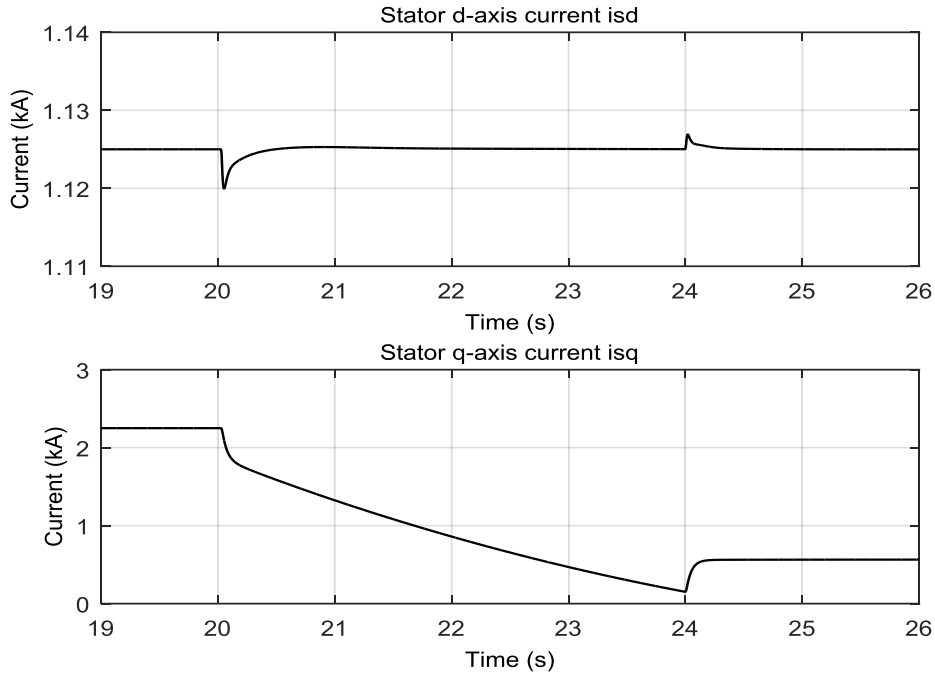

Figure 3.19 Stator *d*-*q* Axes Currents of the Motor behind the Drive

It is seen from Figure 3.13 that the rotor speed is ramped down to 50% in 4 s. The active power of the drive shown in the upper subplot of Figure 3.14 descends to a stable value that is proportional to the cube of the rotor speed. The reactive power in the lower subplot of the same figure is desirably regulated at zero. The instantaneous phase-*a* voltage and current at the terminal of drive are plotted and enlarged in Figure 3.15. It is clearly observed that the voltage and current are in phase with each other. Also, the instantaneous phase-*a* voltage and current at the terminal of motor are presented in Figure 3.16. The inverter generates a variable voltage variable frequency (VVVF) terminal voltage feeding into the motor, as shown in the upper plot of Figure 3.16. The voltage magnitude and frequency are both decreasing to maintain a constant *V*/*f* ratio and also to keep the air-gap flux constant. The phase-*a* stator current in the lower subplot also diminishes because the

torque is decreased. Figure 3.17 exhibits the motor terminal powers. It is noticed that the reactive power absorption is not zero at the motor terminal. Nonetheless, the power factor is corrected to be unity at the drive terminal by the rectifier control. The rotor flux shown in Figure 3.18 is controlled to remain nearly constant. Similarly in Figure 3.19, the *d*-axis stator current is regulated by the current controller. The *q*-axis current, which is proportional to electro-magnetic torque under constant rotor flux, declines to a final value after a series of control actions.

Chapter 4. POSITIVE-SEQUENCE PERFORMANCE-BASED DRIVE MODEL

4.1 Introduction

A performance-based load model is developed in this chapter to capture the dynamic behaviors of a vector-controlled motor drive system in linear operating range. The model formulation is based on relating the active and reactive powers consumed by drive load to voltage and frequency at the point of supply. The development of the performance-based load model of the motor drive system requires the physically observed performance data of a realistic motor drive. Because the performance data is not available to the authors, a three-phase EMT-level motor drive as described in Chapter 3 is used for testing as a surrogate for the realistic drive.

The proposed procedure of model development in this chapter will include the following steps:

- Applying suitable perturbations on the supply voltage and frequency of the surrogate drive system.
- Metering the perturbations of active and reactive powers of the drive.
- Calculating the linear frequency-domain response of the active and reactive powers to the supply voltage and frequency.
- Obtaining the analytic forms of the transfer functions characterizing the frequency-domain performance of the drive.
- Developing electrical and control interfaces that are suitable for use in large-scale simulations in the PSTS program.

The model implementation is accomplished in the PSLF program. The performance-based drive model is validated by comparison with the detailed model simulated in PSCAD. To investigate the system-level dynamic impacts introduced by increasing penetration of converter-driven motor loads, the responses of the proposed PSLF drive load are compared with that of the standard PSLF induction motor model considering varying complexity of grid connections. Simulation cases are formulated to investigate the effect of electronic motor drives on the asymptotic behavior of a simplified two-area system and the detailed IEEE 39-bus system [4].

4.2 Perturbation Analysis

Consider an LTI system with a transfer function $H(j\omega)$ in frequency domain and corresponding $h(t)$ in time domain, if an arbitrary sinusoidal signal given by (4.1) is input into the system, the time-domain output can be computed by convolution shown as (4.2) [50].

$$u(t) = A \cdot \sin(\omega t + \phi) \tag{4.1}$$

$$y(t) = \int_0^t h(\tau) \cdot u(t-\tau)\, d\tau \tag{4.2}$$

The steady state output can be calculated from (4.1) and (4.2) and expressed as

$$y_{ss}(t) = A \cdot \left|H(j\omega)\right| \sin\left[\omega t + \phi + \angle H(j\omega)\right] \tag{4.3}$$

It is obvious from (4.1) and (4.3) that an input of a sinusoidal signal into an LTI system will generate a sinusoidal output with a scaled magnitude and shifted phase angle, which are determined by the transfer function of this LTI system. An advanced *ac* drive system with vector control is inherently a non-linear system. Nevertheless, if the input

perturbation to this system is comparatively small, the complex drive system can be regarded as a linearized LTI system.

As mentioned in Chapter 1 and Chapter 2, a static load is modeled as active and reactive power withdrawals that are algebraically correlated to the instantaneous voltage and frequency. The mathematics of a motor drive system are far more complicated than that of a simple static load model. The static load model roughly represents the aggregation of a variety of load components. As a result, it does not accurately reflect the characteristics of a single intricate load, such as the induction motor load and the motor drive load. A performance-based model of the motor drive system is developed to represent the active and reactive power dynamics of the drive in response to variations of terminal voltage and frequency.

As stated in the previous section (Section 4.1), an EMT point-on-wave motor drive model is used as a replacement for a realistic drive in this research. The EMT drive model, implemented in PSCAD, includes line-side rectifier, machine-side inverter, and corresponding vector control systems. The schematic of the entire drive system is a combination of the rectifier and inverter control systems in Figure 3.5 and Figure 3.8, and is presented in Figure 4.1.

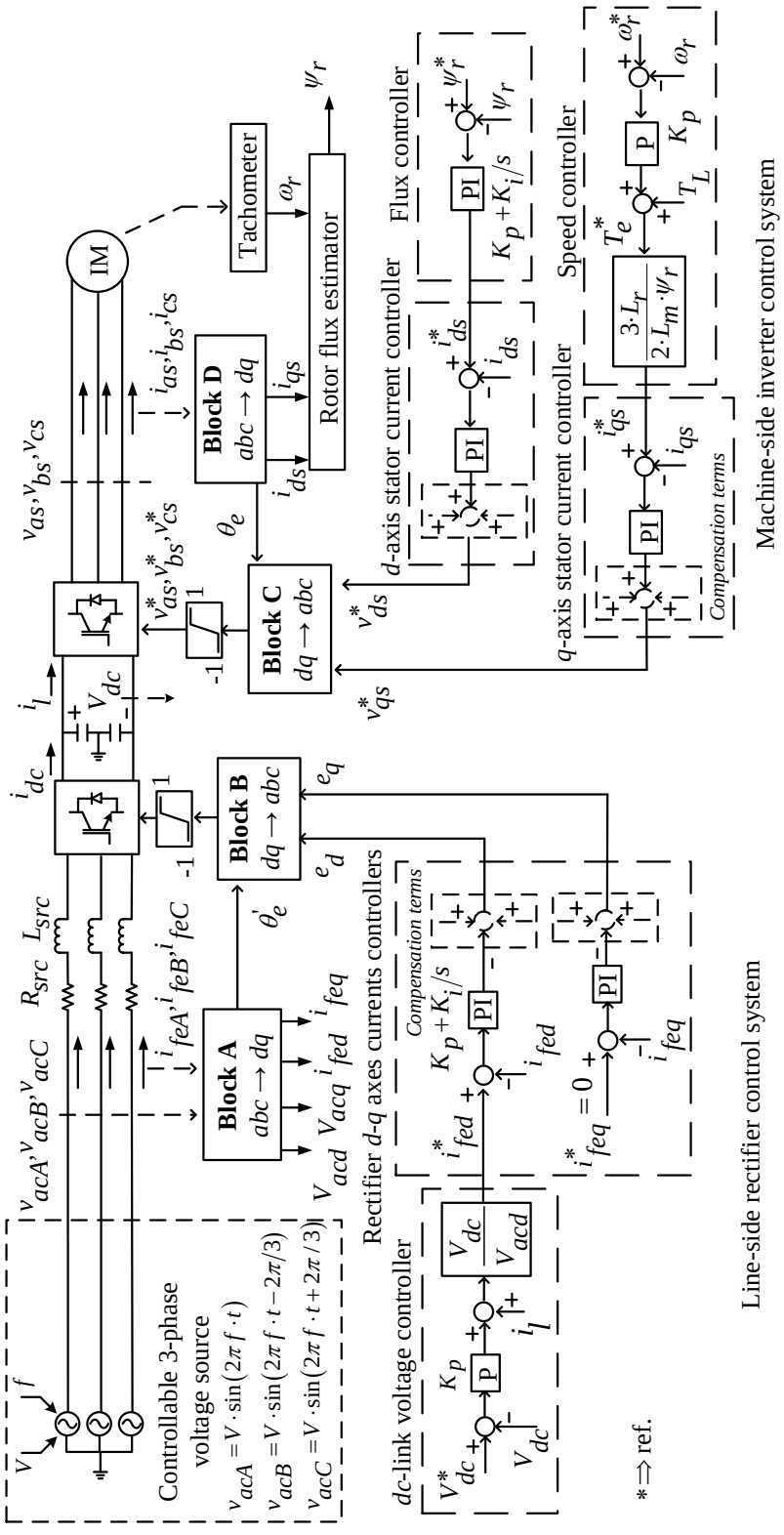

Figure 4.1 Schematic of the Detailed Three-Phase PSCAD Drive Model

In Figure 4.1, the motor drive is connected to a voltage and frequency controllable source. A series of perturbations with incremental sweeping frequencies are added on the supply voltage and frequency of this detailed PSCAD drive model. The amplitude and phase responses characterizing the sensitivities of active and reactive powers to voltage and frequency are calculated and recorded over the range of swept frequency.

For a dynamic load model that is described by differential equations, the active and reactive powers are functions of terminal voltage and frequency, which can be expressed by (4.4) and (4.5) respectively.

$$P = F_1\left(V\left(\omega_p\right), f\left(\omega_p\right)\right) \tag{4.4}$$

$$Q = F_2\left(V\left(\omega_p\right), f\left(\omega_p\right)\right) \tag{4.5}$$

Where, $\omega_p = 2\pi f_p$ represents the system perturbation frequency. Taking the partial derivatives of (4.4) and (4.5) with respect to ω_p and multiplying both sides by $\Delta\omega_p$ yield

$$\Delta P = \frac{\partial P}{\partial V}(s)\Delta V + \frac{\partial P}{\partial f}(s)\Delta f \tag{4.6}$$

$$\Delta Q = \frac{\partial Q}{\partial V}(s)\Delta V + \frac{\partial Q}{\partial f}(s)\Delta f \tag{4.7}$$

Where, ΔV and Δf are small voltage and frequency deviations respectively. The derivatives $\partial P/\partial V$, $\partial P/\partial f$, $\partial Q/\partial V$ and $\partial Q/\partial f$, are functions of the perturbation frequency ω_p, which need to be determined firstly in experimental approaches and secondly in analytic approaches. To develop the analytic form of these four sensitivity transfer functions, the frequency-domain response data need to be obtained from experimental modulation. The modulations of the voltage and frequency are performed separately at the supply side terminal of the drive to procure the responses of active and

reactive power. In Figure 4.1, the modulation of voltage is applied on the supply source and is depicted by (4.8) and (4.9). For demonstration purposes, only the instantaneous phase-*a* voltage is shown.

$$v_a(t) = \left(V_0 + \Delta V\left(f_p\right)\right) \cdot \sin\left(2\pi f_0 t\right) \tag{4.8}$$

$$\Delta V\left(f_p\right) = \Delta V_m \cdot \sin\left(2\pi f_p \cdot t\right) \tag{4.9}$$

The modulation of frequency is depicted by (4.10) and (4.11).

$$v_a(t) = V_0 \cdot \sin\left[2\pi\left(f_0 + \Delta f\left(f_p\right)\right)t\right] \tag{4.10}$$

$$\Delta f\left(f_p\right) = \Delta f_m \cdot \sin\left(2\pi f_p \cdot t\right) \tag{4.11}$$

In which, f_0 is the nominal power frequency (60 Hz). V_0 is the nominal voltage magnitude. ΔV_m and Δf_m are the amplitudes of the modulated voltage and frequency respectively. According to the characteristics of the LTI system indicated by (4.1) – (4.3), perturbed voltage or frequency as input generates perturbed active and reactive powers as outputs at the same modulation frequency. The perturbed active and reactive powers excited by voltage perturbation (4.9) can be expressed by

$$\Delta P_v = \Delta P_{m\_pv}\left(f_p\right) \cdot \sin\left[2\pi f_p \cdot t + \phi_{pv}\left(f_p\right)\right] \tag{4.12}$$

$$\Delta Q_v = \Delta Q_{m\_qv}\left(f_p\right) \cdot \sin\left[2\pi f_p \cdot t + \phi_{qv}\left(f_p\right)\right] \tag{4.13}$$

The perturbed active and reactive power generated by frequency perturbation (4.11) can be denoted by

$$\Delta P_f = \Delta P_{m\_pf}\left(f_p\right) \cdot \sin\left[2\pi f_p \cdot t + \phi_{pf}\left(f_p\right)\right] \tag{4.14}$$

$$\Delta Q_f = \Delta Q_{m\_qf}\left(f_p\right) \cdot \sin\left[2\pi f_p \cdot t + \phi_{qf}\left(f_p\right)\right] \tag{4.15}$$

In (4.12) – (4.15), $\Delta P_{m\_pv}(f_p)$, $\Delta Q_{m\_qv}(f_p)$, $\Delta P_{m\_pf}(f_p)$ and $\Delta Q_{m\_qf}(f_p)$ are amplitudes of the output *P*-*Q* perturbations at modulation frequency f_p, which are excited by the input *V*-*f* perturbations (see (4.9) and (4.11)). $\phi_{pv}(f_p)$, $\phi_{qv}(f_p)$, $\phi_{pf}(f_p)$ and $\phi_{qf}(f_p)$ are relative phase shifts of the *P*-*Q* perturbations compared to the *V*-*f* perturbations.

The modulation described by (4.8) – (4.15) is specifically for one frequency point. In order to derive the analytic transfer functions, modulations for a range of discrete frequencies are necessary. A sweep of the modulation frequency can be performed either in multiple runs or in a one-run simulation. In this research, the voltage and frequency modulations are performed point-by-point over the range 0.1 – 5.0 Hz in steps of 0.2 Hz in a one-run simulation. The modulation is performed on the PSCAD drive system described by Figure 4.1 with parameters given in Table A.0.2 (see APPENDIX A). The time-domain modulation and response plots for the first three frequency points are provided in Figure 4.2. Between each two periods of modulation, the system rests at the nominal operating condition for 10 seconds.

The relative amplitudes and phase shifts of the active and reactive powers to the perturbed voltage or frequency are calculated from Figure 4.2 for each modulation frequency. Figure 4.3 is drawn to illustrate the calculation of magnitude and phase response from time-domain waveforms for each modulation period in Figure 4.2.

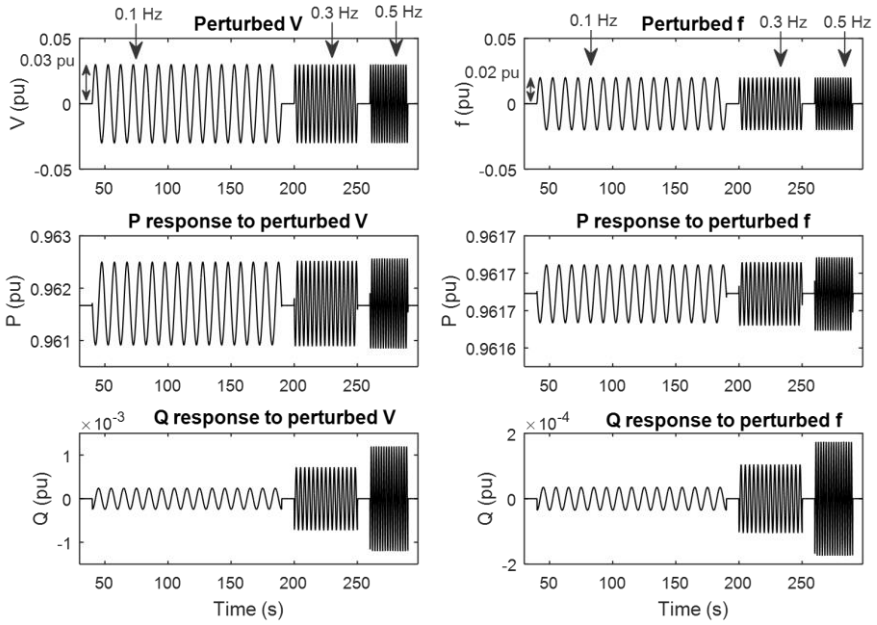

Figure 4.2 Modulation of Voltage and Frequency for the First 3 Frequencies

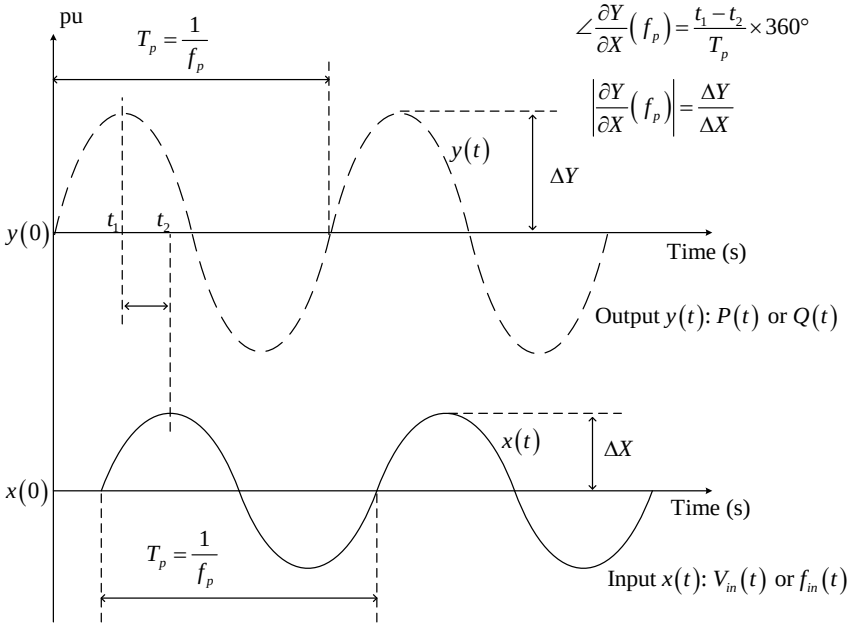

Figure 4.3 Illustration of Calculation of Magnitude and Phase Response for Each Modulation Frequency

After the amplitudes and phase shifts of the *P*-*Q* perturbations are monitored, the frequency-domain magnitude and phase response of $\frac{\partial P}{\partial V}(s)$, $\frac{\partial Q}{\partial V}(s)$, $\frac{\partial P}{\partial f}(s)$ and $\frac{\partial Q}{\partial f}(s)$ at each modulation frequency f_p can be calculated by (4.16) – (4.19) according to the illustration in Figure 4.3.

$$A_{pv}\left(f_p\right)\angle\phi_{pv}\left(f_p\right)=\left|\frac{\Delta P_{m\_pv}\left(f_p\right)}{\Delta V_m}\right|\angle\phi_{pv}\left(f_p\right) \tag{4.16}$$

$$A_{qv}\left(f_p\right)\angle\phi_{qv}\left(f_p\right)=\left|\frac{\Delta Q_{m\_qv}\left(f_p\right)}{\Delta V_m}\right|\angle\phi_{qv}\left(f_p\right) \tag{4.17}$$

$$A_{pf}\left(f_p\right)\angle\phi_{pf}\left(f_p\right)=\left|\frac{\Delta P_{m\_pf}\left(f_p\right)}{\Delta f_m}\right|\angle\phi_{pf}\left(f_p\right) \tag{4.18}$$

$$A_{qf}\left(f_p\right)\angle\phi_{qf}\left(f_p\right)=\left|\frac{\Delta Q_{m\_qf}\left(f_p\right)}{\Delta f_m}\right|\angle\phi_{qf}\left(f_p\right) \tag{4.19}$$

The complete frequency response is obtained by sweeping over the interested range of frequencies. This procedure is illustrated in the flow chart depicted in Figure 4.4.

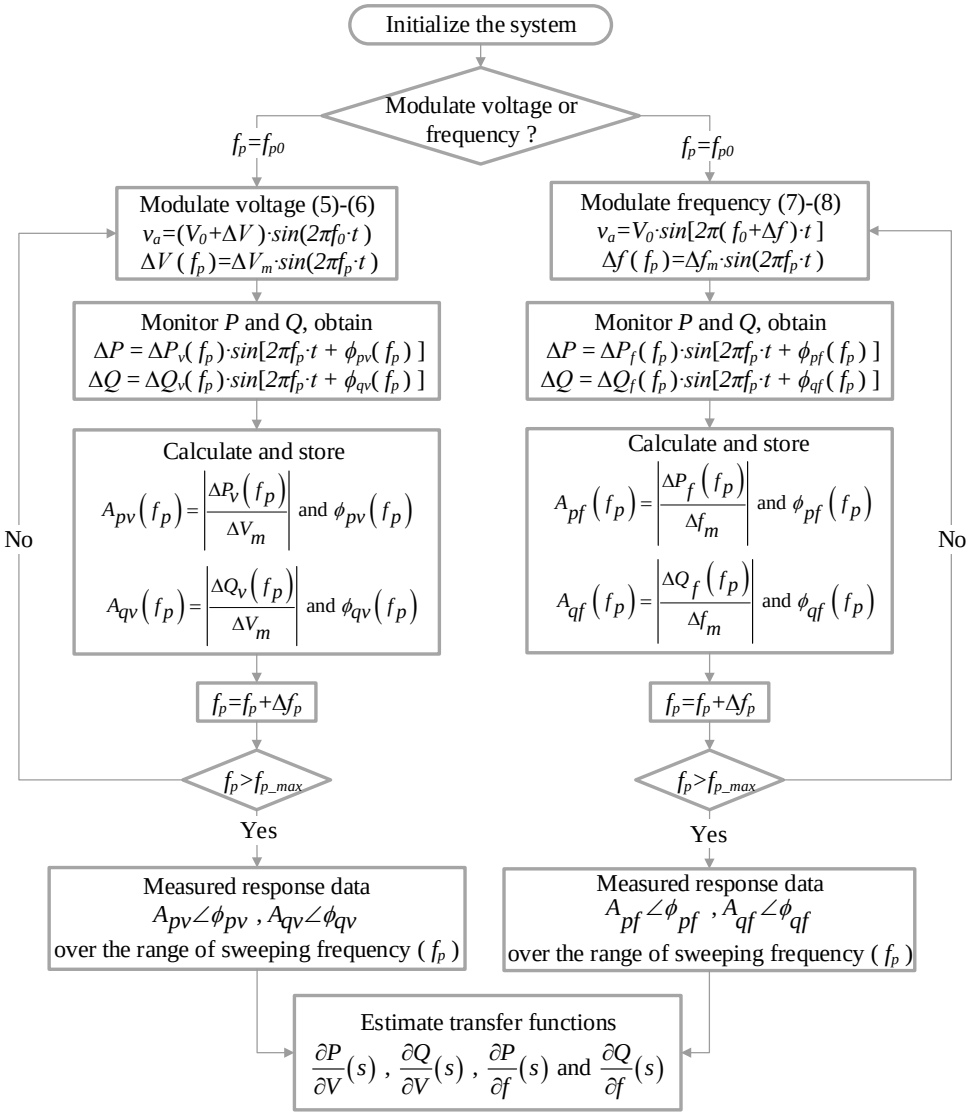

Figure 4.4 Complete Procedure for Obtaining Frequency-Domain Response Data of the Drive from Modulations of Supply Voltage and Frequency

4.3 Estimation of Continuous-Time Transfer Function

The numerator and denominator coefficients of a rational continuous-time transfer function can be estimated by sophisticated optimization algorithms given the sampled data in frequency-domain. The general estimating algorithm implements two major tasks: initializing and updating estimable parameters. For a continuous LTI system, if it is

hypothesized that the inputs and outputs can be sampled at a series of discrete timing instants, the parameters of the frequency-domain system transfer function can be evaluated by employing pre-filtering processing and performing least square estimation (LSE) algorithm[52], [53]. If the frequency responses are measurable, the transfer function can be estimated by utilizing sampled data in frequency domain. The coefficients of transfer function are identified by minimizing the sum of the squares of errors between measured and estimated frequency responses [51], [54]. The acquisition of frequency responses data is achievable according to the discussion in early sections of this chapter. The procedures for deriving transfer functions using the frequency responses data will be briefly addressed in this section.

Consider the analytic form of the estimated transfer function defined by (4.20). The coefficients of the numerator and denominator of the transfer function (4.20) are defined by a vector given by (4.21).

$$H(s,P)=\frac{N(s,P)}{D(s,P)}=\frac{\sum_{m=0}^{n} a_m s^m}{\sum_{m=0}^{d} b_m s^m} \tag{4.20}$$

$$P=\begin{bmatrix} a_0 & a_1 & \cdots & a_n & b_0 & b_1 & \cdots & b_d \end{bmatrix}^T \tag{4.21}$$

where $n \le d$. The measured frequency response of the four sensitivity transfer functions as shown in (4.16) – (4.19) consists of measured magnitude and phase, which can be expressed uniformly by (4.22).

$$H_m(j\omega_k)=A(\omega_k)\angle\phi(\omega_k), \quad \omega_k \in \{\omega_1,\cdots,\omega_N\} \tag{4.22}$$

Where, *N* is the total number of modulated frequencies.

The prediction error minimization approach [51]-[54] is employed to evaluate the transfer functions coefficients defined in the vector form *P*. In general, the estimating algorithm performs two major tasks:

- Estimating the initial coefficients vector $P^{(0)}$.
- Updating *P* by minimizing the prediction error cost function defined by (4.23).

$$\min \text{ Cost}=\sum_{k=1}^{N}\left|H_m\left(j\omega_k\right)-H\left(j\omega_k,P\right)\right|^2=E^TE \tag{4.23}$$

$$E=\left[H_m\left(j\omega_1\right)-H\left(j\omega_1,P\right),\cdots,H_m\left(j\omega_N\right)-H\left(j\omega_N,P\right)\right]^T \tag{4.24}$$

Where, *E* is a vector function (*N* by 1) of the coefficients vector *P*. Converged coefficients vector *P* is obtained using a Newton-Gauss type algorithm [51]. It is noted that the error vector *E* is a function of the vector *P* as shown by (4.25).

$$E=f\left(P\right) \tag{4.25}$$

Applying the Taylor's series expansion, and neglecting high-order terms results in

$$E=f\left(P^{(0)}\right)+J^{(0)}\cdot\left(P-P^{(0)}\right)=E^{(0)}+J^{(0)}\cdot\left(P-P^{(0)}\right) \tag{4.26}$$

$$J^{(0)}=\left(\frac{df}{dP}\right)_{P=P^{(0)}}=\left(\frac{dE}{dP}\right)_{P=P^{(0)}} \tag{4.27}$$

in which, 0 indicates the initial condition. $J^{(0)}$ is an *N* by $dim(P)$ matrix. Left multiplying both sides of (4.26) by $(J^{(0)})^T$ and rearranging the equation yield the result of *P* after the first iteration, given by (4.28).

$$P=P^{(0)}+\left[\left(J^{(0)}\right)^T\left(J^{(0)}\right)\right]^{-1}\left(J^{(0)}\right)^T\left(E-E^{(0)}\right) \tag{4.28}$$

One of the objectives of this optimization problem is to find a feasible solution of the coefficients vector P to force the error vector E to zero. Therefore, a converged P can be found after $(i+1)^{th}$ iteration by numerically integrating (4.29).

$$P^{(i+1)} = P^{(i)} + \left[\left(J^{(i)}\right)^T \left(J^{(i)}\right)\right]^{-1} \left(J^{(i)}\right)^T \left(-E^{(i)}\right) \tag{4.29}$$

$$\Delta P^{(i+1)} = P^{(i+1)} - P^{(i)} < \varepsilon \tag{4.30}$$

The iteration stops when $\Delta P^{(i+1)}$ converges to zero as shown by (4.30), and the optimal coefficients vector P can be calculated correspondingly.

There are multiple analytical formulations of the objective function K [51] aiming to make the resolution more tractable. These approaches are differentiated based on the account of weighting factors and linearity (or nonlinearity).

The commercial analytical software Matlab [56] has a library of continuous-time system identification functions that can be used to estimate the transfer functions given adequate discrete sampled data. The system identification toolbox will be utilized in this research work. It is important to know that Matlab always generates factorable fitted transfer functions.

4.4 Interface of the Performance-Based Drive Model

There are two levels of user-defined models in general PSTS simulation programs, which are interpreted as control system model and electrical system interfaced model. The former model does not connect directly to the network, but controls another device such as a generator or a shunt capacitor. The latter model is a device electrically interfaced to the network, and the examples include generator, induction motor and STATCOM. The initial inputs into these two user-written models stem from the power flow working

case. The parameters of user-defined models are specified in the same dynamic data file in similar formats with the other internally defined models. The flow chart of the dynamic simulation program is illustrated by Figure 4.5. The PSTS simulation program used throughout this dissertation is the General Electric (GE) positive sequence load flow (PSLF) software [10].

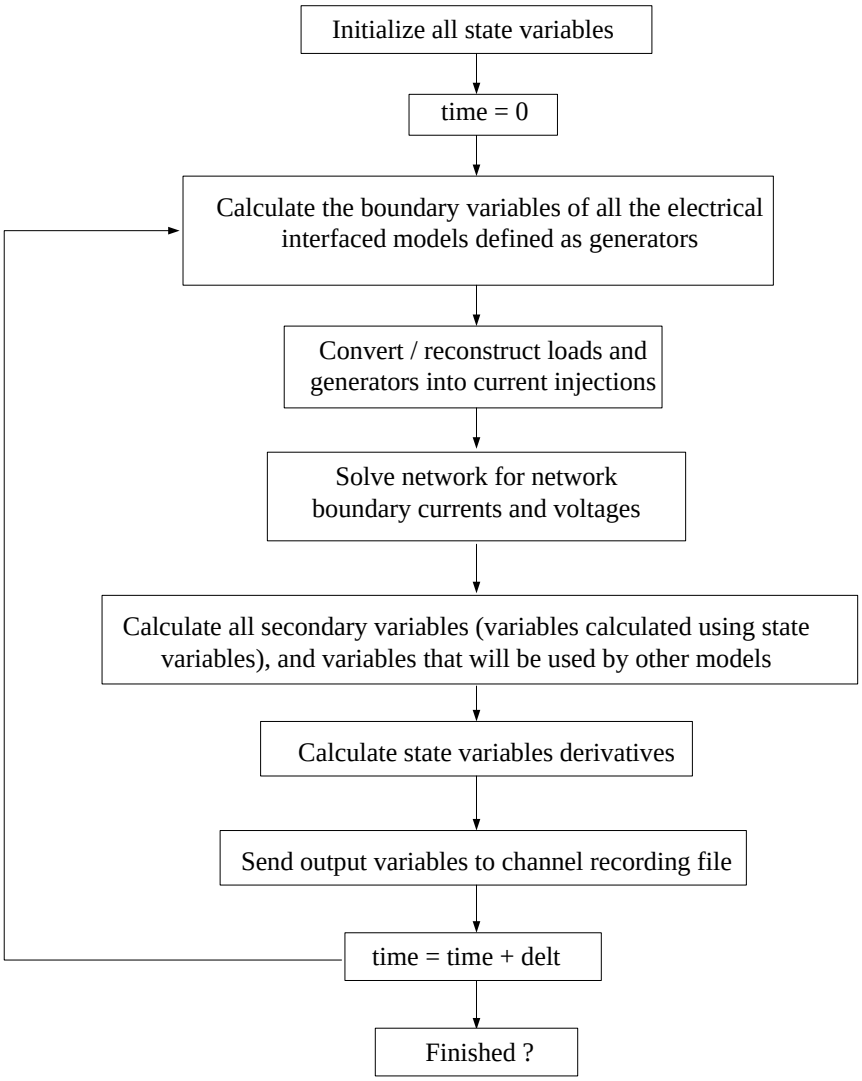

Figure 4.5 Flow Chart of General Dynamic Simulation Program [10]

The static load in the PSTS simulation programs can be represented as a *ZIP* load model consisting of constant impedance (*Z*), constant current (*I*), constant power (*P*)

components, or simply a combination. The dynamic load in the PSTS programs can be represented as an unconstrained "generator-like" model controlled by the characterized transfer functions. The "generator-like" model includes a current injection model and voltage source model [10]. These two models are applicable to certain circumstances respectively. The current injection model is sometimes more straightforward to implement. However, it is less reliable in improving the convergence of the network solution because it contributes no diagonal admittance. Under some specific conditions, the results simulated from both modeling methods overlap each other quite closely. In this research, the voltage source model is implemented as the electrical interface of the load to the positive-sequence grid.

The performance-based load model can be represented by a voltage source in PSLF. The source resistance is neglected in this discussion. The real and imaginary components of the internal voltage denoted by e_d and e_q respectively, are obtained to evaluate the internal voltage source. The imaginary component is designated to align with the real axis of the system reference frame in the model definition as shown in Figure 4.6.

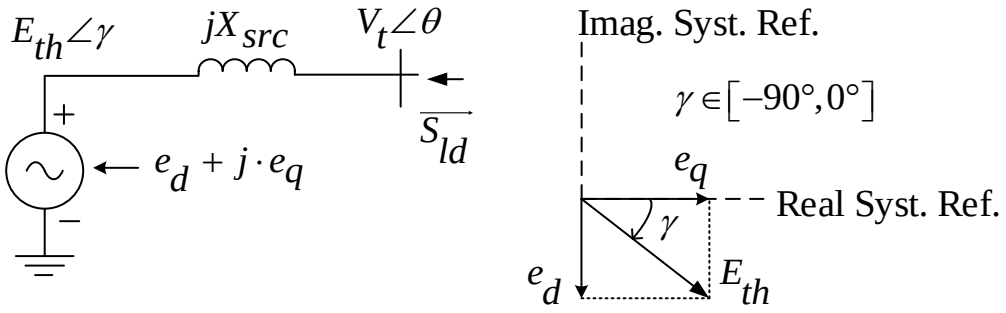

Figure 4.6 General Voltage Source Model in the PSLF

The apparent power flowing from the external system into the load model can be calculated by

$$\overrightarrow{S_{ld}} = P_{ld} + j \cdot Q_{ld}$$

$$= V_t \angle\theta \cdot \left(\vec{I}_t\right)^*$$

$$= V_t \angle\theta \cdot \left(\frac{V_t \angle\theta - E_{th}\angle\gamma}{jX_{src}}\right)^*$$

$$= j \cdot \frac{V_t^2 - V_t E_{th} \angle(\theta - \gamma)}{X_{src}}$$

$$= \frac{V_t E_{th} \sin(\theta - \gamma)}{X_{src}} + j\frac{V_t^2 - V_t E_{th} \cos(\theta - \gamma)}{X_{src}} \tag{4.31}$$

According to the vector diagram in Figure 4.6,

$$\sin(\theta - \gamma) = \sin\theta \cdot \cos\gamma - \cos\theta \cdot \sin\gamma$$

$$= \sin\theta \cdot \frac{e_q}{E_{th}} - \cos\theta \cdot \frac{-e_d}{E_{th}} \tag{4.32}$$

$$\cos(\theta - \gamma) = \cos\theta \cdot \cos\gamma + \sin\theta \cdot \sin\gamma$$

$$= \cos\theta \cdot \frac{e_q}{E_{th}} + \sin\theta \cdot \frac{-e_d}{E_{th}} \tag{4.33}$$

Combining (4.31), (4.32) and (4.33) yields

$$P_{ld} = \frac{V_t\left(e_q \sin\theta + e_d \cos\theta\right)}{X_{src}} \tag{4.34}$$

$$Q_{ld} = \frac{V_t^2 + V_t\left(-e_q \cos\theta + e_d \sin\theta\right)}{X_{src}} \tag{4.35}$$

Moving some irrelevant terms to the other side and re-organizing (4.34) and (4.35) give:

$$e_d \cos\theta + e_q \sin\theta = \frac{P_{ld} X_{src}}{V_t} \tag{4.36}$$

$$-e_q \cos\theta + e_d \sin\theta = \frac{Q_{ld} X_{src} - V_t^2}{V_t} \tag{4.37}$$

The internal voltages e_d and $e_q$can be calculated by

$$e_d = (4.36)\cdot\cos\theta + (4.37)\cdot\sin\theta$$

$$= \frac{P_{ld} X_{src}}{V_t}\cos\theta + \frac{Q_{ld} X_{src} - V_t^2}{V_t}\sin\theta \tag{4.38}$$

$$e_q = (4.36)\cdot\sin\theta - (4.37)\cdot\cos\theta$$

$$= \frac{P_{ld} X_{src}}{V_t}\sin\theta - \frac{Q_{ld} X_{src} - V_t^2}{V_t}\cos\theta \tag{4.39}$$

At each time step of the simulation, P_{ld} and Q_{ld} are obtained as the summation of the initial load powers from the power flow data file and the outputs from the transfer function model (4.6) and (4.7). The terminal voltage magnitude V_t and angle θ are obtained using the PSLF internally defined functions. The structure of the performance-based load model is described in Figure 4.7, in which the four sensitivity transfer functions represent the linear characteristics of the surrogate PSCAD drive.

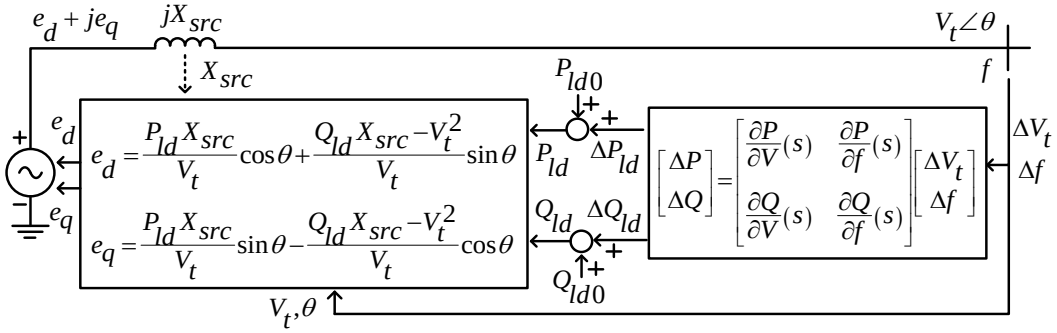

Figure 4.7 Performance-Based Load Model Framework

Section 4.3 has covered the theory of estimating transfer functions. The usage of Matlab software has been specified at the end of Section 4.3. The estimated transfer

function from the Matlab system identification toolbox can usually be rationalized into combination of a constant gain, several first order lead-lag blocks and second order transfer function blocks. This guarantees that the estimated transfer function can be implemented in numerical integration in the PSLF program. The formulae of first order and second order transfer functions can be given by (4.40) and (4.41).

$$TF(s) = \frac{1 + T_1 s}{1 + T_2 s} \tag{4.40}$$

$$TF(s) = \frac{1 + a_1 s}{1 + b_1 s + b_2 s^2} \tag{4.41}$$

In the PSLF model definition file, the derivatives of state variables of each model need to be calculated in the RATE subroutine during each integration loop as depicted in Figure 4.5 [10]. The PSLF internal solution engine performs second-order Euler integration using the updated derivatives of state variables of all the models to obtain a new set of state variables at the next time instant. In order to facilitate the computation of derivatives of state variables, the two fundamental transfer functions defined by (4.40) and (4.41) require to be transformed to dissociate the integrator blocks. The transfer functions are illustrated by the block diagrams in Figure 4.8 and Figure 4.9.

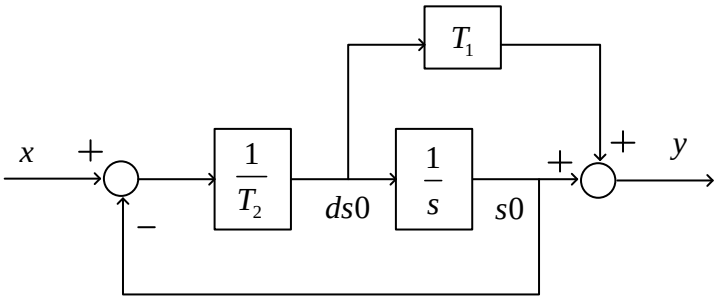

Figure 4.8 Transfer Function of a Lead-Lag Block

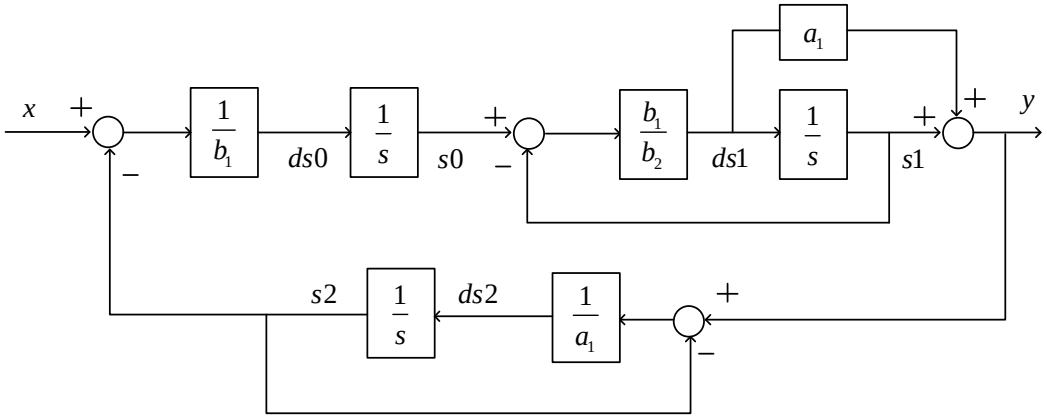

Figure 4.9 Transfer Function of a Second Order Block

For Figure 4.8, the derivative of state variable and the output can be calculated as

$$ds0 = \frac{x - s0}{T_2} \tag{4.42}$$

$$y = s0 + T_1 \cdot ds0 \tag{4.43}$$

While for Figure 4.9,

$$ds0 = \frac{x - s2}{b_1} \tag{4.44}$$

$$ds1 = \frac{b_1}{b_2}(s0 - s1) \tag{4.45}$$

$$y = s1 + a_1 \cdot ds1 \tag{4.46}$$

$$ds2 = \frac{(y - s2)}{a_1} \tag{4.47}$$

The system-wide numerical integration to update state variables can be performed in two stages by (4.48) and (4.49) using the calculated derivatives of state variables of all the dynamic models [10].

$$zs_i(t+h) = zs_i(t) + h \cdot ds_i(t) \tag{4.48}$$

$$s_i(t+h) = zs_i(t+h) + \frac{h}{2} \cdot ds_i(t) \tag{4.49}$$

Where, zs_i is an intermediate variable used to store the first-stage state variable, $zs_i(0) = s_i(0)$. h is the integration time step.

The general form of the estimated transfer function can be expressed by (4.20). After the factorization in Matlab, the transfer function can be expressed by (4.50).

$$TF_{est}(s) = M + K \cdot \sum_{i=1}^{N} TF_i(s) \tag{4.50}$$

In (4.50), $TF_i(s)$ can be either the lead-lag block (4.40) or the second-order block (4.41). N is the total number of blocks. M is usually zero, but sometimes it can be a constant offset. K is a constant gain.

The estimated transfer functions for $\frac{\partial P}{\partial V}(s)$, $\frac{\partial Q}{\partial V}(s)$, $\frac{\partial P}{\partial f}(s)$ and $\frac{\partial Q}{\partial f}(s)$ can be different in order depending on the nature of the modulated system and the required precision of the estimation. The next section (Section 4.5) will demonstrate the four derived transfer functions from the modulation of the sample drive system whose parameters are shown in Table A.0.2.

4.5 Estimated Transfer Functions for the Sample Drive System

In this section, the four transfer functions characterizing the drive model are derived from the modulation data of the detailed PSCAD drive model. The modulation details on the sample system have been stated in Section 4.2, and are now summarized in Table 4.1.

Table 4.1 Details of Modulation on the Sample System

Schematic of the modulated system	Figure 4.1 (drive parameters shown in Table A.0.2)
Modulation mode	One-run simulation
Modulation range	0.1 – 5.0 Hz
Modulation frequency increment	0.2 Hz
Amplitude of voltage perturbation	0.03 pu
Amplitude of frequency perturbation	0.02 pu
Rest time (between two periods of modulation)	10 s
Number of cycles for each modulated frequency	15

The modulations of voltage and frequency and the corresponding response of active and reactive powers have been plotted in Figure 4.2. For clear demonstration purpose, only the first 3 modulation periods are enclosed in Figure 4.2. The four transfer functions are estimated using the modulated frequency-domain data based on the theories introduced in Section 4.3. Matlab is utilized to accomplish the estimation. The initial unfactorized transfer functions estimated by Matlab are in the same form as (4.20), which are given by

$$\frac{\partial P}{\partial V}(s)=\frac{-0.02628-6.151\times10^{-4}s+3.214\times10^{-4}s^2}{1+0.09314s+1.35\times10^{-3}s^2} \tag{4.51}$$

$$\frac{\partial Q}{\partial V}(s)=\frac{6.127\times10^{-4}-0.01265s-7.565\times10^{-4}s^2}{1+0.08555s+1.85\times10^{-3}s^2} \tag{4.52}$$

$$\frac{\partial P}{\partial f}(s)=\frac{-7.629\times10^{-4}-1.165\times10^{-4}s+1.737\times10^{-5}s^2}{1+0.1069s+3.24\times10^{-3}s^2+2.286\times10^{-5}s^3} \tag{4.53}$$

$$\frac{\partial Q}{\partial f}(s)=\frac{7.039\times10^{-7}-2.777\times10^{-3}s-4.731\times10^{-4}s^2}{1+0.2005s+5.325\times10^{-3}s^2+3.956\times10^{-5}s^3} \tag{4.54}$$

The factorization of (4.51) – (4.54) is completed in Matlab to make the transfer functions implementable and programmable in PSLF. The factorized transfer functions are in the fashion of (4.50), and are expressed by

$$\frac{\partial P}{\partial V}(s)=0.238+(-0.2644)\frac{1+0.0862s}{1+0.09314s+1.35\times10^{-3}s^2} \tag{4.55}$$

$$\frac{\partial Q}{\partial V}(s)=-0.4089+0.4095\cdot\frac{1+0.0547s}{1+0.08555s+1.85\times10^{-3}s^2} \tag{4.56}$$

$$\frac{\partial P}{\partial f}(s)=-7.6295\times10^{-4}\cdot\frac{1-0.09276s}{1+0.01011s}\cdot\frac{1+0.24546s}{1+0.09683s+2.2613\times10^{-3}s^2} \tag{4.57}$$

$$\frac{\partial Q}{\partial f}(s)=7.0389\times10^{-7}\cdot\frac{1-3944.773s}{1+0.1707s}\cdot\frac{1+0.1704s}{1+0.02984s+2.3174\times10^{-4}s^2} \tag{4.58}$$

The bode plots showing the comparison of the estimated transfer functions (4.55) – (4.58) and the measured frequency response are presented in Figure 4.10.

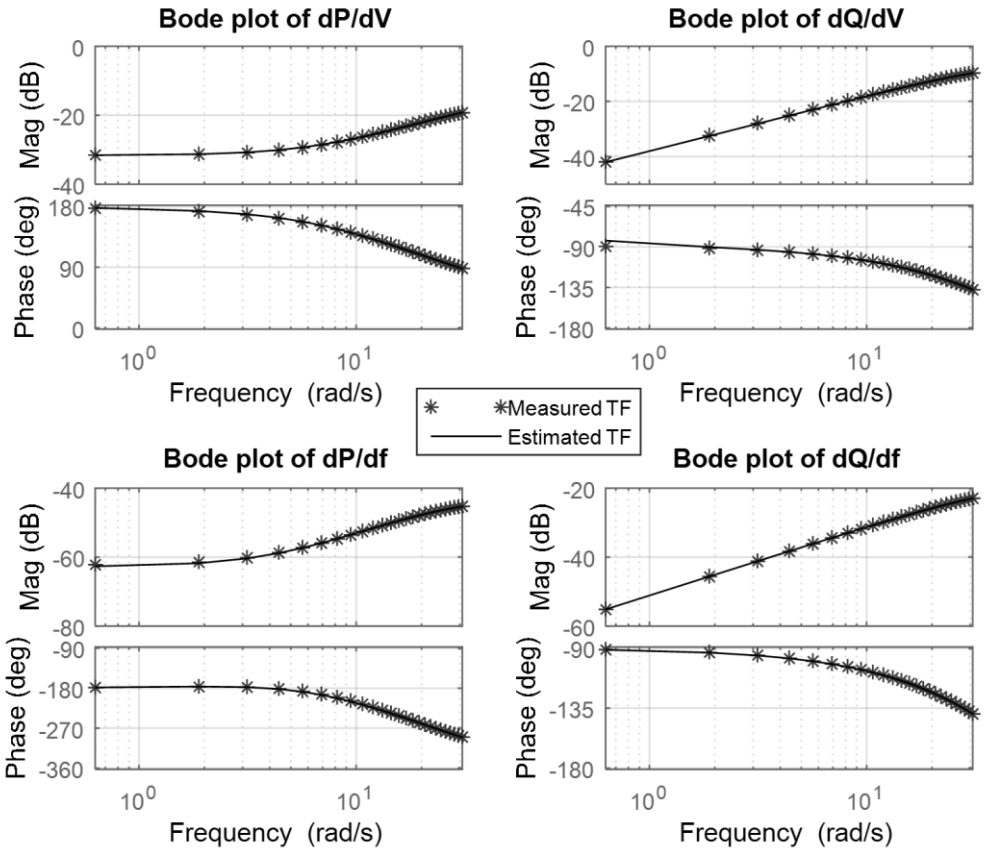

Figure 4.10 Comparison of Bode Plots of the Measured Response and Estimated Transfer Functions over the Modulation Range (0.1 – 5.0 Hz) (Asterisk Indicates Measured Response at Each Frequency)

The complete performance-based drive load model is formulated by combining the electrical interface in Figure 4.7 and the characterized transfer functions (4.55) – (4.58). And this sample drive model will be applied to examine the system dynamics in the next section (Section 4.6).

4.6 Comparison and Applications

In this section, the developed PSLF performance-based drive model in Section 4.5 is compared with the detailed PSCAD drive model by observing the power consumption of the drive subject to different changes of terminal voltage and frequency.

Following the comparison, the developed PSLF drive model is applied to compare the dynamic responses with the PSLF direct-connected induction motor model in two different system connections. The capability of drive and motor loads on damping low-frequency oscillations is investigated. Tripping one transmission line causes slow-varying oscillations on system voltage and frequency. This low-frequency fluctuation is usually intrinsically excited by one dominant sluggish state variable (usually rotor speed or angle) associated with the rotating mass. The oscillation of frequency can be traditionally damped by rotating machines in the system with considerable damping factor, while oscillation of voltage can be damped by VAr support devices in the system.

In the two applications, the same PSLF drive model as in Section 4.5 is used. The PSLF Motor1 model [10] with the same parameters (see Table A.0.2) as the drive-supplied motor is used to represent the direct-connected induction motor throughout Section 4.6. Application 1 (Section 4.6.2) simulates a classical two-area system with a single dynamic load model for which either a pure motor load or a pure drive load is considered. Application 2 (Section 4.6.3) simulates a detailed transmission system with multiple units of mixed load model in which different percentages of drive and motor components are considered.

4.6.1 Comparison with PSCAD Detailed Drive Model

In this part, the PSLF performance-based drive model is compared with the detailed PSCAD drive model. The structure of the developed performance-based drive model has been depicted in Figure 4.7 with the transfer functions defined by (4.50) – (4.53). The detailed PSCAD drive model is presented in Figure 4.1. The test system is a simple two-bus radial feeder shown in Figure 4.11. The load model that represents the PSLF or PSCAD

drive is connected to a voltage and frequency controllable source through a distribution transformer. The responses of the PSLF and PSCAD drive load models are compared when the operating source voltage or frequency is perturbed sinusoidally, or in a step fashion or in a ramp fashion.

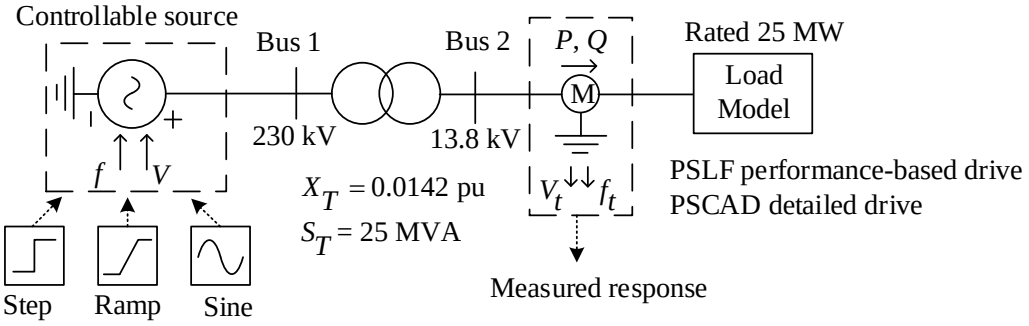

Figure 4.11 Schematic for Comparing the Linear Model and Detailed Model

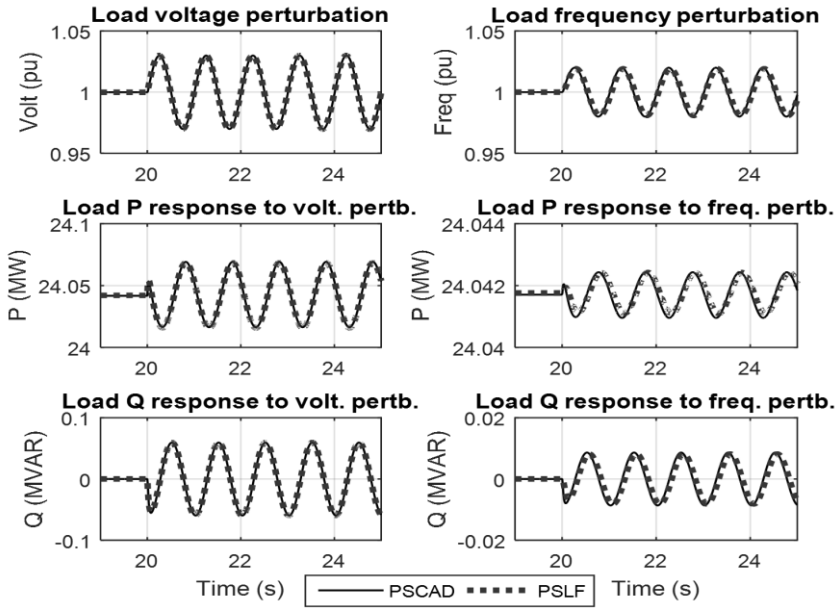

Figure 4.12 Responses of the PSLF and PSCAD Drive Models Subjected to Sinusoidal Perturbations of Source Voltage and Frequency

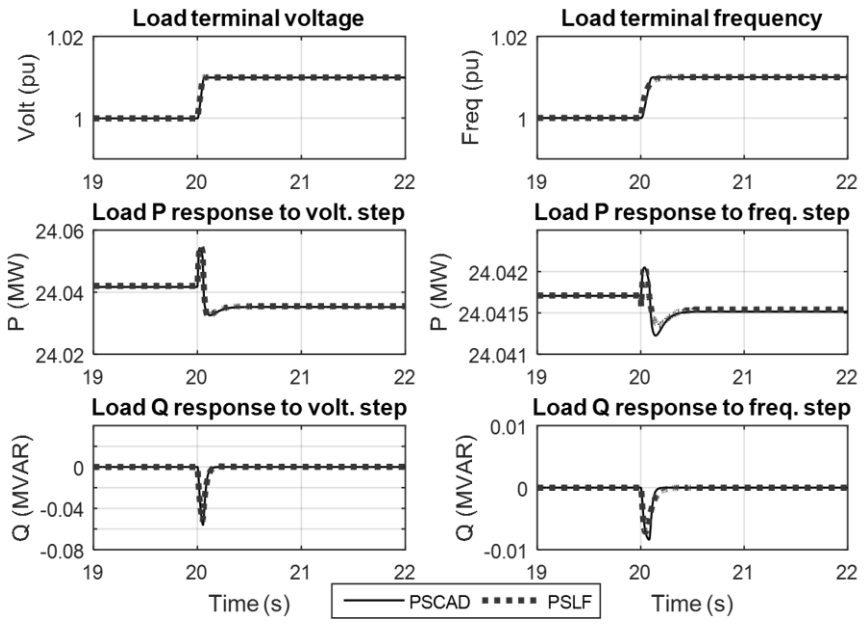

Figure 4.13 Responses of the PSLF and PSCAD Drive Models Subjected to Step Changes on Source Voltage and Frequency

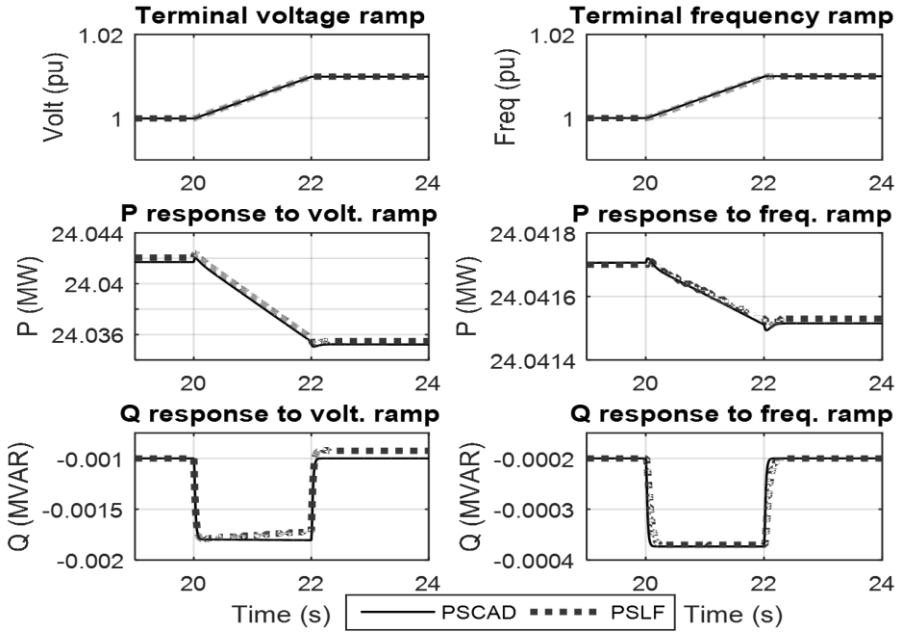

Figure 4.14 Responses of the PSLF and PSCAD Drive Models Subjected to Ramp Changes on Source Voltage and Frequency

Figure 4.12 shows the responses of load powers when perturbed sine waves are added on the nominal source voltage (defined by (4.8) – (4.9)) or on the nominal source

frequency (defined by (4.10) – (4.11)). For both cases, the perturbation frequency is 1.0 Hz. Figure 4.13 and Figure 4.14 present the responses of load powers to step and ramp changes on source voltage and source frequency. The matching results shown in Figure 4.12 through Figure 4.14 reveal that the PSLF performance-based drive model can precisely reproduce the dynamic behaviors of the PSCAD detailed drive model in linear operating range.

4.6.2 Application 1: Two-Area Grid Behavior

A common two-area system is synthesized as shown in Figure 4.15. This two-area system is parametrically symmetrical centered on Bus 3. The loads at Bus 2 and Bus 4 are represented using a constant current model. A total of 250 MW active power is flowing from Bus 2 to Bus 3. The load at Bus 6 is represented by either a direct-connected induction motor or an electronic motor drive. The Bus 6 load is a varied for the convenience of creating different levels of load aggregation at the mid-point of the system. Table 4.2 shows the different simulation cases. It is assumed that the power factors of all loads are unity. A contingency of tripping one tie-line between Buses 2 and 3 excites low-frequency oscillations. The simulation results are shown in Figure 4.16 through Figure 4.21Figure 4.21.

Table 4.2 Case Preparation for the Simulation

Case	Load at Bus 6 (MW)	Load type	Total power flow between Buses 3 and 4 (MW)
A	*a*= 50	Drive Load	200
		Motor Load	
B	*a*= 200	Drive Load	50
		Motor Load	

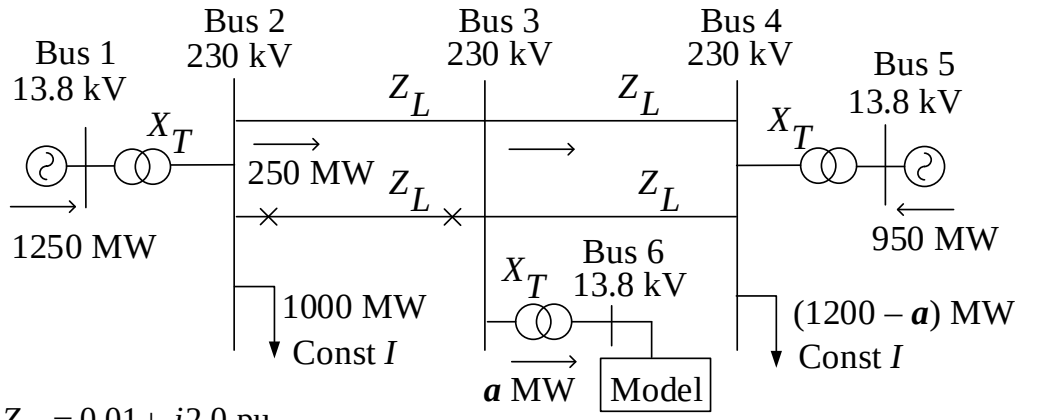

$Z_L = 0.01 + j2.0$ pu,

$X_T = 0.0567$ pu, both on 1000 MVA

Model represents motor or drive load

Figure 4.15 Two-Area System

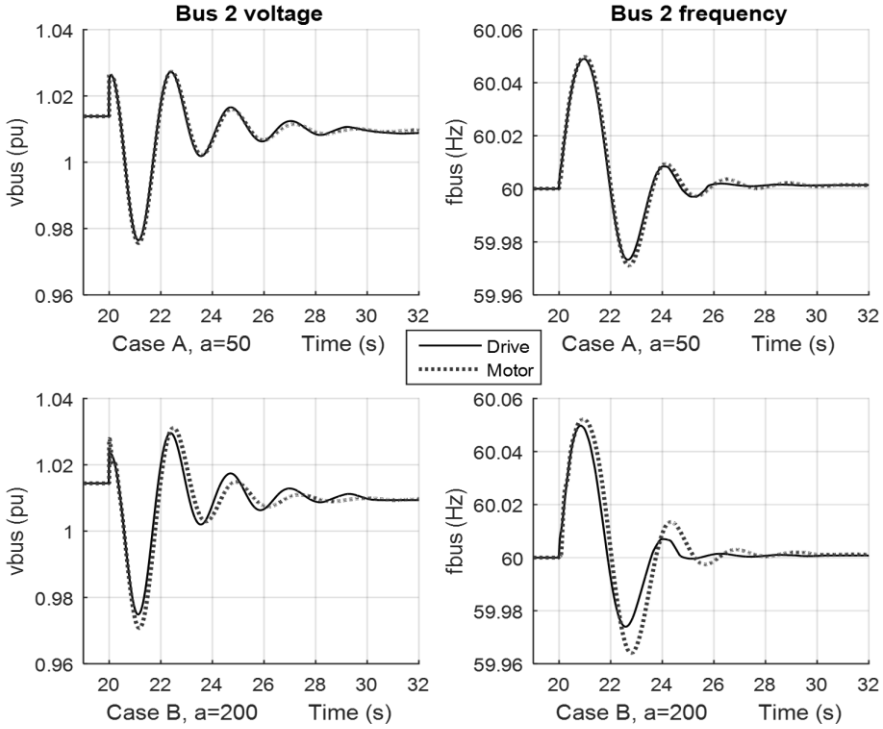

Figure 4.16 **Cases A and B**: Bus 2 Voltage and Frequency

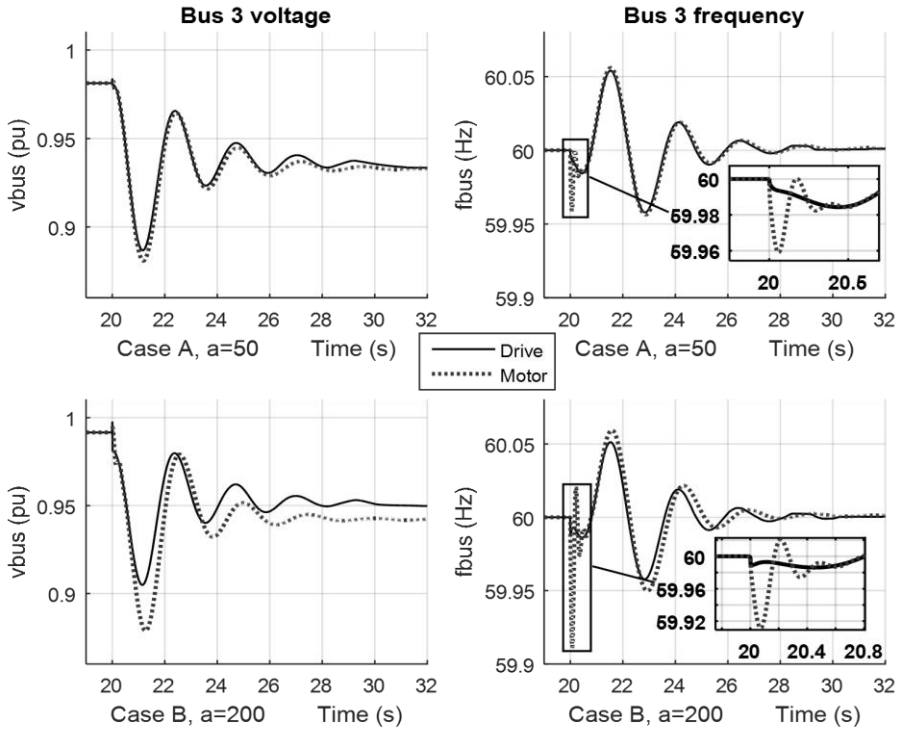

Figure 4.17 **Cases A and B**: Bus 3 Voltage and Frequency

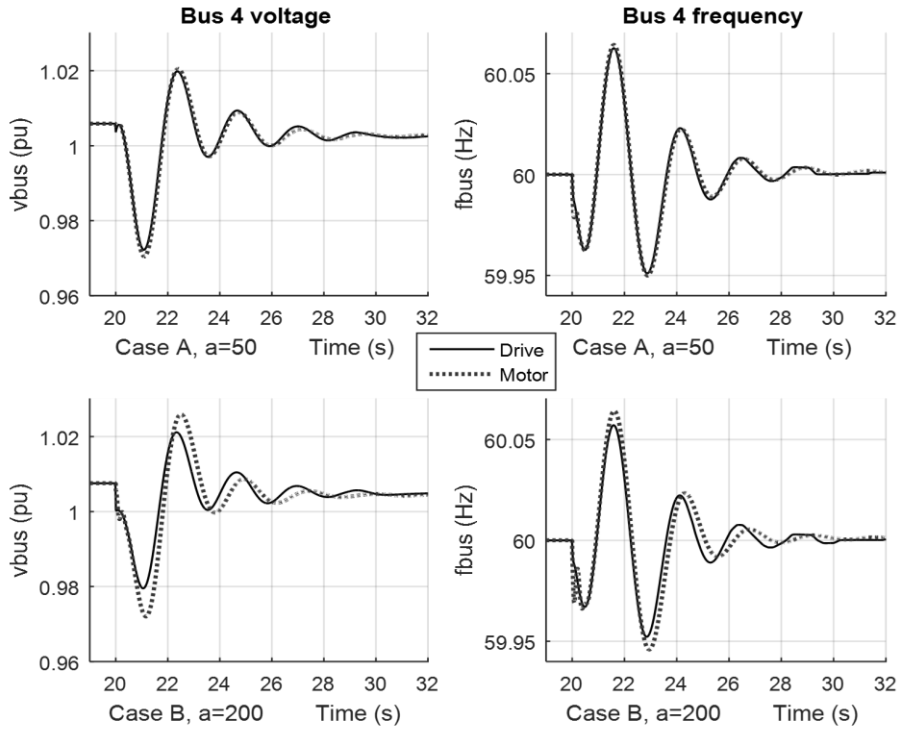

Figure 4.18 **Cases A and B**: Bus 4 Voltage and Frequency

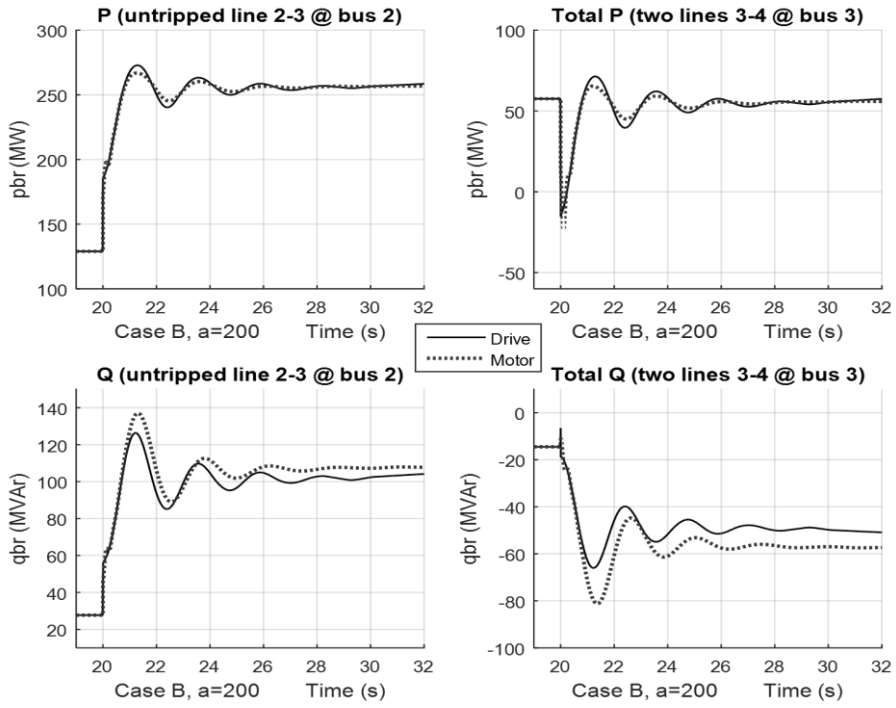

Figure 4.19 **Case B**: *P* and *Q* on the Untripped Line Flowing from Bus 2 to Bus 3, Measured at Bus 2 (left two subplots); the Total *P* and *Q* Flowing from Bus 3 to Bus 4, Measured at Bus 3 (Right Two Subplots)

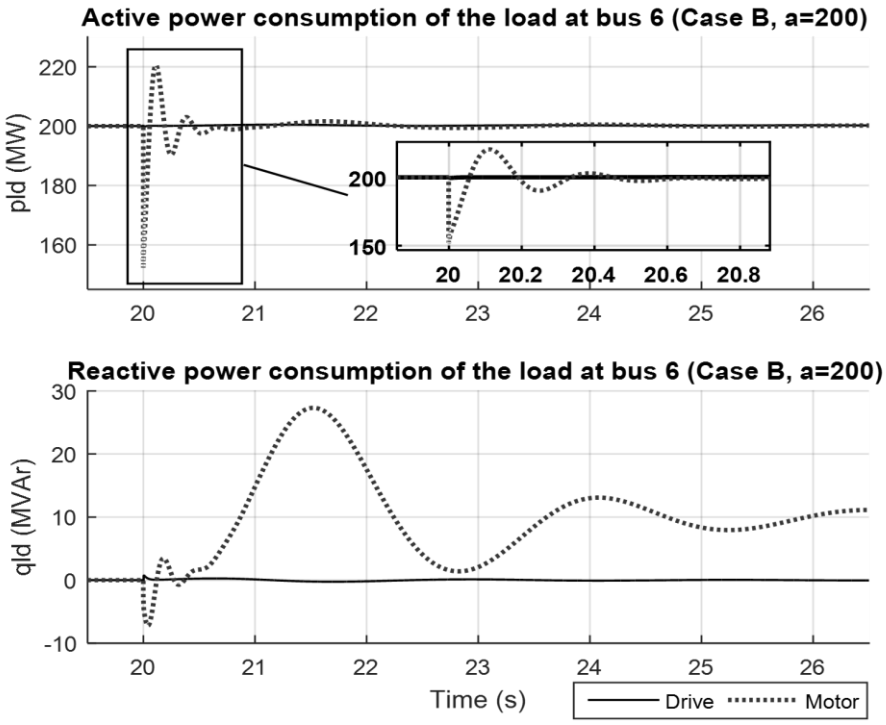

Figure 4.20 **Case B**: Active and Reactive Power Consumptions of the Load at Bus 6

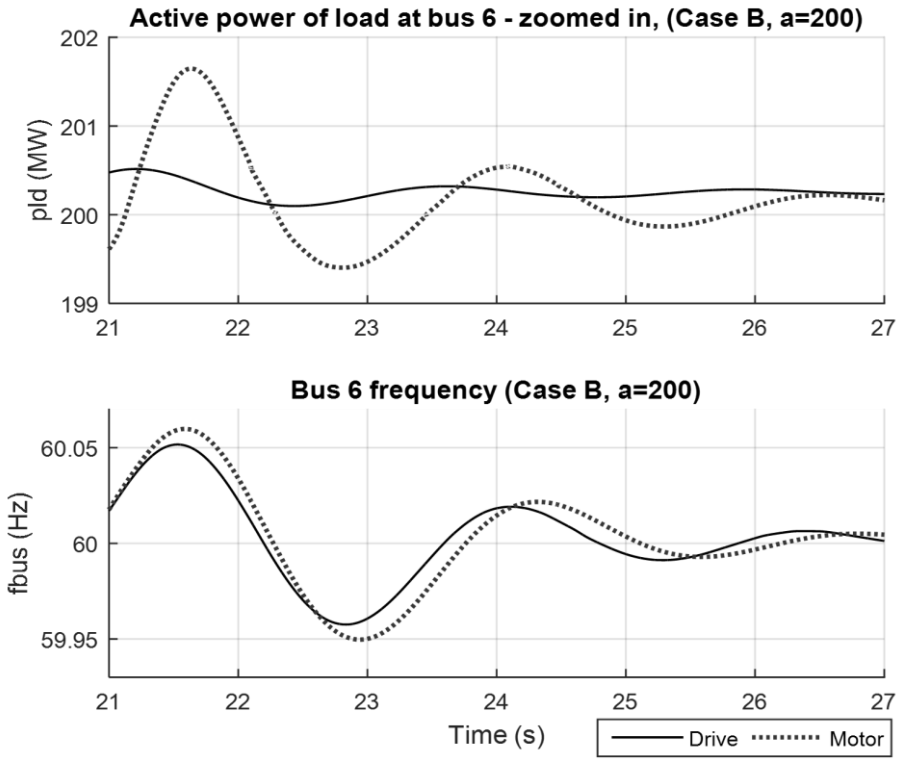

Figure 4.21 **Case B**: Active Power Consumption of the Load (in Narrow Time Scale) and the Frequency at Bus 6

It can be seen from Figure 4.16 to Figure 4.21 that a 0.38 Hz inter-area oscillation [6], [57] is excited following the line outage contingency. The following observations are made.

- The damping effects of the drive load on oscillations of bus voltages are slightly better than that of the motor load especially during the first swing of the oscillation, seen from the left two subplots in Figure 4.16 through Figure 4.18.
- The damping effects of the drive load on oscillations of bus frequencies are similar to that of the motor load, seen from the right two subplots in Figure 4.16 through Figure 4.18. The driven load of the direct-connected motor varies with the square of the speed, while the electronically connected load is controlled to constant speed and hence constant power.

- The damping effects of the two types of loads do not show great difference with a small amount (50 MW) of load located in the middle of the system. Nevertheless, with large amount (200 MW) of motor or drive loads aggregated in the middle, the drive load manifests superior damping effects on system voltage oscillations.
- Figure 4.17 shows that the post-contingency stabilized voltages at Bus 3 for both drive and motor cases are lower than the pre-contingency values. This occurs because the total impedance between Bus 2 and 3 becomes larger after one tie-line is tripped, which will cause more voltage drop across the line. The Bus 3 voltage for the motor case is even lower than the drive case mainly because the motor model absorbs positive reactive power after the system stabilizes (see Figure 4.20).
- Figure 4.19 exhibits the power flows on the tie lines when the mid-point load is 200 MW. The motor load shows similar (negligibly better) damping effects on oscillations of active power flows on the lines compared to the drive load. It is noticed that the motor load has a damping factor of 2.0 pu. However, the drive load demonstrates visibly better damping effects on oscillations of reactive power flows.
- The direct-connected motor exhibits a high-frequency transient of active and reactive power (see Figure 4.20). Following the initial fast transients, the motor and drive loads have asymptotic low-frequency oscillations of active power. The reactive power consumption is varying for the case of motor load and is nearly constant for the case of drive load (see lower subplot of Figure 4.20).
- For the motor load, Figure 4.21 shows that the oscillation of the active power consumption is almost in phase with the oscillation of frequency, which indicates large damping torque and nearly zero synchronizing torque provided by the motor load. For

the drive load, Figure 4.21 shows that there is a nearly 45 degrees phase shift between the oscillations of the active power and frequency, which implies desirable damping and synchronizing torques are provided by the drive load.

4.6.3 Application 2: Multiple Mixed Loads

In Application 2, the test of multiple mixed load models is performed on the standard IEEE 39-bus New England System [4] shown by Figure 4.22. The original static loads located at Buses 3, 4, 15, 16, 18 and 27 are replaced by the mixed load models that comprise of varying percentages of drive and motor components. The other static loads in the system are modified to have constant current characteristic for active power and constant impedance characteristic for reactive power. Table 4.3 selects two typical line outage contingencies to demonstrate the system responses considering different levels of penetration of the drive component. Uniform composition percentages as indicated in Table 4.3 are applied to all the six mixed load blocks. The two lines selected to be tripped have similar impedances and different active power flows. This simulation scenario also investigates the system damping effects with respect to the loading level of the tripped line. The simulation results are presented in Figure 4.23 and Figure 4.24.

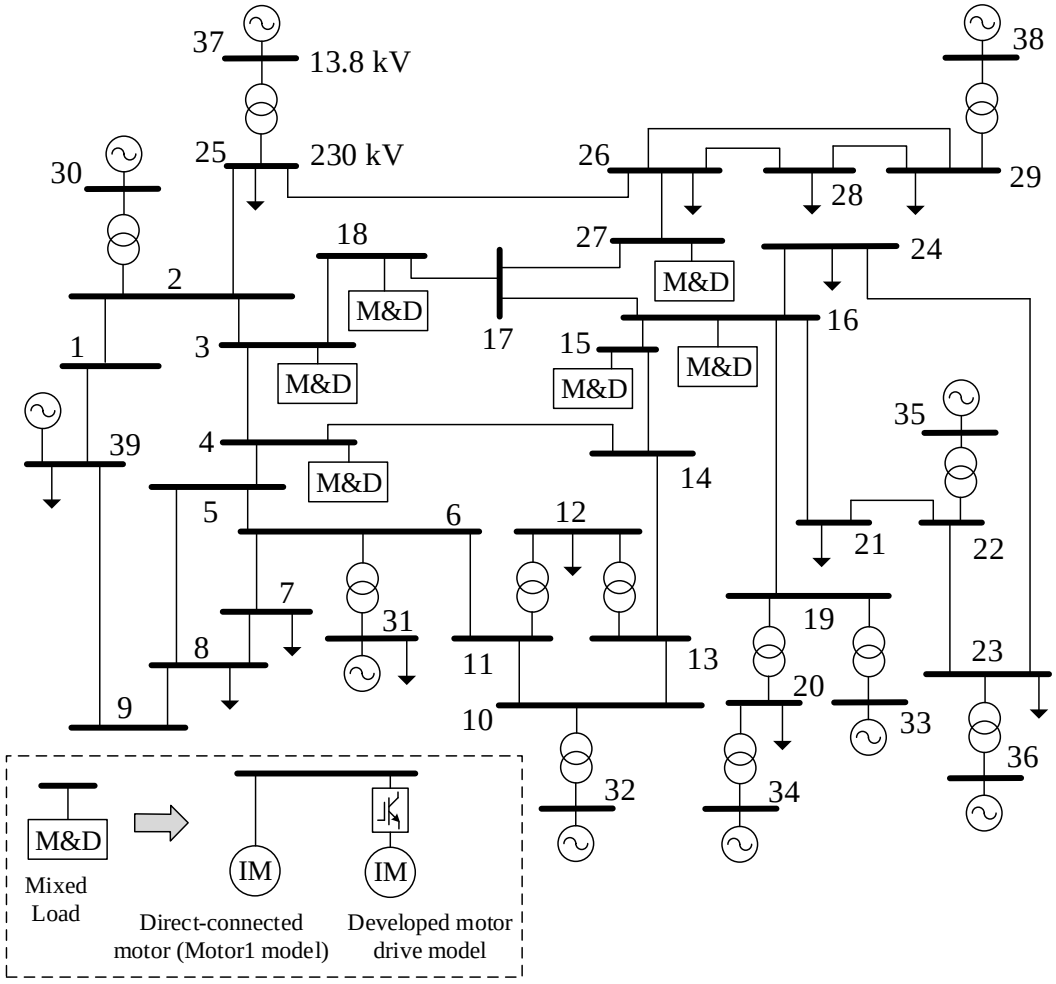

Figure 4.22 IEEE 39-Bus New England System

Table 4.3 Selected Cases of Contingency

Trip Line	Flow	Impedance (pu)	Mixed Load
16-17	208 MW 16→17	0.0007 + j0.0089	20% Drive + 80% Motor
			80% Drive + 20% Motor
17-18	174 MW 17→18	0.0007 + j0.0082	20% Drive + 80% Motor
			80% Drive + 20% Motor

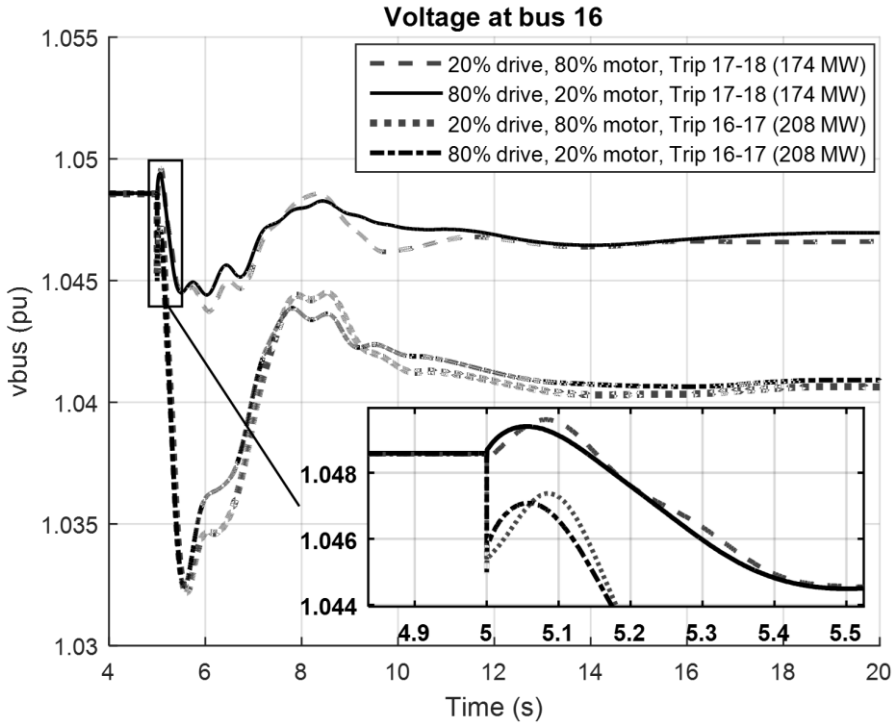

Figure 4.23 Bus 16 Voltage

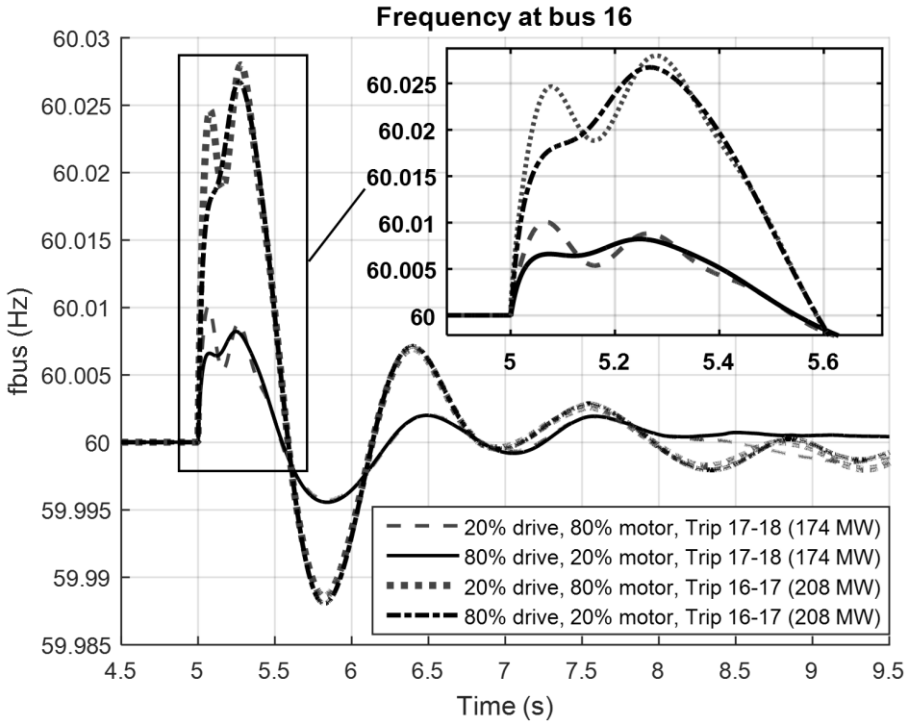

Figure 4.24 Bus 16 Frequency

It is observed from Figure 4.23 and Figure 4.24 that with higher percentage of drives (80%) in the composite load, the system exhibits better damping effects on voltages and similar damping effects on frequencies compared to the case of higher percentage of motor. The outage of a more stressed line will cause the system voltages and frequencies to oscillate more severely and will deteriorate the system damping effects.

In general, both motor and drive loads have damping effects on low-frequency oscillations of system voltage and frequency. The two loads yield comparable damping of frequency but different degrees of damping of voltage. The degree of damping effects hinges on the oscillation mode, the proportion of motor or drive load, the location and distribution of the motor or drive load and the power flow stress on the tie lines.

Chapter 5. POSITIVE-SEQUENCE TRANSIENT DRIVE MODEL

5.1 Introduction

In Chapter 4, the development of performance-based drive load model is discussed. It has been emphasized that the performance-based model is suitable for investigations on small-magnitude low-frequency system oscillations. In this chapter, a novel complete drive model is proposed to investigate the system performances subject to large disturbances such as voltage depressions. Compared to the detailed drive model in the three-phase EMT programs, the complexity of the transient drive model in the PSTS simulation programs is simplified to avert numerical instability. Nevertheless, the accuracy is reasonably well maintained.

The transient model of vector-controlled drive is developed from the dynamic equations of the motor drive system. On the line side, the decomposed *d-q* vector controls are exercised to generate command voltage signals to regulate the interfaced rectifier modeled as a voltage source to maintain desired power factor. The *dc*-link of the double-sided converter is implemented based upon the power balance equation and voltage differential equation of the capacitor, which models the intermediate stage to represent the grid-side rectifier and the machine-side inverter. On the machine side, the rotor flux oriented control is actualized to calculate the *dc*-link output current. The acquisition of this *dc*-link output current is pivotal in the model development because it acts as a juncture between the rectifier and inverter. As a resolution, the average model of converter is adopted to facilitate the calculation. In this chapter, details about the model development will be addressed. Voltage depression contingencies will be applied on systems of different

sizes to validate the performance of the model and to explore the system characteristics with different levels of penetration of the modern *ac* motor drives.

5.2 The Complete Vector-Controlled Transient Drive Model

The schematic of the detailed three-phase EMT motor drive model similar to Figure 4.1 has been presented in Figure 5.1. This model serves as a prototype system for the positive-sequence drive model to be represented, and is used for validation of the developed model. In Figure 5.1, the line-side control system encloses *dc*-link voltage controller and *d*-*q* axes line currents controllers. The machine-side control system includes rotor flux and rotor speed controllers, and the *d*-*q* axes stator currents controllers. These controllers formulate basic configuration of a vector-controlled drive system. More functional controllers (e.g. drive terminal voltage regulator) can be inserted, and will be discussed in later sections. The average model of PWM converter [28] is utilized to implement the rectifier and inverter in this EMT drive model.

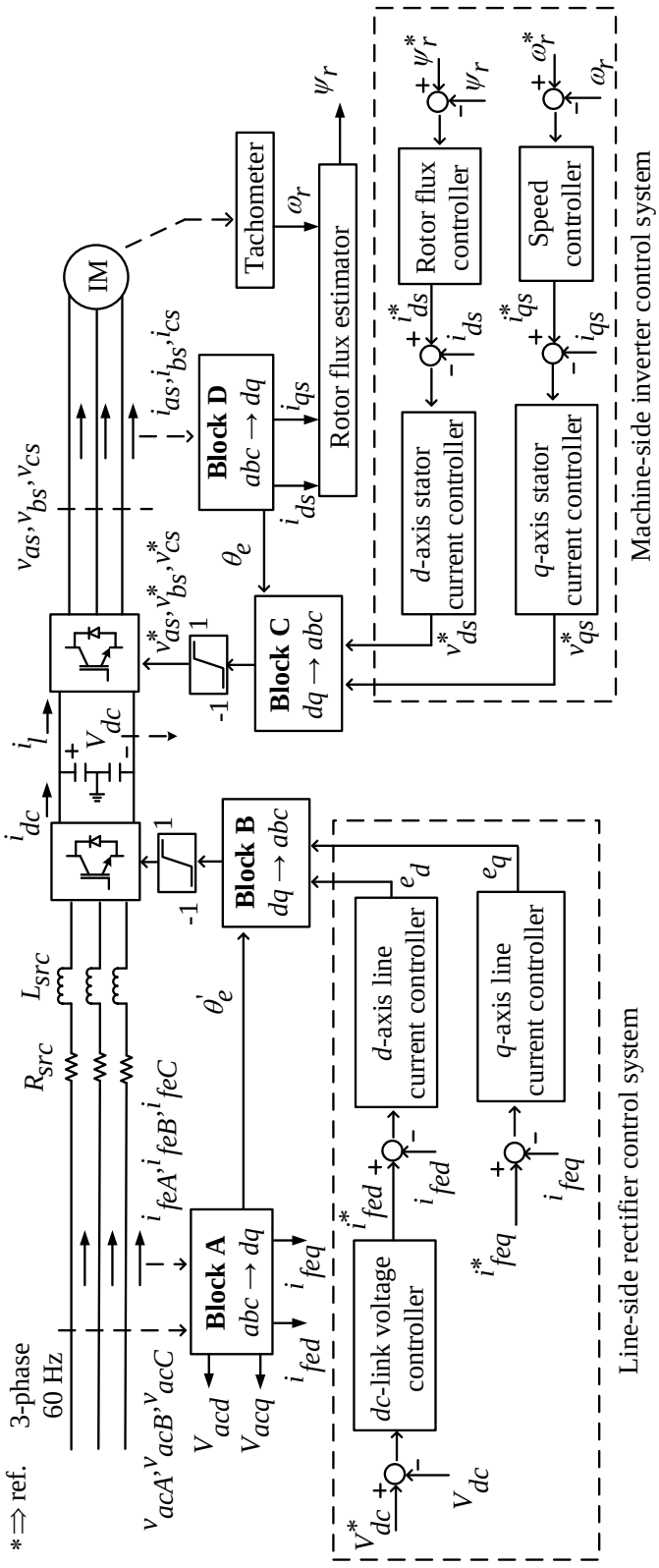

Figure 5.1 Schematic of the EMT Drive Model to be Represented in the PSTS Program

The key point to develop the positive-sequence model is to reduce the balanced three-phase electrical system into *d-q* axes formation and implement corresponding *d-q* axes controls. To achieve this goal, the *abc-dq* reference transformations require to be eliminated. It is noticed in Figure 5.1 that Block A obtains measured three-phase voltages and currents signals, and calculates reference transformation angle θ_e' and *d-q* axes quantities [14]. θ_e' is also used by Block B to transform the *d-q* axes reference voltages into three-phase signals to command the rectifier. Therefore, to develop the positive-sequence model, the two mutually inverse transformations labeled by Blocks A and B can nullify each other. Similarly, the machine-side Blocks C and D cancel each other. It is a fact that the tachometer and rotor flux estimator in Figure 5.1 have negligible response time, and they can be neglected for developing the positive-sequence model.

The implementation of the positive-sequence motor drive model is presented in Figure 5.2. Similar rectifier and inverter control systems are used for the models depicted by Figure 5.1 and Figure 5.2. Comparing these two figures, it is known that the rectifier of the drive is the direct interface to the electrical network. For a balanced system, the rectifier can be represented in PSTS programs by a positive-sequence phasor-form voltage source in which the real and imaginary components of the internal voltages are manipulated by rectifier control system. In Figure 5.2, the inverter is modeled as a pure gain block. The detailed implementation of the grid-side and machine-side control systems, *dc*-link block and induction motor model will be covered in following sections.

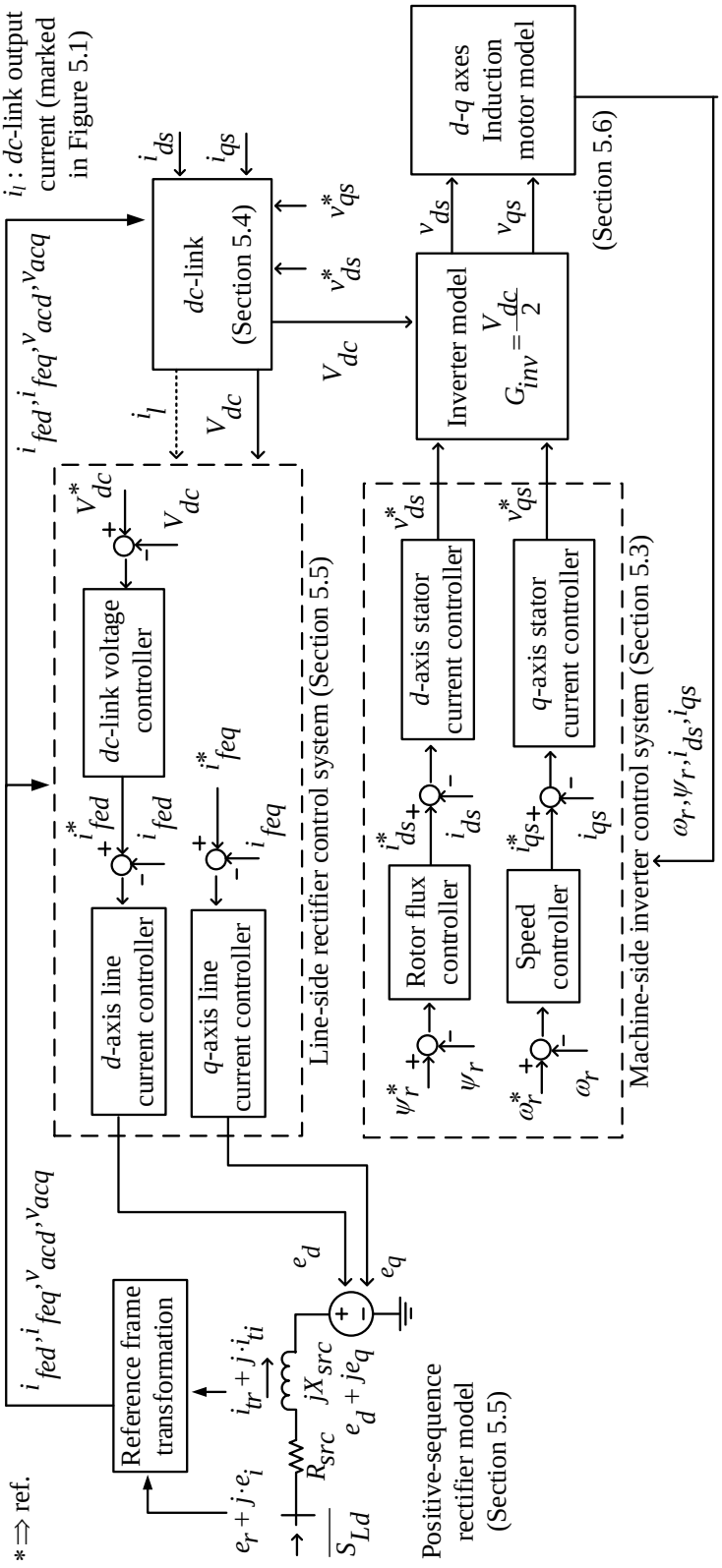

Figure 5.2 Positive-Sequence Motor Drive Model

5.3 Machine-Side Inverter Control System of the Transient Drive Model

The rotor flux oriented control for the inverter supplying a driven motor is developed based on orienting the *d*-axis of the rotating reference frame to align the rotor flux vector, and controlling the magnitude of rotor flux, the speed of rotor and the *d*-*q* axes stator currents [14], [19]. This control technique has been introduced in the development of the EMT drive model in Section 3.4 of Chapter 3. The controller models of the EMT and positive-sequence drives are identical seen from Figure 5.1 and Figure 5.2. The depiction of the detailed inverter control system is given by Figure 5.3. Optional compensation terms can be added at the output ports of the *d*-*q* axes stator currents controllers to improve the dynamic performance of the inverter control [19]. The output *d*-*q* axes reference voltages are fed to the inverter model as shown in Figure 5.2.

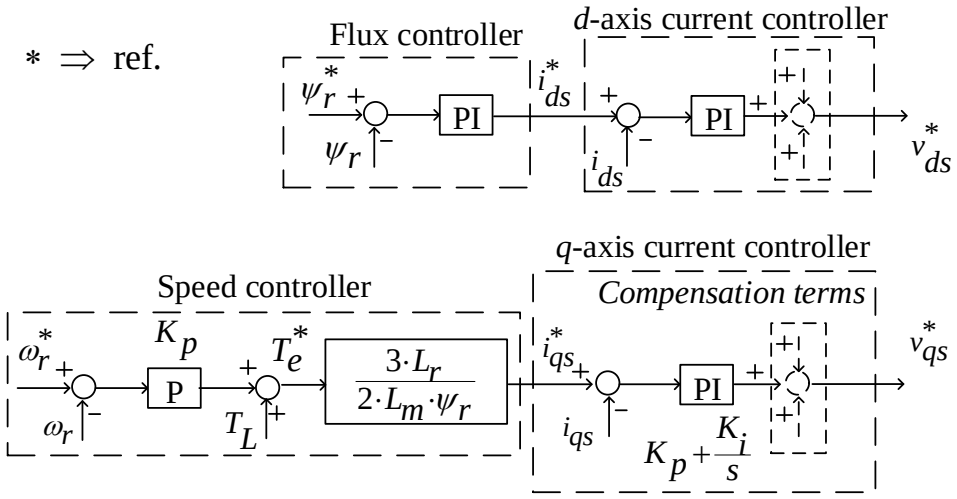

Figure 5.3 Machine-Side Inverter Control System

5.4 Implementation of *dc*-Link

The implementation of the *dc*-link block in Figure 5.2 is divided into two parts. The first part deduces the equation for calculating the *dc*-link output current i_l from the average

model of PWM converter. The second part describes the linkage of i_l to the *ac*-side electrical variables through the dynamic equation of *dc*-link capacitor. The three-phase average model of PWM converter is depicted in Figure 5.4. A similar schematic has been given in Figure 3.12.

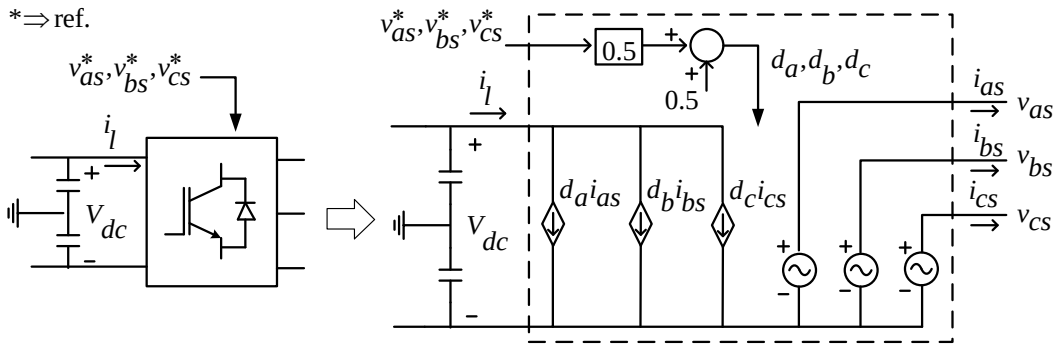

Figure 5.4 Average Model of PWM Converter

The *dc*-link output current i_l can be calculated using matrix operations by (5.1).

$$i_l = \begin{bmatrix} d_a & d_b & d_c \end{bmatrix} \begin{bmatrix} i_{as} & i_{bs} & i_{cs} \end{bmatrix}^{\mathrm{T}} \tag{5.1}$$

$$\begin{bmatrix} d_a & d_b & d_c \end{bmatrix} = \begin{bmatrix} 1/2 & 1/2 & 1/2 \end{bmatrix} + 1/2 \cdot \begin{bmatrix} v_{as}^* & v_{bs}^* & v_{cs}^* \end{bmatrix} \tag{5.2}$$

where, d_a, d_b and d_c represent the instantaneous three-phase duty ratios. v_{as}^*, v_{bs}^* and v_{cs}^* denote the normalized three-phase reference voltages to the converter. i_{as}, i_{bs} and i_{cs} indicate the converter *ac*-side three-phase currents, which are fed to the stator of the motor. For a balanced three-phase system, the three-phase stator currents sum up to zero as shown by (5.3).

$$i_{as} + i_{bs} + i_{cs} = 0 \tag{5.3}$$

Thus, i_l can be calculated by combining (5.1) – (5.3) to be

$$i_l = 1/2 \cdot \begin{bmatrix} v_{as}^* & v_{bs}^* & v_{cs}^* \end{bmatrix} \begin{bmatrix} i_{as} & i_{bs} & i_{cs} \end{bmatrix}^{\mathrm{T}} \tag{5.4}$$

Typical *dq-to-abc* transformation [19] is applied to the reference voltages and stator currents by (5.5) – (5.7).

$$\begin{bmatrix} v_{as}^* & v_{bs}^* & v_{cs}^* \end{bmatrix}^{\mathrm{T}} = \mathbf{K_p} \begin{bmatrix} v_{ds}^* & v_{qs}^* \end{bmatrix}^{\mathrm{T}} \tag{5.5}$$

$$\begin{bmatrix} i_{as} & i_{bs} & i_{cs} \end{bmatrix}^{\mathrm{T}} = \mathbf{K_p} \begin{bmatrix} i_{ds} & i_{qs} \end{bmatrix}^{\mathrm{T}} \tag{5.6}$$

$$\mathbf{K_p} = \frac{2}{3} \begin{bmatrix} 1 & -1/2 & -1/2 \\ 0 & \sqrt{3}/2 & -\sqrt{3}/2 \end{bmatrix}^{\mathrm{T}} \begin{bmatrix} \cos\theta_e & -\sin\theta_e \\ \sin\theta_e & \cos\theta_e \end{bmatrix} \tag{5.7}$$

Where, $\mathbf{K_p}$ has already been defined in the same form as $\mathbf{K_{r2}}$ in (3.13b). θ_e is the transformation angle between these two reference frames. v_{ds}^* and v_{qs}^* denote the *d-q* axes reference voltages to the inverter model; i_{ds} and i_{qs} indicate the *d-q* axes stator currents, as shown in Figure 5.2.

Transposing (5.5) and substituting with (5.6) into (5.4) generates

$$i_l = 1/2 \begin{bmatrix} v_{ds}^* & v_{qs}^* \end{bmatrix} \mathbf{K_p^T K_p} \begin{bmatrix} i_{ds} & i_{qs} \end{bmatrix}^{\mathrm{T}} \tag{5.8}$$

It is noted from (5.7) that

$$\mathbf{K_p^T K_p} = \frac{2}{3} \begin{bmatrix} 1 & 0 \\ 0 & 1 \end{bmatrix} \tag{5.9}$$

Combining (5.8) and (5.9), the *dc*-link output current can be calculated as

$$i_l = 1/3 \cdot \left(v_{ds}^* \cdot i_{ds} + v_{qs}^* \cdot i_{qs} \right) \tag{5.10}$$

After the *dc*-link output current is derived to associate the machine-side variables as shown in (5.10), the linkage between the *dc*-link and line-side electrical variables will be found. Neglecting the dissipation in the line-side impedance, the line-side *d-q* axes voltages and currents can be related to the *dc*-link voltage V_{dc} and input current i_{dc} through power balance equation [4] given by

$$v_{acd} i_{fed} + v_{acq} i_{feq} = V_{dc} i_{dc} \tag{5.11}$$

As shown in Figure 5.1 and Figure 5.2, v_{acd} and v_{acq} are the line-side *d*-*q* axes voltages. i_{fed} and i_{feq} are the *d*-*q* axes line currents. There is also a differential equation associating with the *dc*-link capacitor, which is

$$i_{dc} = \left(B_C / \omega_B\right)\left(dV_{dc} / dt\right) + i_l \tag{5.12}$$

where, B_C is the susceptance of the *dc*-link capacitor normalized based on the line-side base admittance. ω_B is the base angular frequency on the line-side.

The *dc*-link block can be implemented by combining (5.10) – (5.12), and illustrated by Figure 5.5.

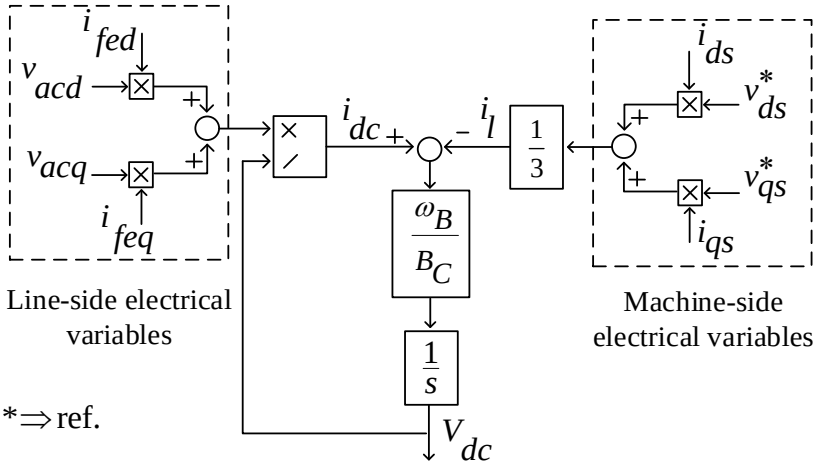

Figure 5.5 Block Diagram of *dc*-Link in the Positive-Sequence Drive Model

5.5 Grid-Side Rectifier Control System of the Transient Drive Model

The positive sequence representation of the balanced three-phase rectifier can be equivalenced as a voltage source in PSTS programs as shown in Figure 5.6. For this voltage source equivalence, the grid-side voltage $\overline{\mathbf{V}_{\mathbf{ac\_rl}}}$ and current $\overline{\mathbf{I}_{\mathbf{fe\_rl}}}$ are evaluated internally using EPCL functions and referred to system reference frame. In order to produce the

reference voltage $\overline{\mathbf{V}_{\mathbf{fe}}}$ under the model reference frame, the controllers inputs $\overline{\mathbf{V}_{\mathbf{ac\_ri}}}$ and $\overline{\mathbf{I}_{\mathbf{fe\_ri}}}$ need to be transformed into the model reference variables denoted by $\overline{\mathbf{V}_{\mathbf{ac}}}$ and $\overline{\mathbf{I}_{\mathbf{fe}}}$. This transformation is illustrated by Figure 5.7 and specified by (5.13) – (5.16). For convenience, the *d*-axis of the model reference frame is directed to align with the grid-side voltage space vector $\overline{\mathbf{V}_{\mathbf{ac\_ri}}}$ by calculating the boundary variable α in (5.16).

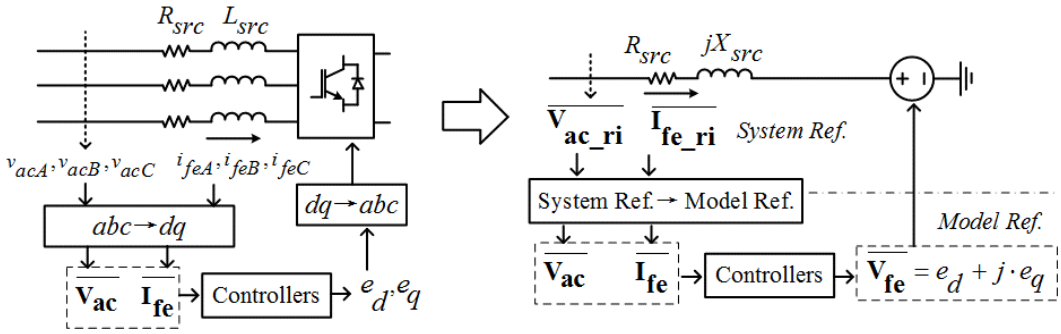

Figure 5.6 Voltage Source Equivalence of Line-Side Rectifier

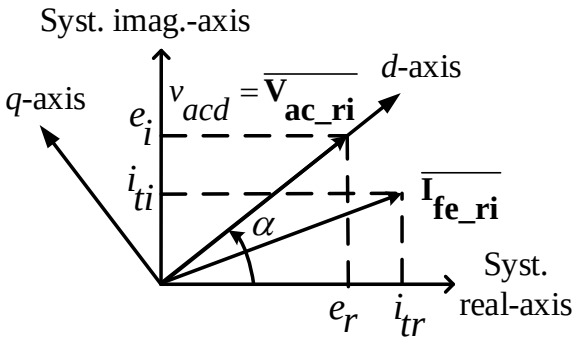

Figure 5.7 Transformation between System and Model Reference Frames

$$\overline{\mathbf{V}_{\mathbf{ac}}} = v_{acd} + j \cdot v_{acq} = e^{-j\alpha} \overline{\mathbf{V}_{\mathbf{ac\_ri}}} = e^{-j\alpha} \left(e_r + j \cdot e_i \right) \tag{5.13}$$

$$\overline{\mathbf{I}_{\mathbf{fe}}} = i_{fed} + j \cdot i_{feq} = e^{-j\alpha} \overline{\mathbf{I}_{\mathbf{fe\_ri}}} = e^{-j\alpha} \left(i_{tr} + j \cdot i_{ti} \right) \tag{5.14}$$

$$\overline{\mathbf{V}_{\mathbf{fe}}} = e_d + j \cdot e_q \tag{5.15}$$

$$\alpha = \sin^{-1} \left(e_i \Big/ \sqrt{e_r^2 + e_i^2} \right) \tag{5.16}$$

in which, e_r and e_i are the real and imaginary components of the grid-side phasor voltage. i_{tr} and i_{ti} are the real and imaginary parts of the phasor line current. These four variables are obtained using EPCL functions and are defined w.r.t. the system reference frame. e_d and e_q are the internal source *d*-*q* axes voltages under model reference frame, and need to be obtained from the rectifier control system.

The dynamic differential equation of the voltage source interface under model reference frame can be expressed in phasor form by (5.17).

$$\overline{\mathbf{V_{fe}}} = \overline{\mathbf{V_{ac}}} - R_{src}\overline{\mathbf{I_{fe}}} - \left(X_{src}/\omega_B\right)\left(d\overline{\mathbf{I_{fe}}}/dt\right) \tag{5.17}$$

Under the reference frame illustrated by Figure 5.7, the *q*-axis component of $\overline{\mathbf{V_{ac}}}$, denoted by v_{acq}, becomes zero. Substituting (5.13) – (5.15) into (5.17) and equating the real and imaginary parts give

$$e_d = v_{acd} - R_{src}i_{fed} - \left(X_{src}/\omega_B\right)\left(di_{fed}/dt\right) \tag{5.18}$$

$$e_q = -R_{src}i_{feq} - \left(X_{src}/\omega_B\right)\left(di_{feq}/dt\right) \tag{5.19}$$

The differential equation associated with the *dc*-link can be derived from (5.11), (5.12) and $v_{acq} = 0$, and shown by

$$v_{acd}i_{fed}/V_{dc} = \left(B_C/\omega_B\right)\left(dV_{dc}/dt\right) + i_l \tag{5.20}$$

The rectifier control system can be formulated from the differential equations (5.18) – (5.20) and presented in Figure 5.8. The active power consumption of the drive is regulated by holding the *dc*-link voltage unchanged and adjusting the *d*-axis current to react to specific disturbances. The *q*-axis line current controller maneuvers the reactive power import or export of the drive.

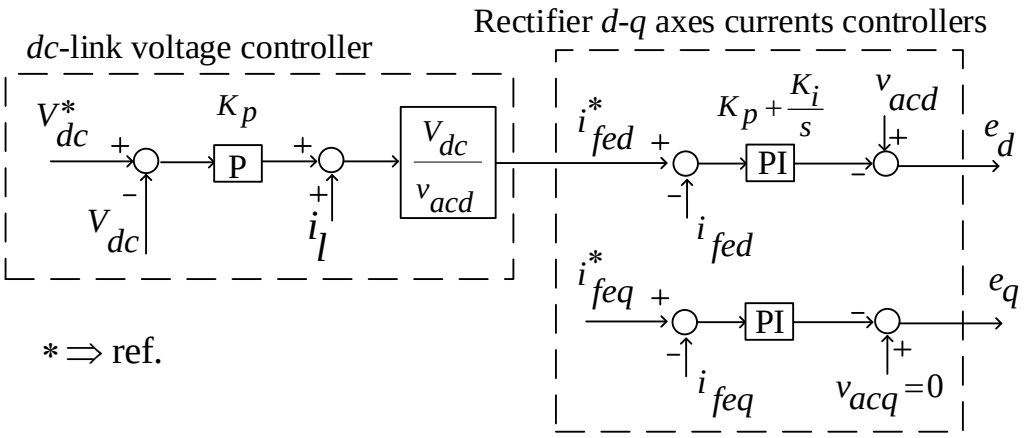

Figure 5.8 Line-Side Rectifier Control System

5.6 Driven Motor Model for the PSLF Transient Drive

As shown in Figure 5.2, the driven motor for this PSLF drive model is reduced to *d-q* axes representation by eliminating the *abc-dq* transformation with the controller model. The single-cage induction motor is considered. The block diagram of the motor model can be derived from the standard dynamic equations of induction motor as covered in Section 3.3 of Chapter 3. The *d-q* axes induction motor model in rotor flux coordinates can be developed from (3.33a), (3.33b) (3.38), (3.42) and (3.43), and (3.47) – (3.49). The block diagram of the motor model is presented by Figure 5.9.

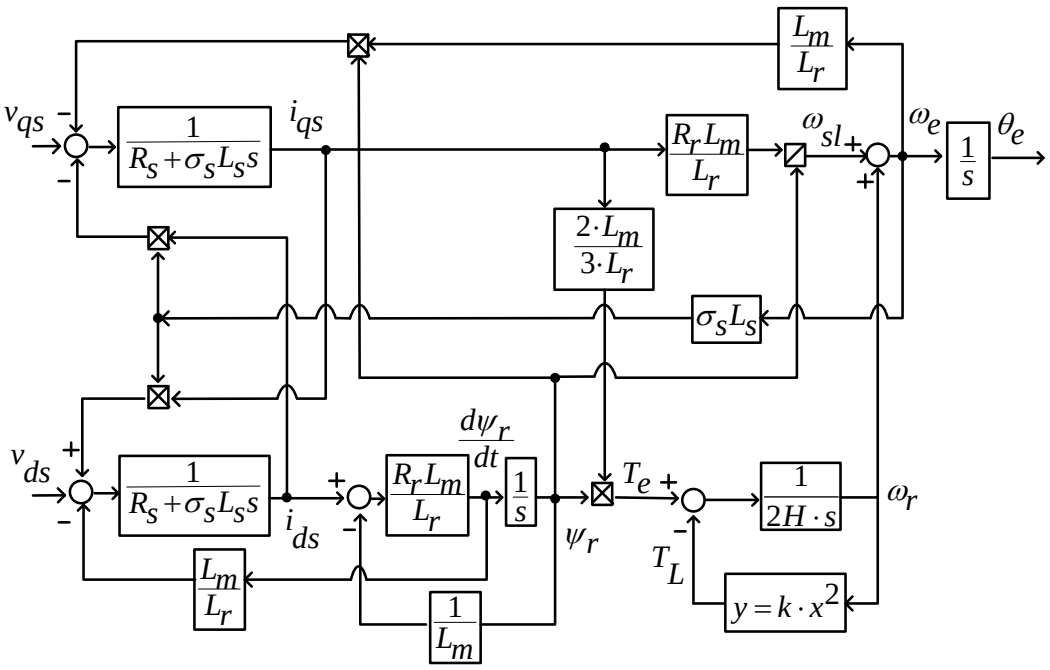

Figure 5.9 *d-q* Axes Induction Motor Model in Rotor Flux Coordinates

According to Figure 5.2, the rotor speed, rotor flux and *d-q* axes stator currents are monitored from the motor model in Figure 5.9 and transmitted to the inverter controllers. The *d-q* axes stator currents are also used in the implementation of the *dc*-link block.

5.7 Simulation Scenario I: Comparing PSLF and PSCAD Models

Two simulations are performed in this Scenario I to compare the PSLF transient drive model and the PSCAD detailed drive model. These two simulations are conducted on a standard IEEE 9-bus system [47] with pertinent modifications.

The modified IEEE 9-bus system is presented in Figure 5.10. The original constant impedance load on Bus 6 is replaced by a vector-controlled motor drive load connected to this bus through a step-down transformer. The reactive power absorption of the drive is regulated to be zero by line-side rectifier controls. The generator G1 on Bus 1 is idealized

to be an infinite voltage source representing the robust external grid. This equivalencing facilitates the ability to apply different voltage contingencies on the localized system.

The simulation without applying contingency is performed first to examine the simulation efficiency of the PSLF and PSCAD drive models in the two simulators. The results are presented in Table 5.1. Following that, two cases of simulation are performed in Sections 5.7.1 and 5.7.2 separately to verify the similar performance of the PSLF drive model with the PSCAD model. The simulations in this chapter are executed with time steps of 100 us in PSCAD and 420 us in PSLF.

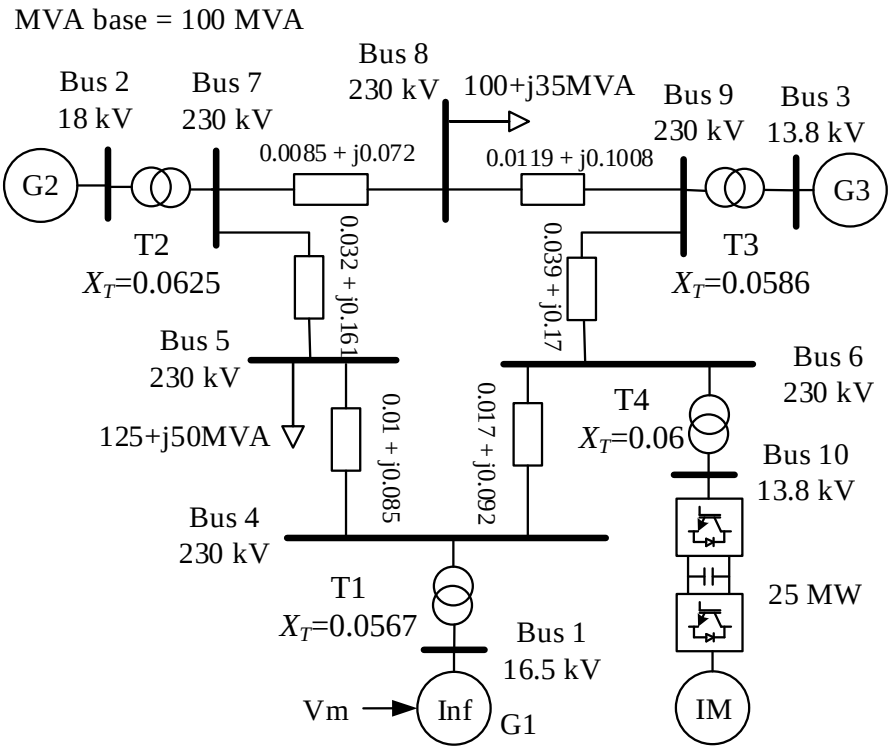

Figure 5.10 Modified IEEE 9-Bus System

Table 5.1 Comparison of Simulation Speed

Simulation length = 2 s			
Drive model	Simulator	Model solution time step	Time elapsed
EMT	PSCAD	100 us (max)	10.0 s
Positive-sequence	PSLF	100 us	3.96 s
		420 us	1.04 s
		1050 us (max)	0.4 s

5.7.1 Voltage Depression

The first collection of comparisons exhibits the response of the drive subject to a voltage dip scenario. It is assumed that a fault occurring somewhere in the external system induces a voltage dip on Bus 1 to 70% of its operating value. The voltage magnitude is depressed for 12 cycles and forced back to 90% of nominal value after the clearance of fault. The detailed PSCAD drive system is constructed using built-in electrical components and user-written controller transfer functions. The simplified PSLF drive model is implemented exclusively by transfer functions. The behavioral responses of these two models are compared. The detailed parameters of control and drive systems used in Section 5.7.1 are attached in Table A.0.5 in the APPENDIX A.

The simulation results are shown in Figure 5.11 through Figure 5.21, in which related line-side and machine-side electrical variables are plotted. In some of these figures, corresponding PSCAD results and PSLF results are plotted on the same graphs for clear comparison. All the variables in per-unit are normalized on the line-side basis.

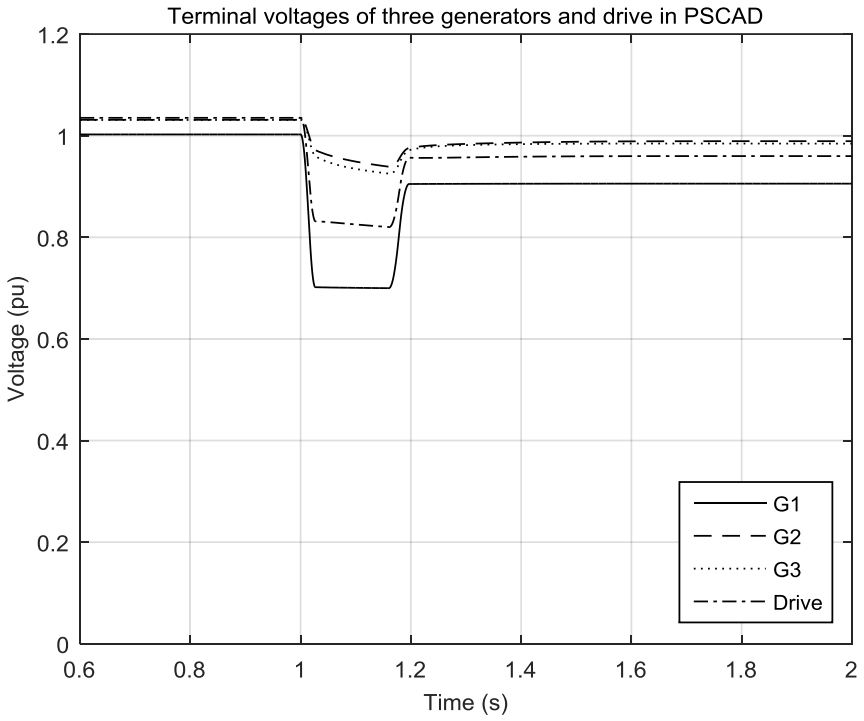

Figure 5.11 Terminal Voltages of the Three Generators and the Drive Simulated in PSCAD

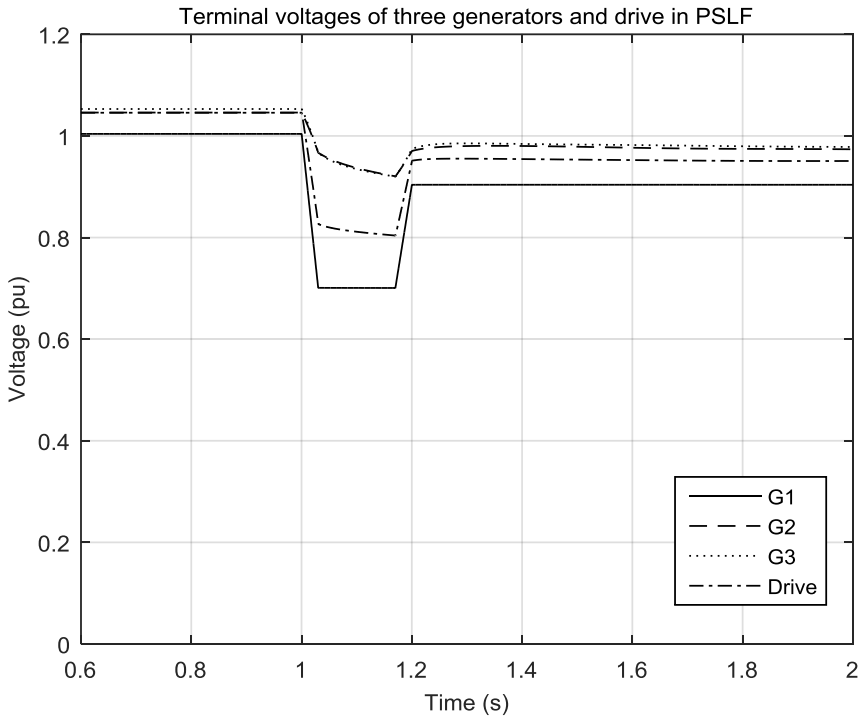

Figure 5.12 Terminal Voltages of the Three Generators and the Drive Simulated in PSLF

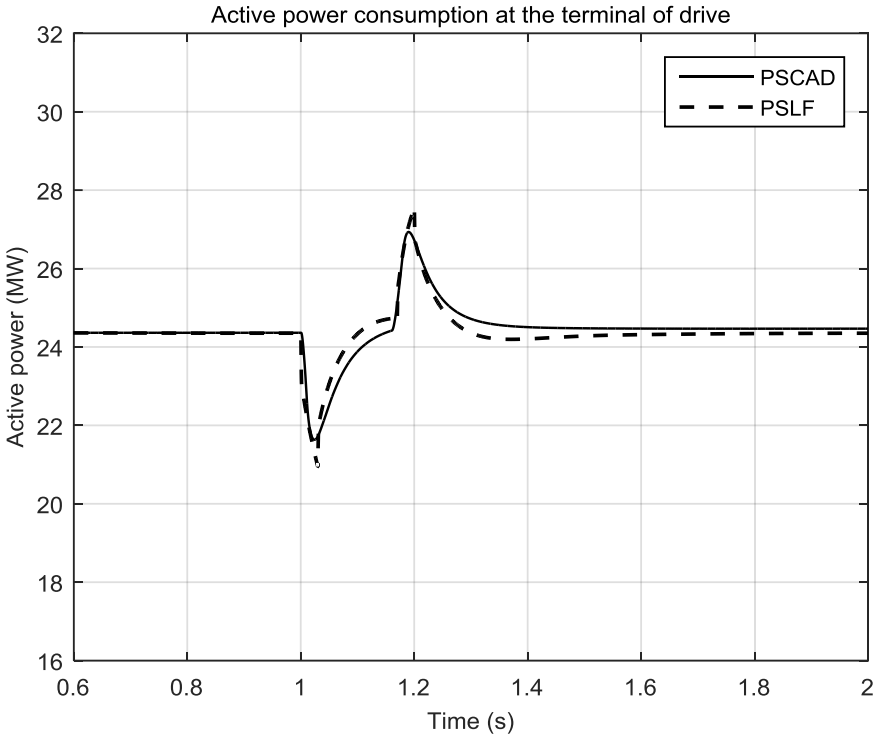

Figure 5.13 Active Power Consumption at the Terminal of the Drive

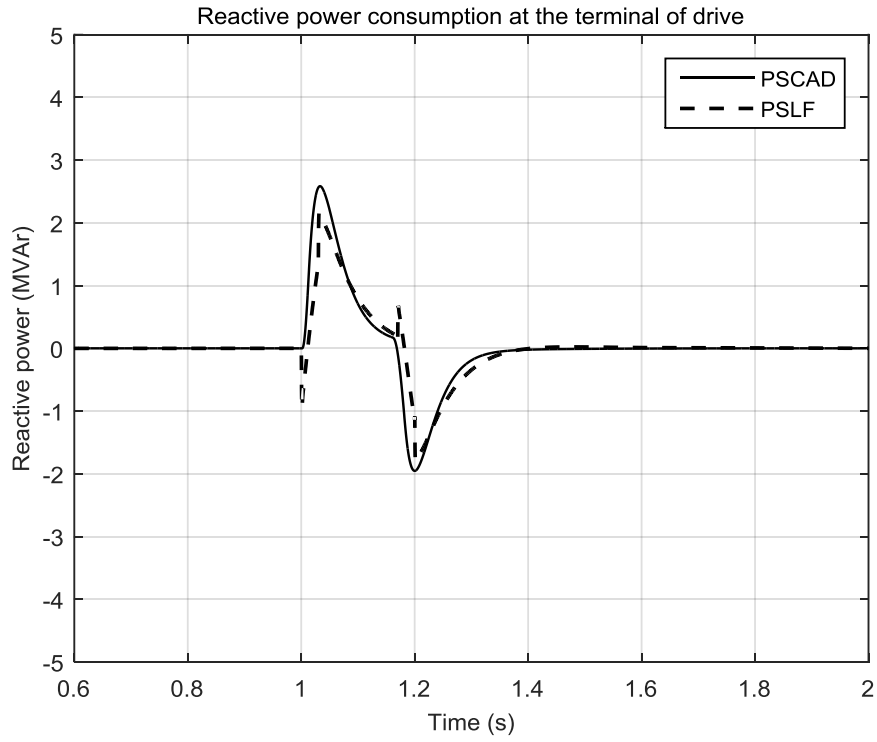

Figure 5.14 Reactive Power Consumption at the Terminal of the Drive

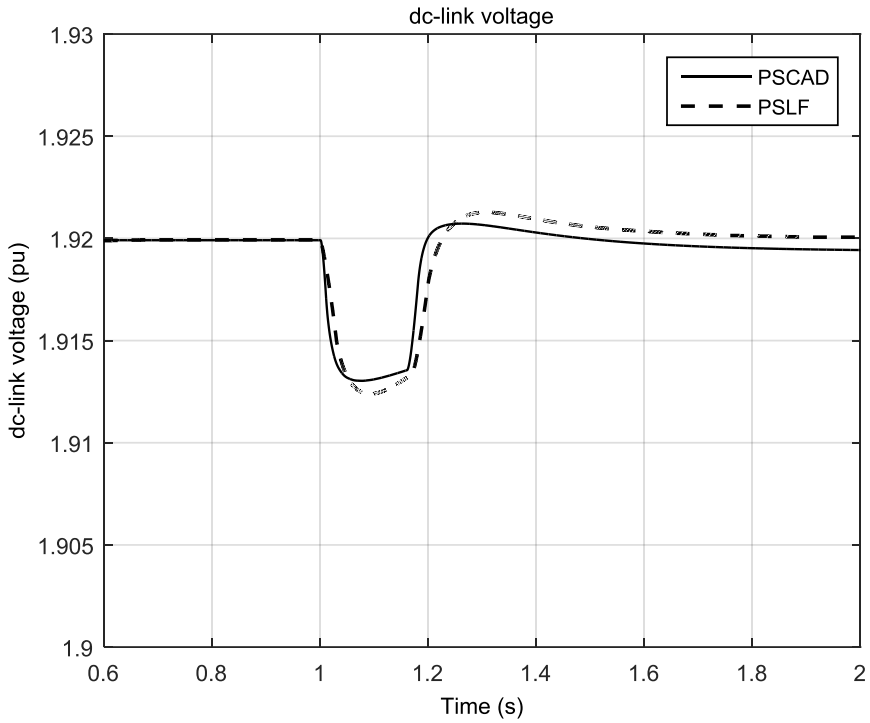

Figure 5.15 *dc*-Link Voltage

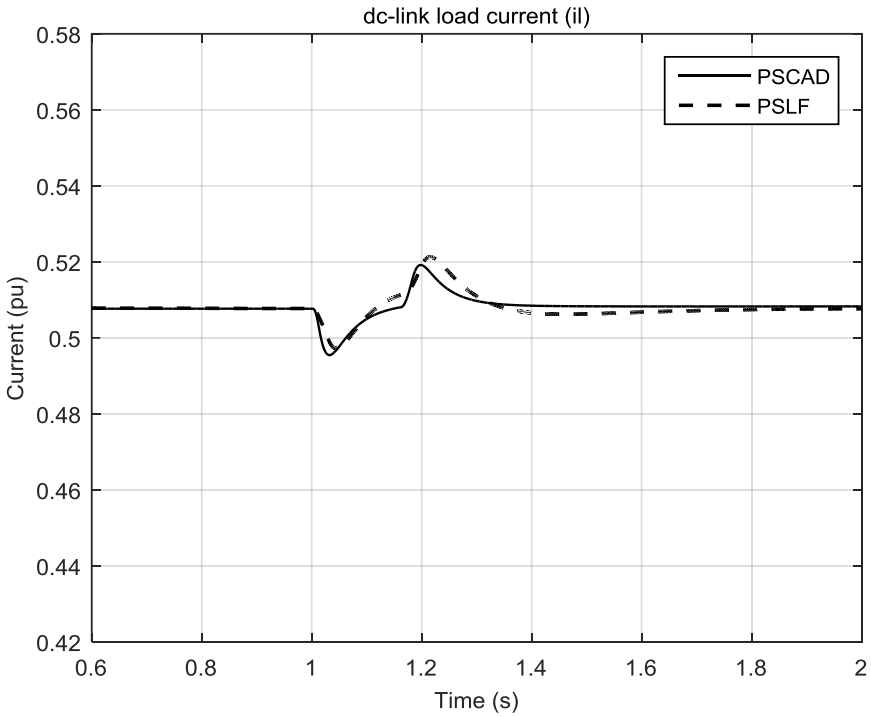

Figure 5.16 *dc*-Link Output Load Current

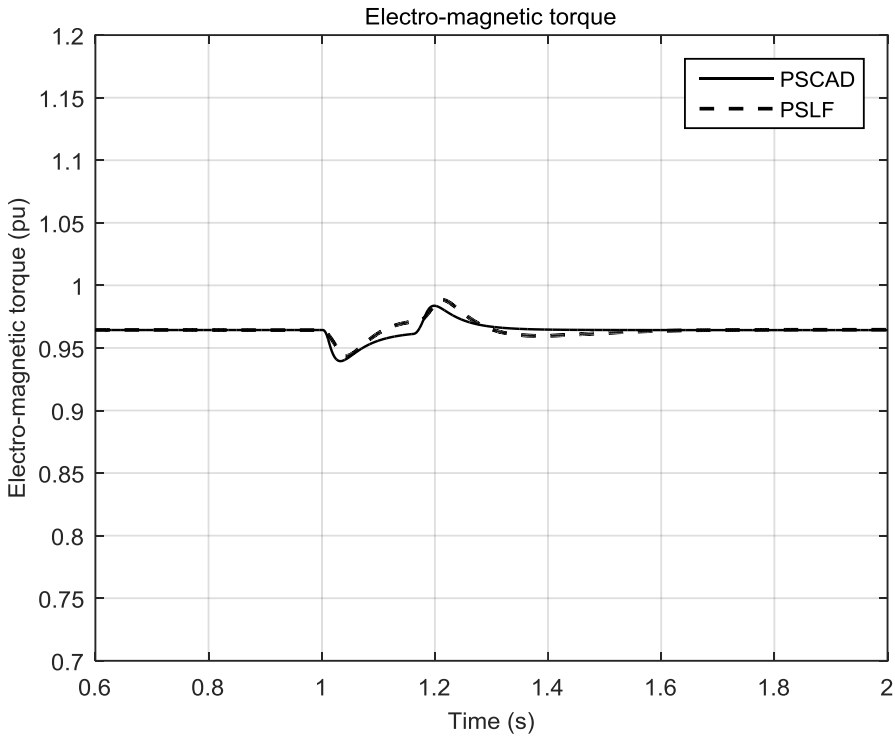

Figure 5.17 Electro-Magnetic Torque of the Induction Motor behind the Drive

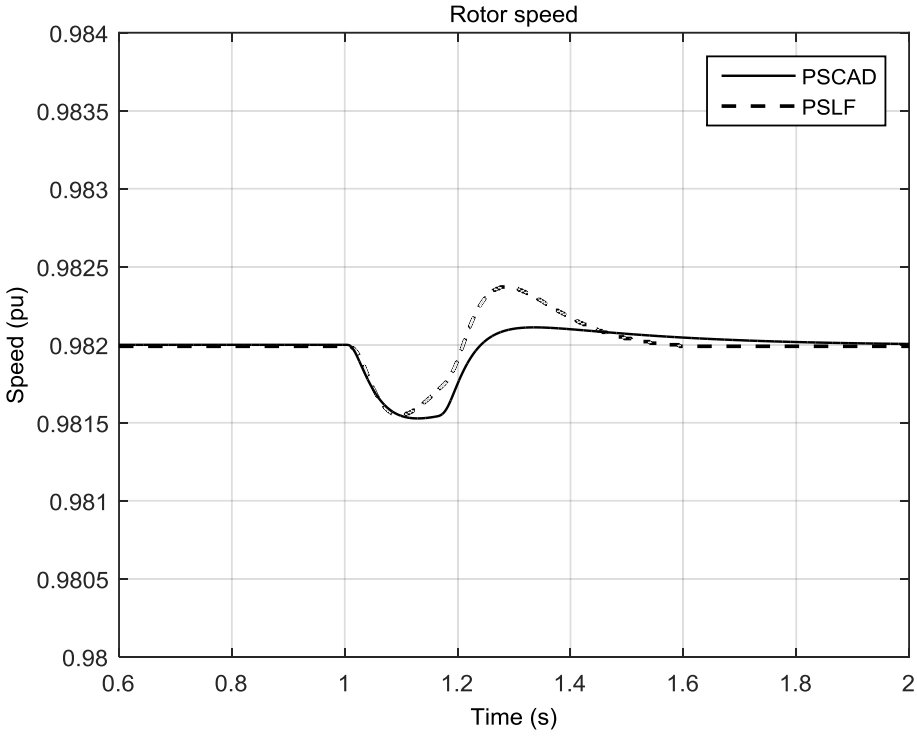

Figure 5.18 Rotor Speed of the Driven Induction Motor

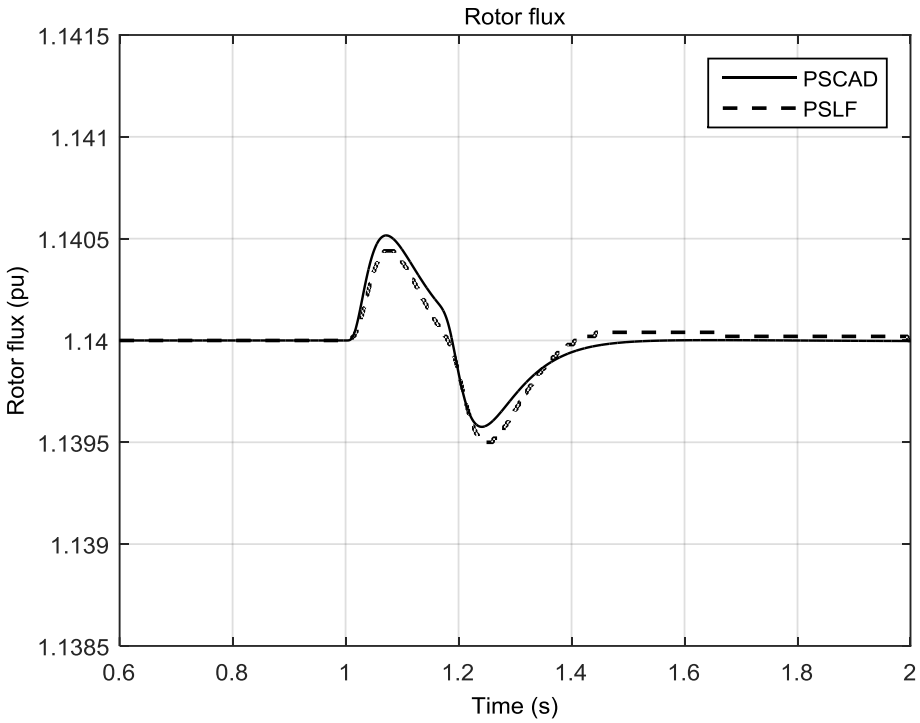

Figure 5.19 Rotor Flux of the Driven Induction Motor

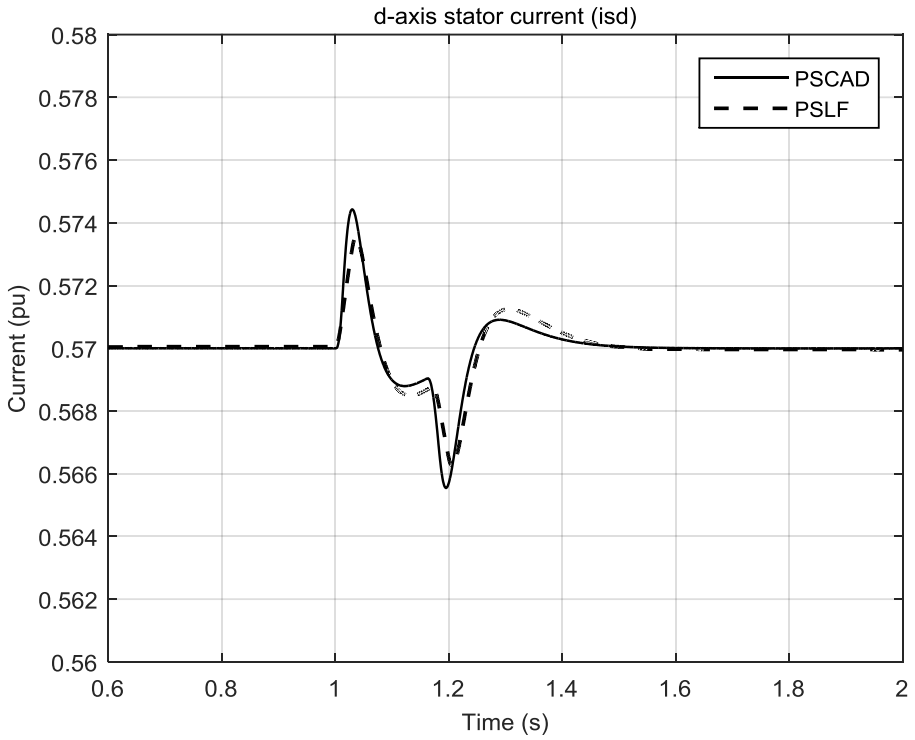

Figure 5.20 *d*-Axis Stator Current of the Driven Induction Motor

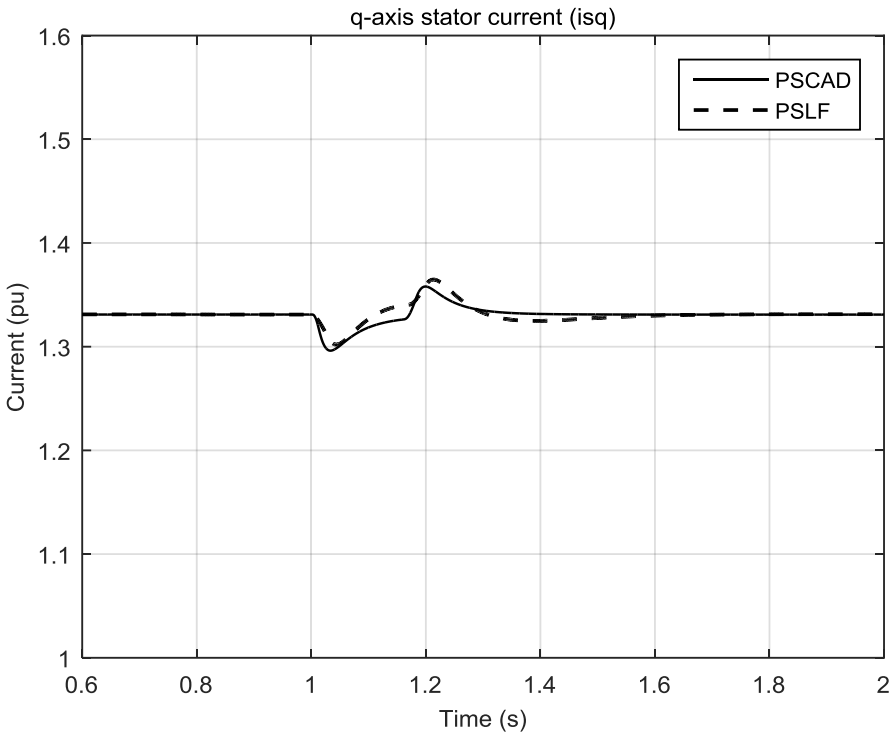

Figure 5.21 *q*-Axis Stator Current of the Driven Induction Motor

It is observed from the above plots that the PSLF simulation results are approximately identical to PSCAD simulation results within allowable errors. The cause of the errors is attributed to the simplification of the PSLF model. In the PSCAD simulation system, the internal single-cage induction motor model is used. In the PSLF simulation case, the induction motor model in rotor flux coordinates is implemented.

The voltages of the three generators and the terminal voltage of drive are shown in Figure 5.11 and Figure 5.12 separately for PSCAD and PSLF. The tiny mismatch existing in these two graphs is the consequence of network solution errors. The absorbed active power, shown in Figure 5.13, is depressed instantly and then boosted by controllers of the rectifier and inverter. Small amount of positive reactive power is withdrawn from the system during voltage sag to support the terminal voltage and is released when the voltage magnitude is restored after the fault, which is shown in Figure 5.14. The *dc*-link voltage

and *dc*-link output load current are shown in Figure 5.15 and Figure 5.16. It can be seen from both these plots that because of the rectifier *dc*-link voltage control and inverter *ac*-side currents control the *dc*-link voltage and load current are ideally regulated. The electro-magnetic torque and rotor speed of the driven motor are displayed in Figure 5.17 and Figure 5.18 respectively. It is noted from Figure 5.18 that the difference on the bumpy overshoot for the speed curve appears because of the cumulative integral effects of the mismatch on motor electro-magnetic and mechanical torques in these two simulators. It is recalled from previous sections that the mechanical load torque is proportional to the square of rotor speed.

5.7.2 Speed Adjustment

In this section, the comparison between the PSLF and PSCAD models is conducted considering a speed ramp-down process. A programmable reference speed adjuster configured for the machine-side inverter controller enforces a command to decelerate the driven motor from 100% to 80% rated speed. The parameters of the control and drive systems are provided in Table A.0.6. The speed of the driven motor, and the active and reactive power consumed at the drive terminal are plotted in Figure 5.22 to Figure 5.24.

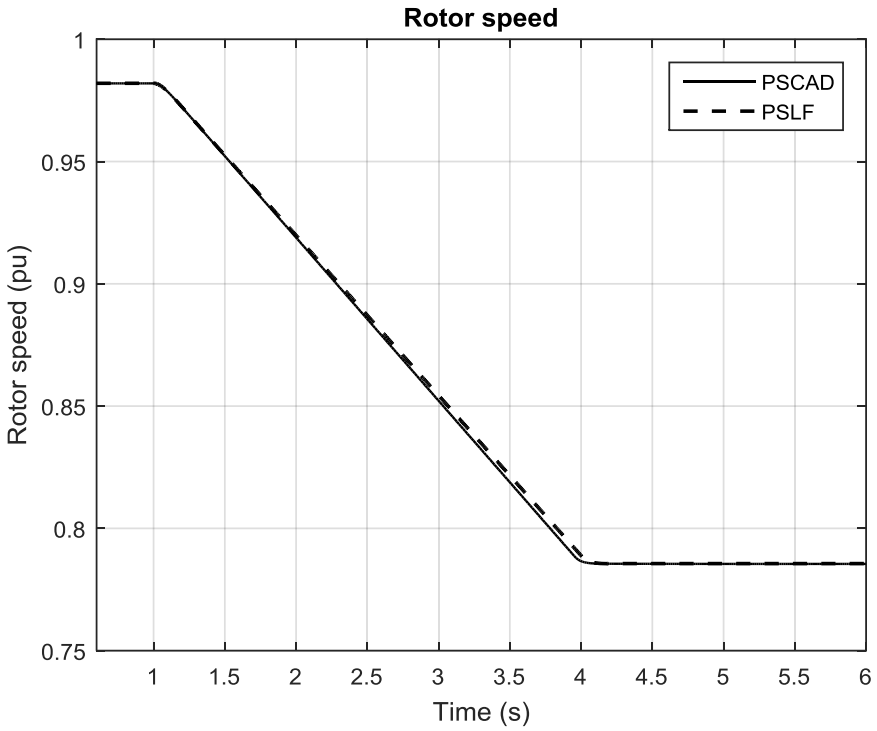

Figure 5.22 Rotor Speed (Speed Adjustment)

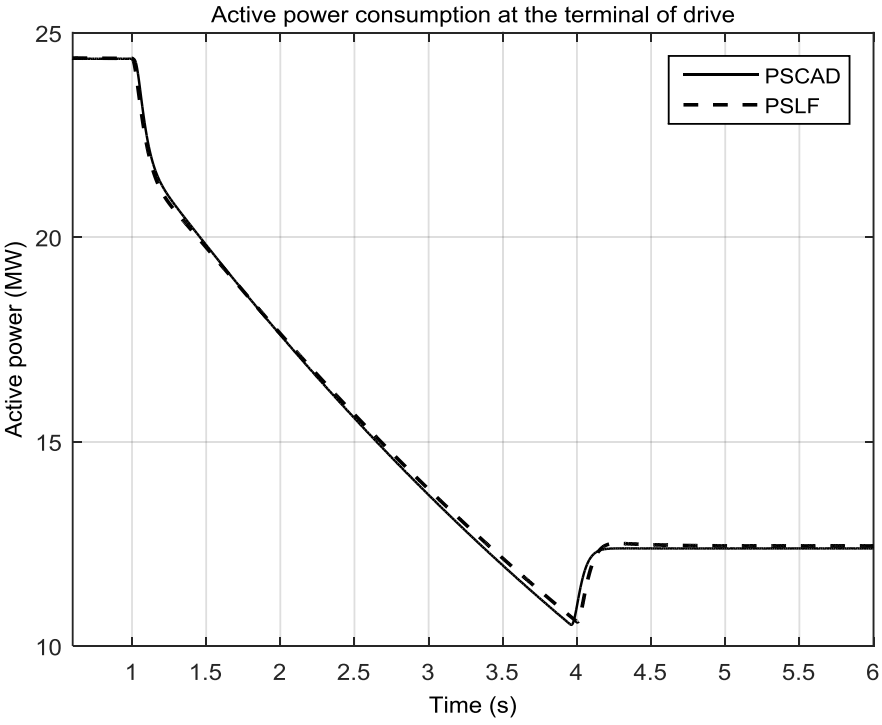

Figure 5.23 Active Power Consumption at the Terminal of the Drive

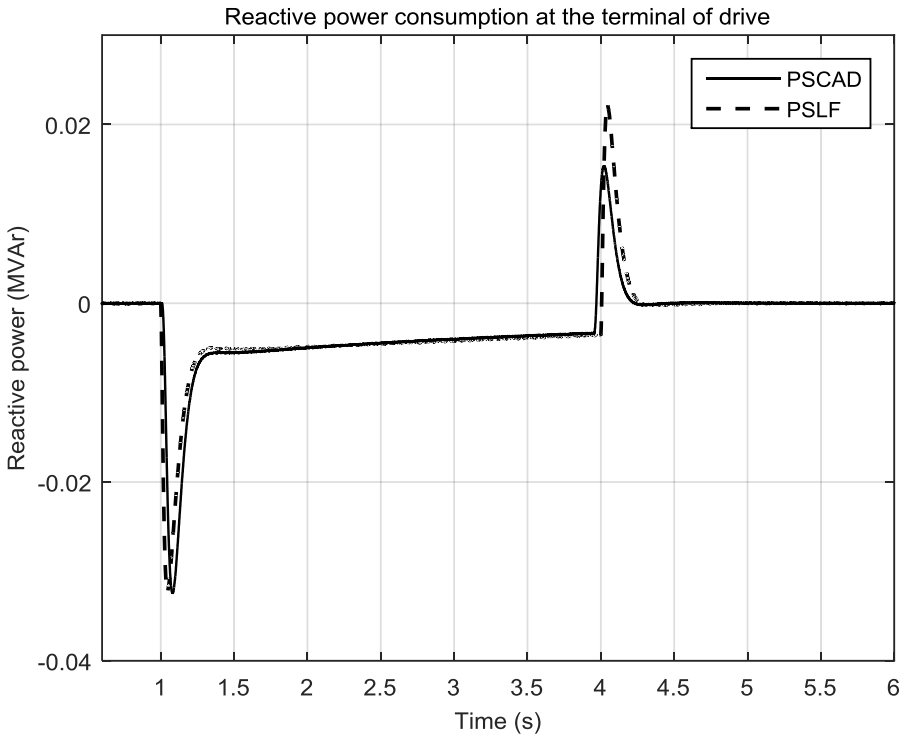

Figure 5.24 Reactive Power Consumption at the Terminal of the Drive

It is observed from Figure 5.22 and Figure 5.23 that the motors in both simulators decelerate smoothly, and the trajectories of motor speed and active power almost overlap. The small ramp-up slopes displayed on the active power curves in Figure 5.23 at the instant when motor speed reaches final values are caused by the delay of the rectifier *dc*-link voltage control with respect to the machine-side speed response. The reactive power consumption, as shown in Figure 5.24, is ideally regulated by the rectifier current control.

5.8 Simulation Scenario II: Investigating Mixed Loads Structure

In the second simulation scenario, a composite load structure including direct-connected and drive-supplied induction motors is formulated. This scenario leverages the PSLF transient drive model to investigate the benefits provided to the composite load structure by the drive load components subject to the voltage dip contingency occurring on

the supply side. In this simulation scenario, a small 4-bus simplified system with the described composite load structure is taken into account. The system schematic is shown in Figure 5.25.

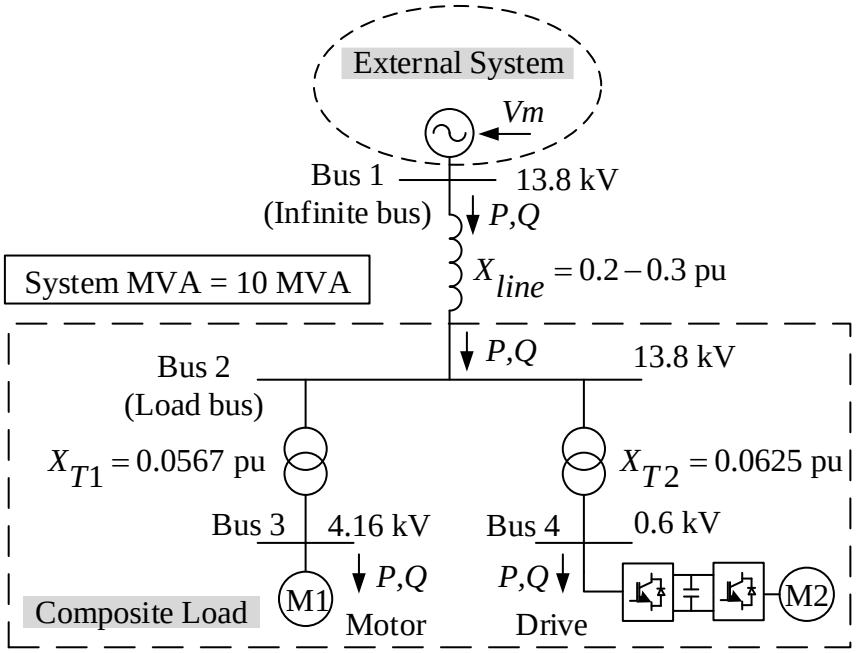

Figure 5.25 Mixed Induction Motor and Drive Loads

As shown in Figure 5.25, a magnitude-controllable voltage source is deployed at Bus 1, which is considered as the infinite bus. A heavily inductive equivalent distribution line stretches out to supply two aggregated industrial loads consisting of a direct-connected induction motor and a motor drive through two separate transformers. The voltage at the infinite bus is manipulated to dip from its nominal value to 40% and then recover to 90% of the original operating value.

The first case investigates the impacts on the system transient stability considering different percentages of drive load in the composite load structure.

In the second case, a blueprint for a future industrial load composition, in which over 90% motor loads are driven by advanced power electronic converters and only a very

small portion of induction motors are directly interfaced to the grid. The VAr support capability of the drives will be investigated in response to a voltage depression. The detailed simulation description for this scenario is provided in Table 5.2. The PSLF Motor1 model is used to represent the direct-connected motor load. The parameters of the motor and drive systems are given in Table A.0.7.

Table 5.2 Simulation Description of Scenario II

Contingency: *infinite bus voltage magnitude drops from nominal to 40% in 0.03 seconds, remains at 40% for 0.14 seconds, and recovers from 40% to 90% in 0.03 seconds.*	
Case 1: studying impacts of drive load with different levels of penetration 3 MW composite load, $X_{line} = 0.2\ pu$, No VAr support	
	2 MW motor + 1 MW drive
	1 MW motor + 2 MW drive
Case 2: investigating VAr support capability of drive load 0.1 MW motor + 2 MW drive, $X_{line} = 0.3\ pu$	
	No VAr support ($i_{feq}^{*} = 0.0\ pu$) during voltage dip
	Medium VAr support ($i_{feq}^{*} = 0.5\ pu$) during voltage dip
	Large VAr support ($i_{feq}^{*} = 1.0\ pu$) during voltage dip
Note: i_{feq}^{*} is the reference value for the reactive component current controller of the rectifier (see Figure 5.2 and Figure 5.8).	

In Case 2, different levels of VAr support are activated by changing the reference value of the reactive component of the line-side current (i_{feq}^{*}, see Figure 5.2 and Figure 5.8) when the drive terminal voltage drops below a threshold value.

5.8.1 Case 1: Different Levels of Penetration of Drive Load

In this case, a total 3.0 MW active power is considered consumed by the composite load depicted in Figure 5.25. This total load is allocated as a portion of the direct-connected induction motor and a portion of the motor drive as shown in Table 5.2. The simulation results are presented in Figure 5.26 through Figure 5.28.

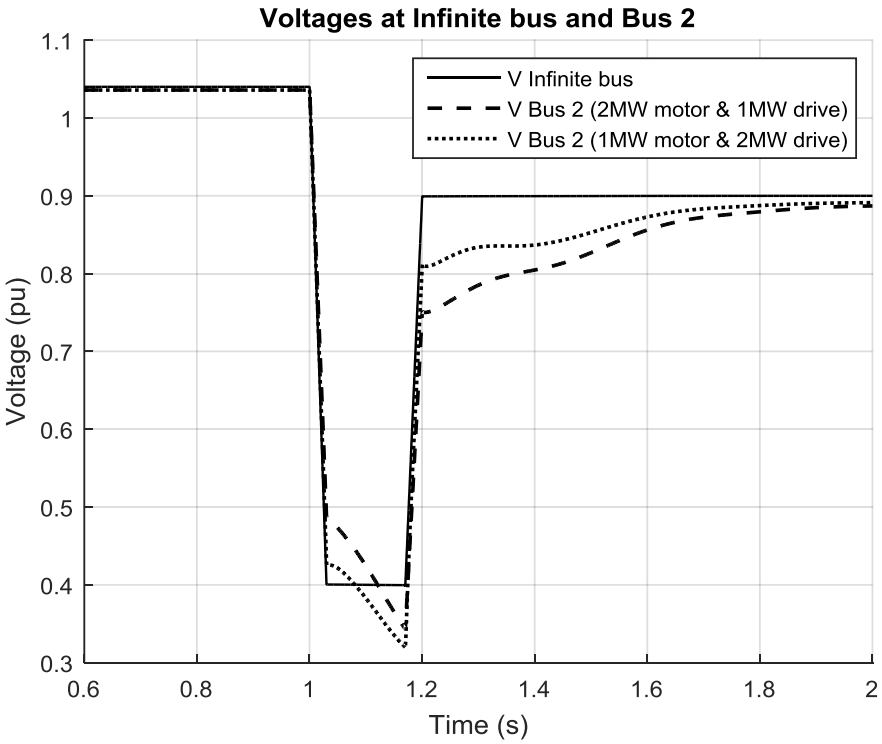

Figure 5.26 Voltages at Infinite Bus and Bus 2

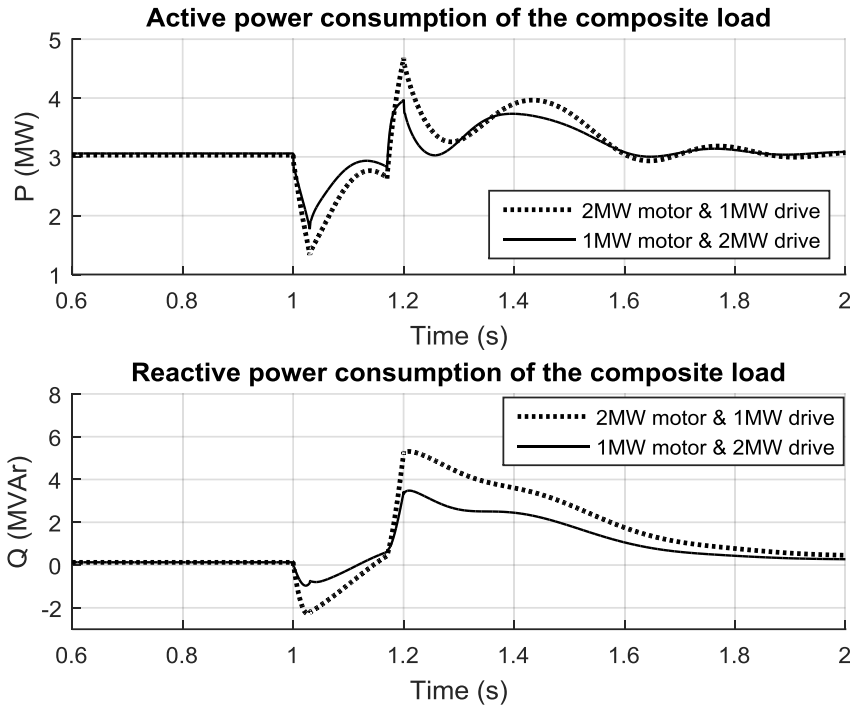

Figure 5.27 Active and Reactive Power Consumption of the Composite Load (Measured at Bus 2)

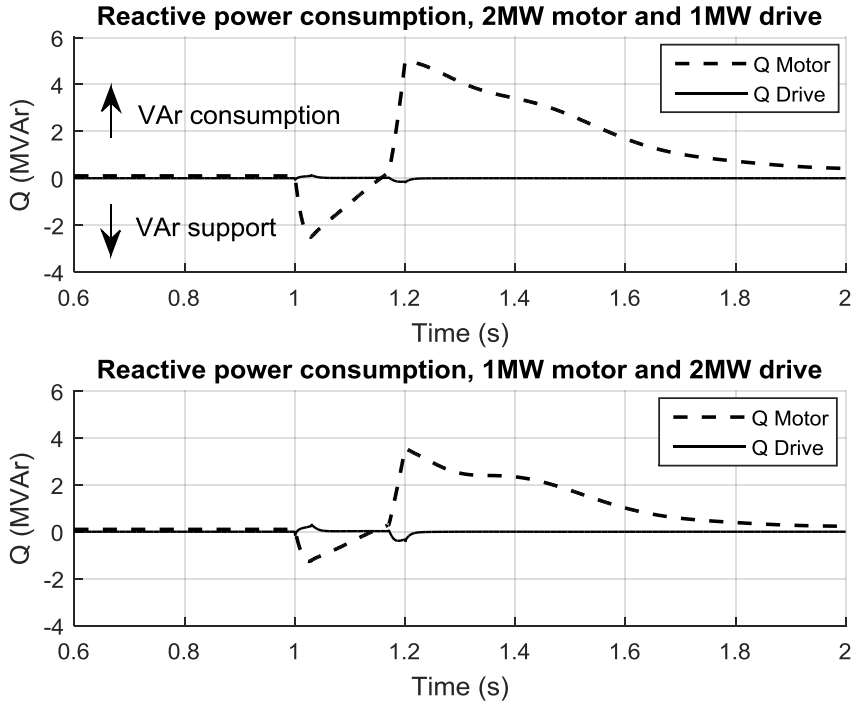

Figure 5.28 Reactive Power Consumption of the Motor and the Drive for Both Conditions

Figure 5.26 shows the voltages at the infinite bus and Bus 2. Figure 5.27 and Figure 5.28 depict the power consumptions measured at the terminals of the direct-connected motor load (Bus 3), drive load (Bus 4) and composite load (Bus 2). Negative VAr consumption indicates VAr support provided by the load as shown in Figure 5.28. This convention applies to the other reactive power traces throughout this chapter. It can be seen from Figure 5.27 that with higher percentage of drive load component, the active power trajectory of the composite load exhibits smaller variation during contingency and better post-event damping effects. It can be observed from Figure 5.26 and Figure 5.28 that the direct-connected motor provides transitory VAr support during voltage depression, and absorbs large amount of reactive power and delays the voltage recovery as the VAr contribution ends. In contrast, the reactive power consumption of the drive component is well regulated.

5.8.2 Case 2: VAr Support Capability of Drive Load

In the second simulation, the VAr support capability of the drive load is explored. The reference command for the reactive component of currents controllers (i_{feq}^*), as shown in Figure 5.2 and Figure 5.8, is strategically maneuvered to output reactive power to the system during voltage depression. In this case, the same system schematic as shown in Figure 5.25 is used. The motor load is much smaller in size compared to the drive load. The simulation details are provided in Table 5.2. In the table, "No VAr support" means the reference i_{feq}^* is zero throughout the simulation. "Medium VAr support" and "Large VAr support" indicate the conditions of a hard switch from $i_{feq}^* = 0.0\ pu$ to $i_{feq}^* = 0.5\ pu$ and $i_{feq}^* = 1.0\ pu$ when the terminal voltage drops below a set point that is set to be 0.8 pu in

this simulation case. The same contingency as Case 1 (shown in Table 5.2) is replicated in this case. Related results are plotted in Figure 5.29 through Figure 5.35.

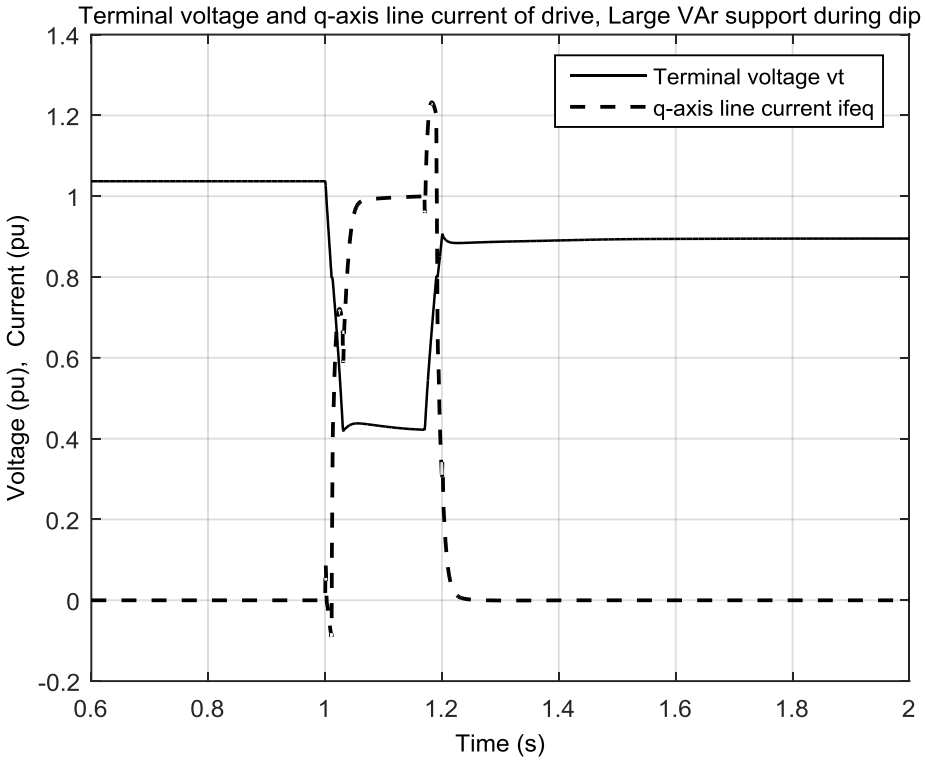

Figure 5.29 Terminal Voltage of the Drive and the *q*-Axis Line-Side Current i_{feq} with Large VAr Support during Voltage Depression

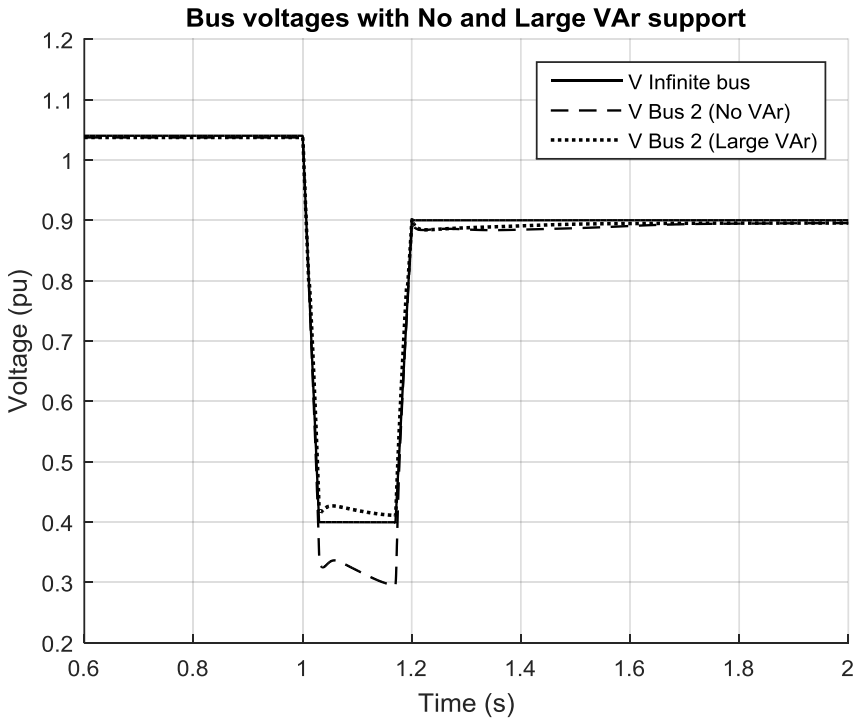

Figure 5.30 Voltages at Infinite Bus and at Bus 2 for Conditions of No VAr Support and Large VAr Support

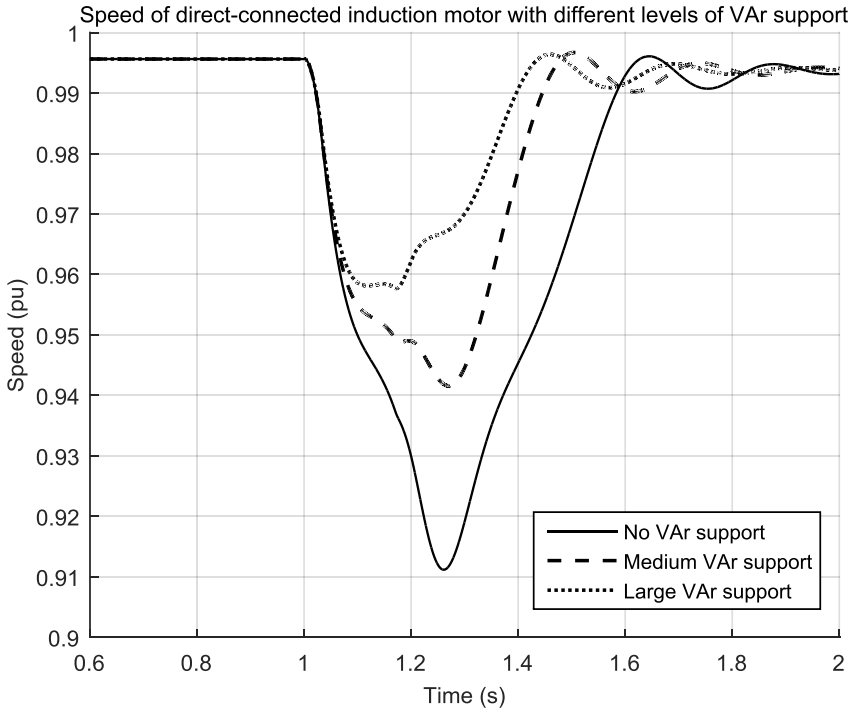

Figure 5.31 Speeds of Direct-Connected Induction Motor with Different Levels of VAr Support by the Drive

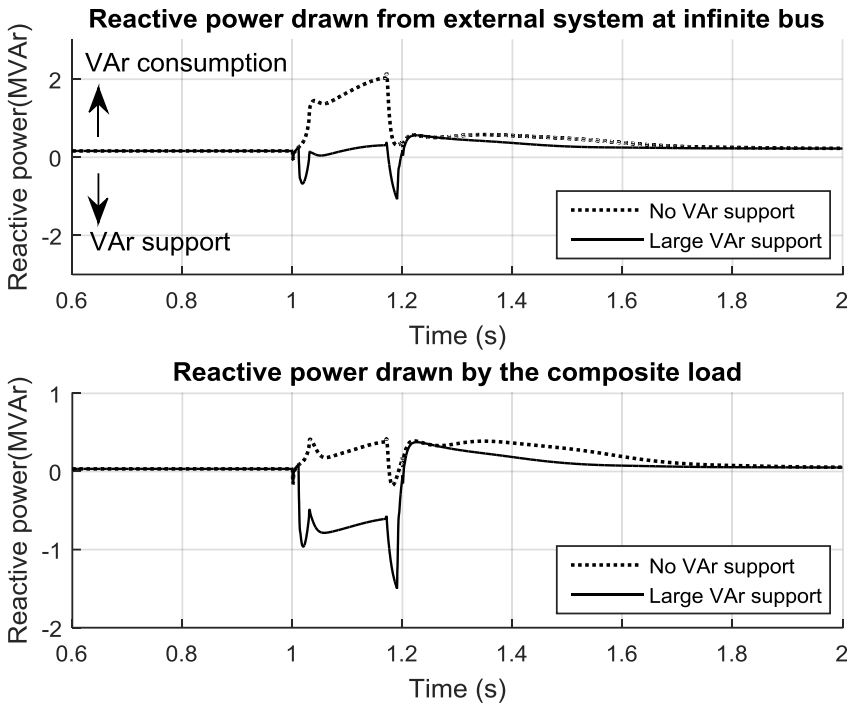

Figure 5.32 Reactive Power Drawn by the Infinite Bus and by the Composite Load for Conditions of No VAr Support and Large VAr Support

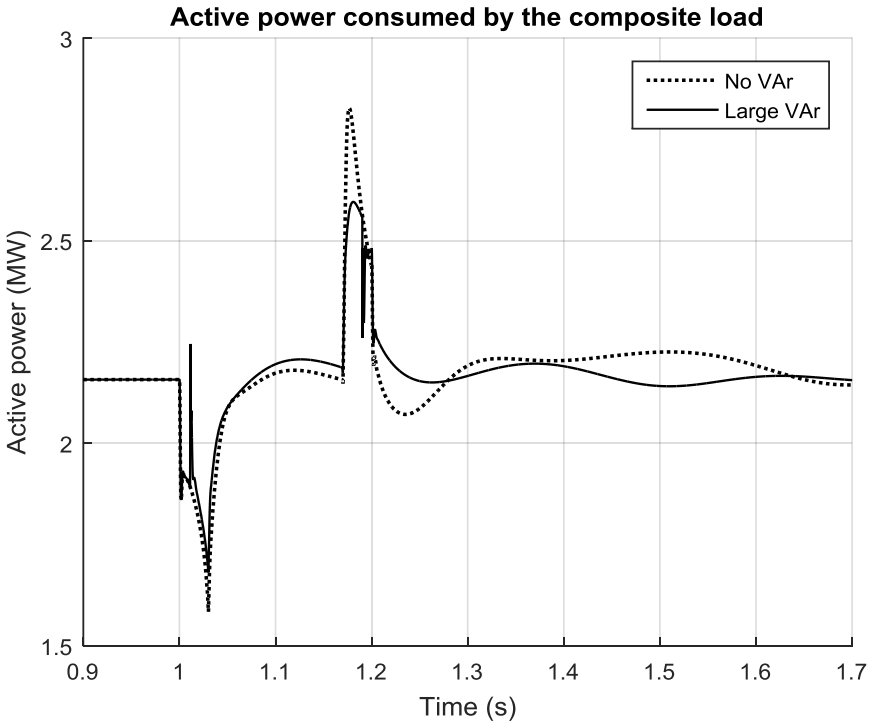

Figure 5.33 Active Power Consumed by the Composite Load for Conditions of No VAr Support and Large VAr Support

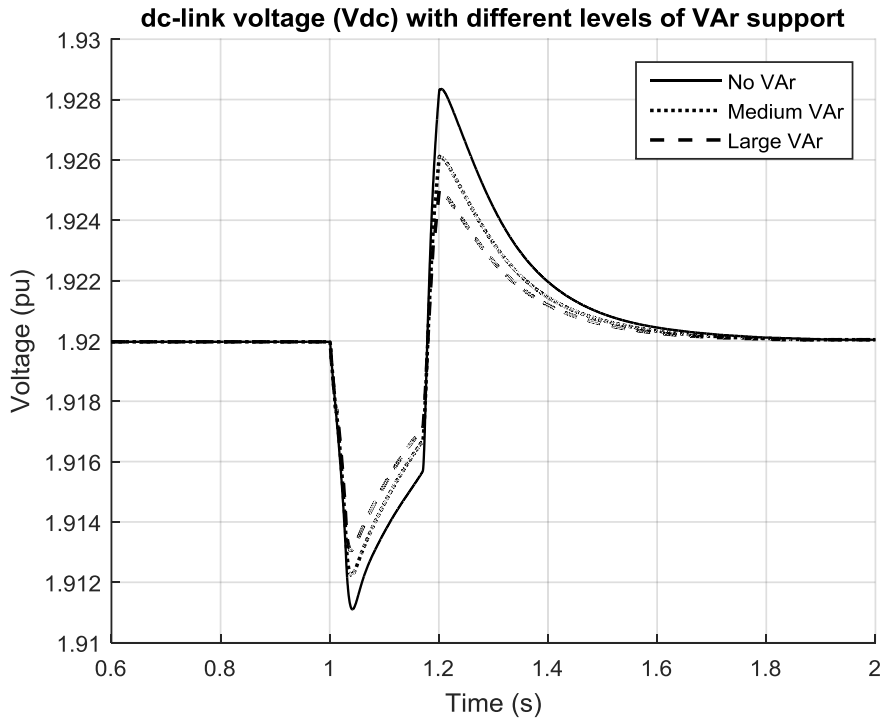

Figure 5.34 *dc*-Link Voltages for Different Levels of VAr Support

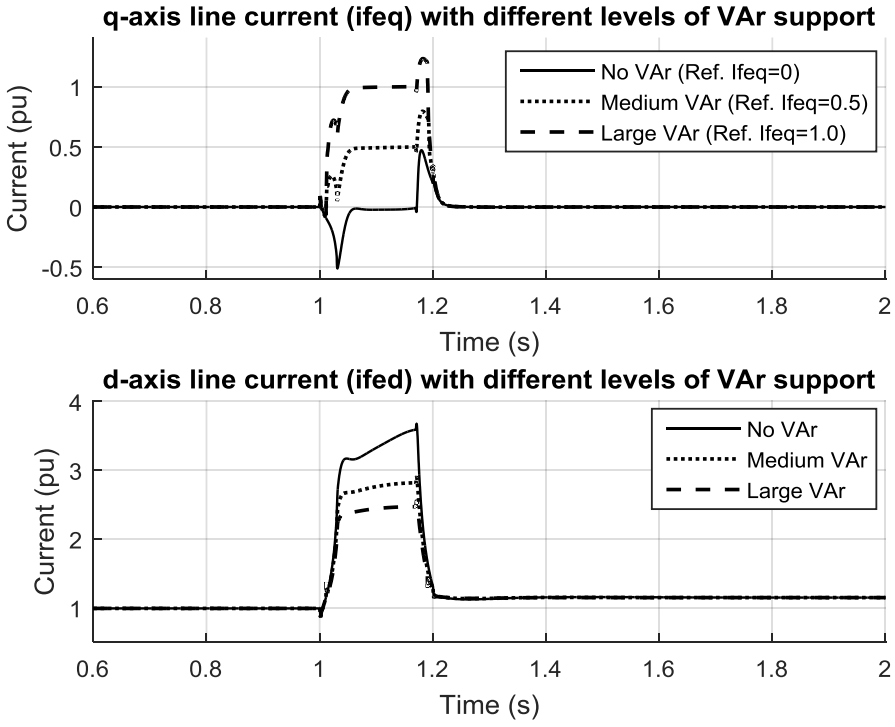

Figure 5.35 *q*-Axis and *d*-Axis Grid-Side Line Currents (i_{feq} and i_{fed}) for Different Levels of VAr Support

Figure 5.29 displays the terminal voltage of the drive and the reactive component of the line-side current (i_{feq}) both in per unit under the condition of large VAr support. It is viewed that i_{feq} is regulated to be zero during normal operation and boosted to 1.0 after voltage drops below 0.8 pu. The small overshoot in i_{feq} during voltage recovery is caused by control effects in response to the voltage recovery and the reference command change. The plot of i_{feq} validates the functioning of the current controllers.

Figure 5.30 presents the voltages at the infinite bus and the composite load bus (Bus 2) under the conditions of zero and large VAr support. The solid line denotes the voltage at the infinite bus. It is observed that with large VAr support the voltage at the terminal of the composite load is higher than the infinite bus voltage during the contingency; while in the case without any VAr support the voltage of the composite load is below the infinite bus and is as low as 0.3 pu. The activated VAr support provided by the drive load could increase the localized voltage by approximately 0.1 pu during voltage depression.

Figure 5.31 depicts the speeds of the direct-connected motor load at Bus 3 at different levels of VAr support by the drive. It can be seen that with better voltage support the motor decelerates to a relatively higher speed compared to the case with no VAr injection.

Figure 5.32 displays the reactive power consumptions at the infinite bus and Bus 2. It is shown that without VAr support the infinite bus draws reactive power from the external system, and most of the absorbed reactive power is consumed by the equivalent inductive distribution line as a consequence of the voltage dip. Considering that the drive load contributes VAr support during voltage dip, a large portion of the generated reactive power

traverses the inductive line and compensates the reactive power consumption at the infinite bus. A small fraction of the reactive power circulates to the direct-connected motor load to satisfy its demand. It is observed from the upper subplot of Figure 5.32 that the total reactive power consumption at the infinite bus is largely reduced during the voltage dip contingency.

Figure 5.33 displays the active power consumption at the composite load bus. It can be seen that the fluctuation of the active power during and after the voltage depression becomes smaller with the VAr support being activated.

Figure 5.34 depicts the *dc*-link voltage of the drive converter under different levels of VAr support. Due to the action of the *dc*-link voltage controller, the *dc*-link voltage trajectories are approaching each other. The *dc*-link voltage experiences a sag during *ac*-side voltage depression, and then recovers to the reference value after the overshoot is completely damped by the controllers.

Figure 5.35 exhibits the *d*-*q* axes line-side currents of the converter. It can be seen from the upper subplot of Figure 5.35 that the reactive components of the line-side currents (i_{feq}) are regulated at designated values by current controllers during the voltage depression. It has been stated above that the sag levels of the *dc*-link voltages are nearly consistent under these three conditions. The *d*-axis current controller, which obtains the reference signal from the output of the *dc*-link voltage controller as shown in Figure 5.2, effectively lowers the peak value of the *d*-axis line-side current i_{fed} to avoid overcharging the *dc*-link capacitor as the *q*-axis current rises during contingency. This action also minimizes the overcurrent problem on the *ac*-side line.

5.8.3 Installation of Terminal Voltage Regulator

As a supplement to Case 2 (Section 5.8.2), a terminal voltage regulator is installed for the rectifier control of the drive as an alternative way to provide VAr support. A PI controller is employed to autonomously adjust the amount of reactive power support based on the error of the reference and actual terminal voltages. This type of VAr support mechanism is capable of constantly supplying reactive power to force the actual terminal voltage to approach the reference value no matter whether the terminal voltage experiences small disturbances or sudden large dips. It is observed that the switching type of VAr support as shown in Case 2 can only be activated when the terminal voltage drops below a threshold value. The superiority of the controller-based mechanism to the switching mechanism is that the controller-based VAr support is not only effective during voltage dip contingency but also beneficial in improving the terminal voltage condition during normal operation. After the installation of the terminal voltage regulator, the line-side rectifier control as shown in Figure 5.8 is modified to be drawn in Figure 5.36.

The controller-based VAr support is compared to the switching-based VAr support under the same load condition and system connection as Case 2. For the controller-based VAr support shown in Figure 5.36, the proportional gain of the voltage regulator K_{p_vt} is chosen to be 3.0 pu, and the integral gain K_{i_vt} is 0.01 pu/s. The limiter for i_{feq}^{*} is set to be $i_{feq\_min}^{*} = -1.0\ pu$ and $i_{feq\_max}^{*} = 1.0\ pu$. For the switching-based VAr support, only the condition of large VAr support is compared. The results are provided in Figure 5.37 through Figure 5.39.

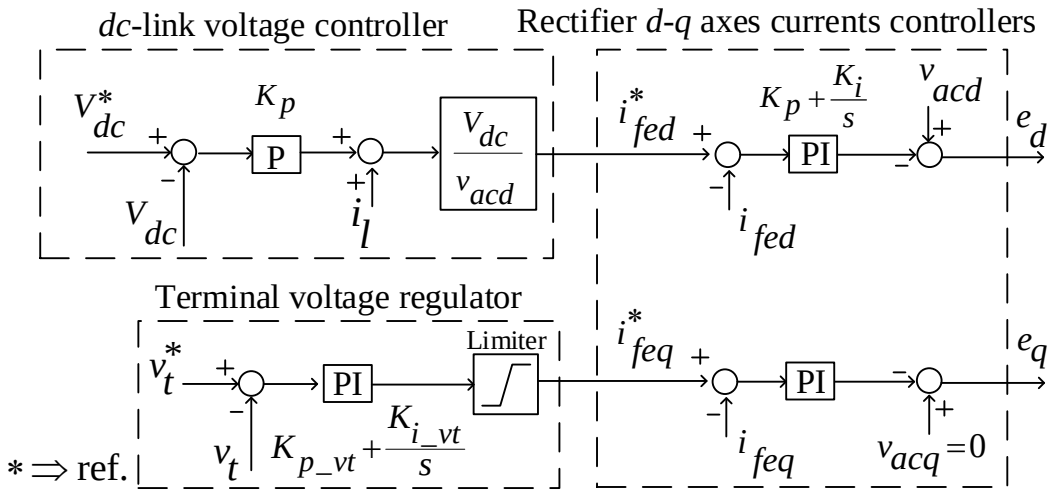

Figure 5.36 Line-Side Rectifier Control with Terminal Voltage Regulator

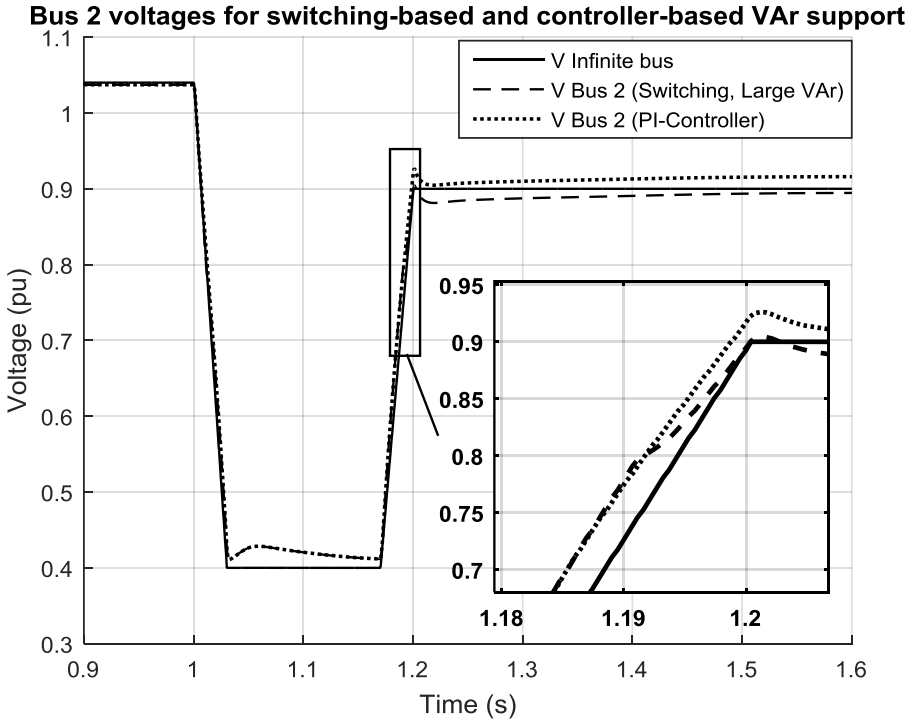

Figure 5.37 Voltages at Infinite Bus and Bus 2 for Switching-Based and Controller-Based VAr Support Mechanisms

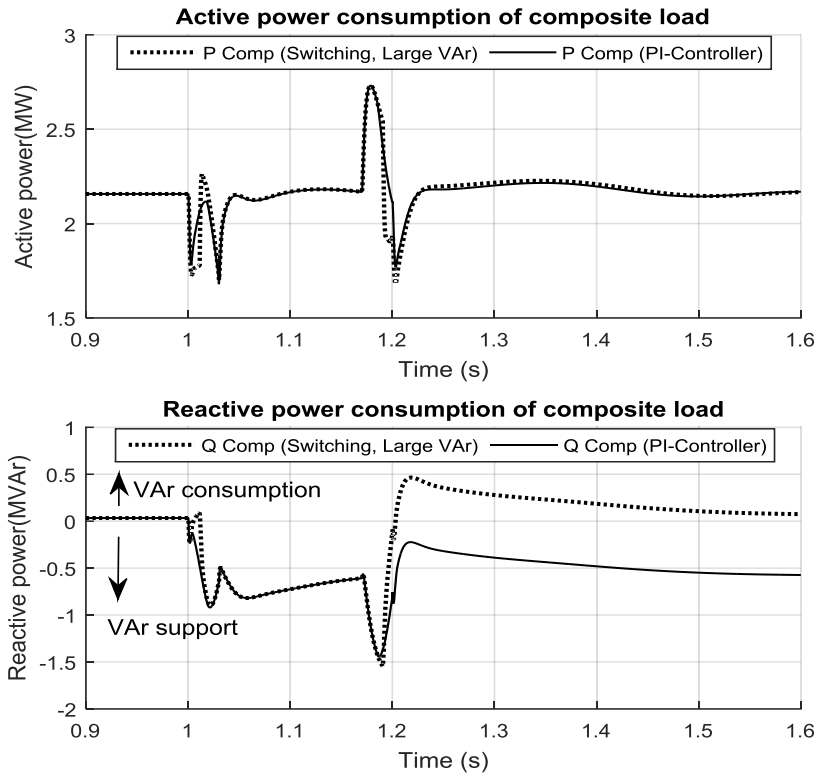

Figure 5.38 Active and Reactive Power Consumptions of the Composite Load for Switching-Based and Controller-Based VAr Support Mechanisms

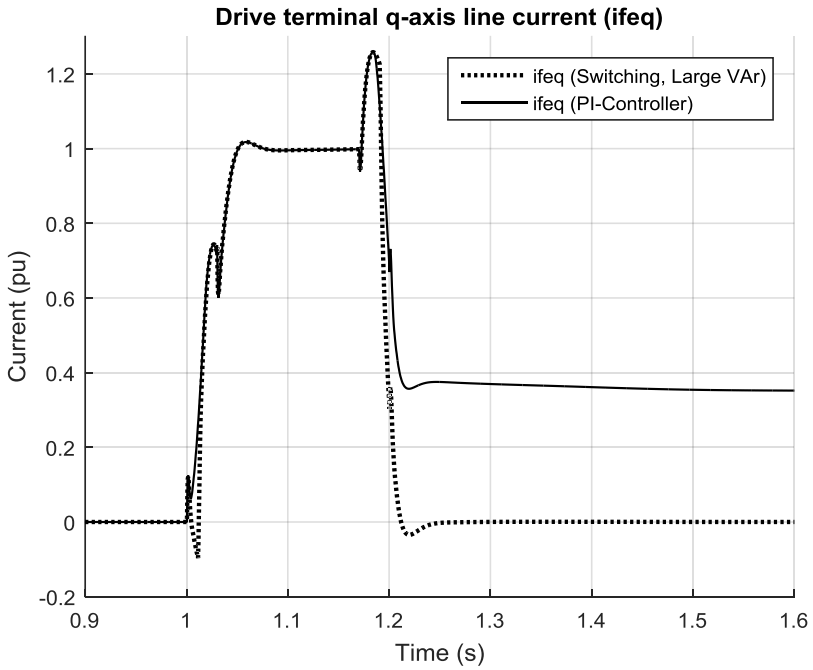

Figure 5.39 Drive Terminal q-Axis Line Current i_{feq} for Switching-Based and Controller-Based VAr Support Mechanisms

Figure 5.37 depicts terminal voltage of the composite load at Bus 2 compared to supply voltage at the infinite bus. It is seen that both VAr support mechanisms boost the load voltage to be higher than the infinite bus voltage during voltage depression. After the depression is cleared, the supply voltage recovers to 0.9 pu which is higher than the threshold voltage (0.8 pu) of the switching-mode VAr support. The VAr support of the switching mode is discontinued after the voltage recovery. Therefore, the terminal voltage of the composite load stays below the supply voltage. Nevertheless, for the controller-based VAr support, since the recovered voltage is still lower than the preset nominal voltage of the terminal voltage regulator, the drive continues to output reactive power and raise the load voltage to a level higher than the supply voltage.

Figure 5.38 displays the active and reactive power consumptions of the composite load. It can be observed from the lower subplot of Figure 5.38 that if the drive is equipped with terminal voltage regulator, the composite load keeps injecting VArs into the system as long as the terminal voltage is below the nominal value.

Figure 5.39 shows the reactive component of the drive terminal current. It can be seen that the controller-based VAr support responds to the voltage depression a little faster than the switching-based method.

In general, the simulation results in Scenario II affirm the prediction that the drive load is capable of providing beneficial influence to the neighboring motor loads and to the external system.

5.9 Simulation Scenario III: Test of Multiple Mixed Loads

The simulations in Sections 5.7 and 5.8 only consider one drive model in the system. In this section, the test of multiple mixed load blocks is performed on IEEE 14-bus system

[4] shown by Figure 5.40. The original static loads located at Buses 11, 12, 13 and 14 are replaced by the mixed load blocks that consist of different percentages of drive and motor components. The other static loads in the system are modeled as constant impedance loads. Bus 1 generator is equivalenced as an infinite voltage source for which different voltage contingencies can be played in to represent the behaviors of external faults. In the simulation, the infinite source voltage depresses from 1.06 pu to 0.7 pu, and recovers to 1.02 pu after 12 cycles. Two combinations, 80% drive load plus 20% motor load and 80% motor load plus 20% drive load, are assigned to form the loading conditions of each mixed load block. These two combinations of loading are compared. Unity power factor is assumed for the motor and drive loads. The terminal voltage regulator as discussed in Section 5.8.3 is installed for all the drives in the system. The parameters of the motor and drive loads are provided in Table A.0.8.

This PSLF simulation scenario investigates the system transient stability improved by increasing penetration and dispersion of advanced motor drive systems. The simulation results are presented in Figure 5.41 through Figure 5.43.

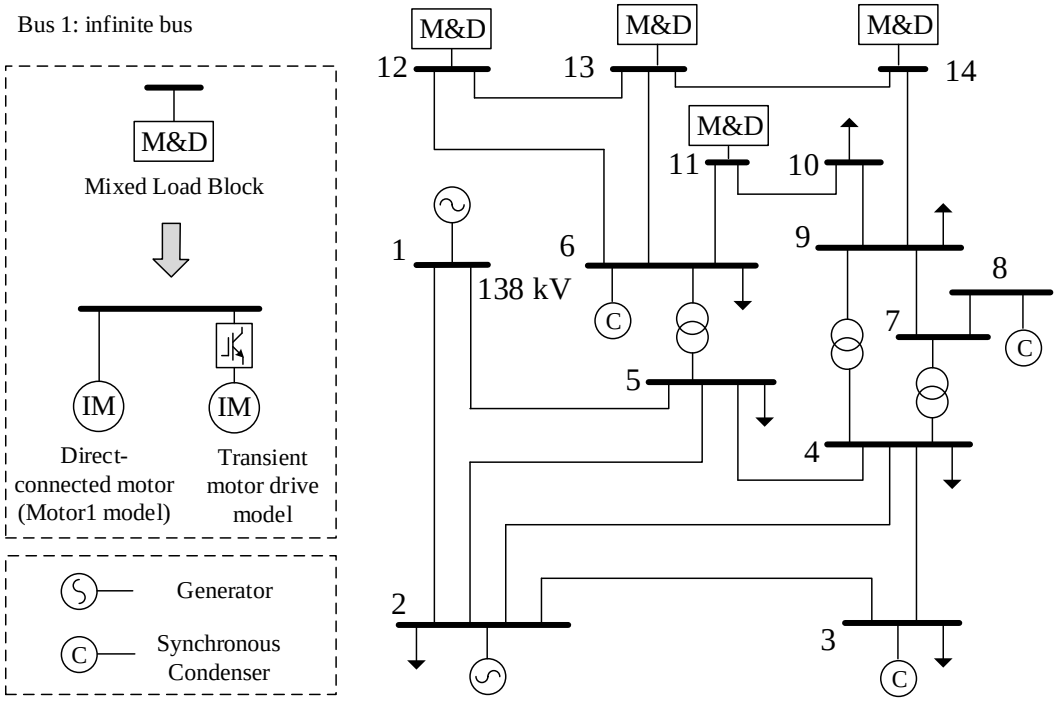

Figure 5.40 IEEE 14 Bus System with Several Static Loads Replaced by Mixed Load Blocks

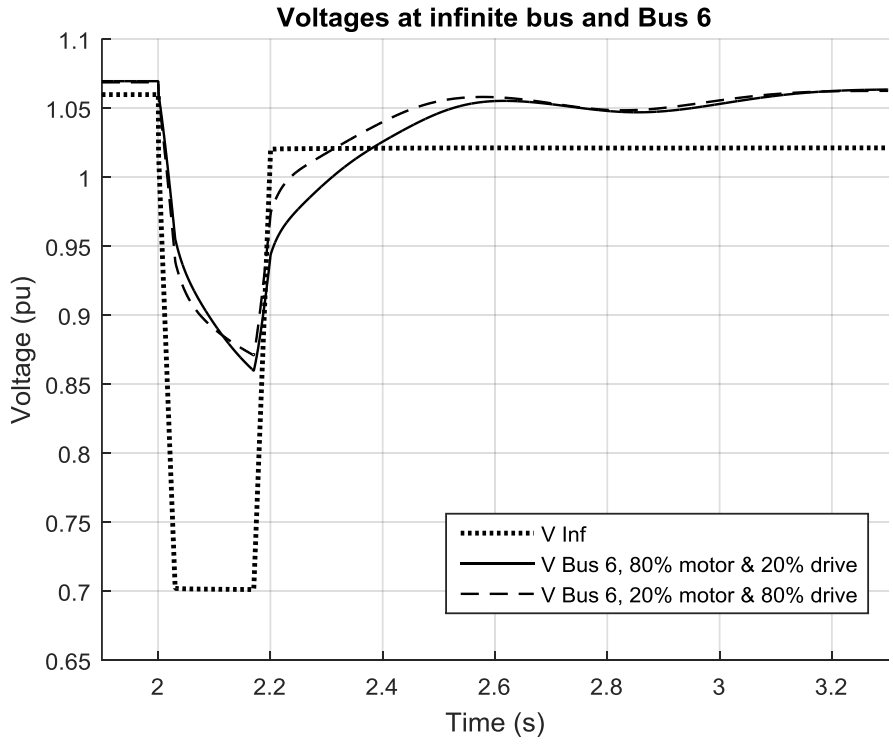

Figure 5.41 Voltages at Infinite Bus and Bus 6

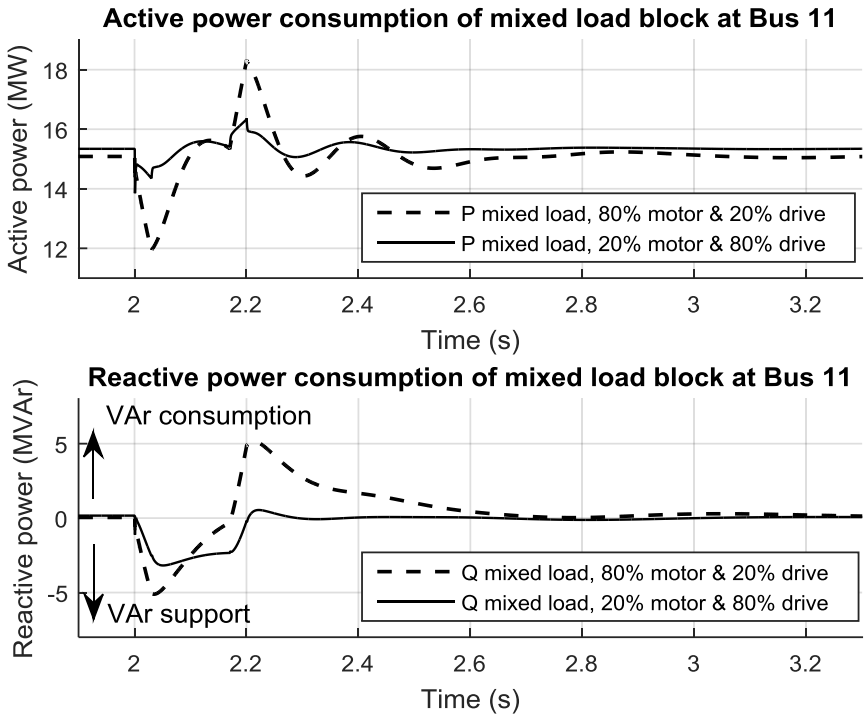

Figure 5.42 Active and Reactive Power Consumptions of Mixed Load Block at Bus 11

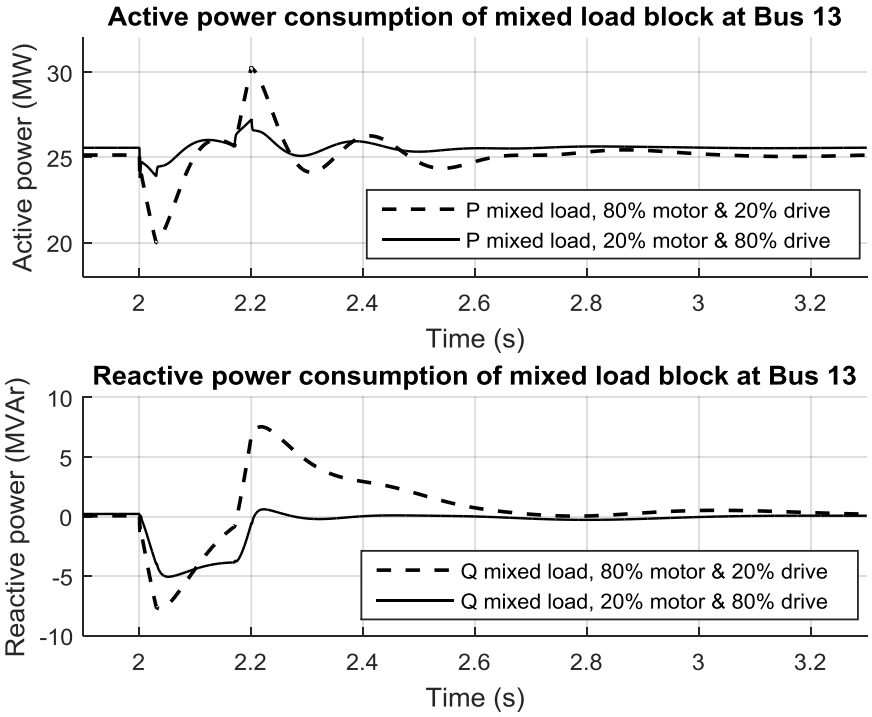

Figure 5.43 Active and Reactive Power Consumptions of Mixed Load Block at Bus 13

Figure 5.41 compares Bus 6 voltage during and after the depression contingency for the two combinations of loading. It is discovered that with higher percentage (80%) of drives in the multiple mixed load blocks, the post-event system voltages recover faster than the condition of higher percentage of motors. Similar conclusions were drawn from the simulation of single unit of composite load model in Section 5.8.1.

Figure 5.42 and Figure 5.43 depict the active and reactive power consumptions of the mixed load blocks at Buses 11 and 13. Both figures demonstrate stable active power consumptions for the condition of 80% drive and oscillatory active power characteristics for the condition of 80% motor during and after the voltage depression. Under both conditions, the mixed load blocks output some reactive power to support the depressed voltage. After the clearance of the fault, the mixed load blocks with 80% motor consume large amount of reactive power; while for the condition of 80% drive the reactive power consumptions of the mixed load blocks are negligible.

The simulation in this scenario verifies the availability of system-level simulation with multiple units of the developed transient drive model. The load characteristics are observed to be more stable and beneficial with higher rate of advanced drive components in the load.

Chapter 6. CONCLUSIONS AND FUTURE WORK

The major contribution of this research is the development of a performance-based drive load model and a complete transient drive load model based on vector control technology for electro-magnetic transients and positive sequence transient stability simulations. The dissertation report can be divided into three major parts. The first part details the construction of the three-phase vector-controlled drive system on the EMT-level simulation program. The second part of this dissertation proposes a performance-based drive model that can be used to analyze the responses of drive loads to system small disturbances (e.g. low-frequency oscillation, generation step change, and line outage). The performance-based drive model is derived based on obtaining the linearized transfer functions relating power-voltage and power-frequency at the supply point of the drive. The third part of this report covers the implementation of the complete transient drive model in the PSTS simulator. The complete drive model is conceived based on the consideration of devising a linkage between the inverter-side motor control system and the rectifier-side power control system.

It can be concluded from the model development and simulations that the advanced motor drive model with vector controls demonstrates superior performance in controlling the power consumption of the load, stabilizing the motor terminal voltages and currents, and adjusting the motor speed smoothly. These favorable performance characteristics tremendously improve the efficiency of motor operation in an industrial application.

The developed performance-based drive model facilitates the investigation of system small-signal stability considering increasing penetration of the motor drive loads. With such levels of the drive load model being represented in the system-level simulations,

the introduced damping effects on the oscillations of bus voltages, bus frequencies and line power flows can be simulated and clearly observed. The simulation results demonstrate that, as the penetration of the drive loads increases, the damping effects improve. It can also be concluded that the outage of a stressed transmission line aggravates system oscillations.

The development of the complete transient drive model in PSTS programs facilitates the investigation of the improvement of the system transient stability introduced by the drive loads. It can be concluded that the increasing penetration of the motor drive loads renders more resiliency and stability to the characteristics of load powers during and after the voltage depression. Considering the incorporation of the developed complete drive loads into a future composite load structure, the intelligent VAr support characteristics of the drive loads can be explored. It is observed from the simulation results that the VAr support provided by the drive loads has extensive advantages in boosting the depressed localized voltage magnitude, compensating reactive power inflow into the composite load, preventing the neighboring motor loads from under-speed or stalling, and stabilizing the active power fluctuations of the drive itself and the neighboring motors.

Comparing the performance-based and the complete transient drive models, it can be generalized that the performance-based model is a realistic representation of the detailed drive model in the linearized operating range and is exclusively utilized to analyze the system behavior under small perturbations. If large disturbances are considered in the dynamic simulations, the complete drive model is a preferable choice though the complexity of the drive model is simplified.

In the future, the performance-based composite load model can be developed using similar modulation techniques as discussed in this dissertation. The traditional composite load model includes static loads, voltage-dependent electronic loads, direct-connected three phase induction motor loads and balanced-distributed single-phase motor loads. The cutting-edge load structure, however powered by electronic converters, would incorporate large portions of converter-driven three-phase and single-phase induction motor loads. The single-phase motor drive is easy to implement in the EMT simulator but hard to represent in the PSTS simulation program. The performance-based modeling is suitable to capture the dynamics of such a complicated load structure without needing to handle the internal details of the single-phase drives. Besides, the frequency and voltage damping factors can be added to the performance-based model for further investigation.

The positive-sequence transient drive model developed in this dissertation is based on sophisticated vector control techniques. In the future, simple scalar-controlled drives can also be implemented in the PSTS programs using similar approaches.

REFERENCES

[1] B. R. Williams, W. R. Schmus and D. C. Dawson, "Transmission voltage recovery delayed by stalled air-conditioner compressors," *IEEE Transactions on Power Systems*, vol. 7, no. 3, pp. 1173 - 1181, 1992.

[2] J. W. Shaffer, "Air-conditioner response to transmission faults," *IEEE Transactions on Power Systems*, vol. 12, no. 2, pp. 614 - 621, 1997.

[3] Y. Liu, V. Vittal, J. Undrill, and J. H. Eto, "Transient model of air-conditioner compressor single phase induction motor," *IEEE Transactions on Power Systems*, vol. 28, no. 4, pp. 4528 - 4536, Nov. 2013.

[4] P. Kundur, *Power system stability and control*, McGraw-Hill, NY, 1994.

[5] K. Prasertwong, N. Mithulananthan, and D. Thakur, "Understanding of low-frequency oscillation in power systems," *International Journal of Electrical Engineering Education*, vol. 47, no. 3, Jul. 2010.

[6] I. A. Hiskens and J. V. Milanovic, "Load modeling in studies of power system damping," *IEEE Transactions on Power Systems*, vol. 10, no. 4, pp. 1781 - 1786, Nov. 1995.

[7] IEEE Task Force on Load Representation for Dynamic Performance, "Load representation for dynamic performance analysis," *IEEE Transactions on Power Systems*, vol.8, no. 2, pp. 472 - 482, May 1993.

[8] IEEE Task Force on Load Representation for Dynamic Performance, "Standard load models for power flow and dynamic performance simulation," *IEEE Transactions on Power Systems*, vol.10, no. 3, pp. 1302 - 1313, Aug. 1995.

[9] "WECC composite load model," WECC Load Modeling Task Force, [Online]. Available: https://www.wecc.biz/Reliability/WECC%20MVWG%20Load%20Model%20Report%20ver%201%200.pdf.

[10] "PSLF User's Manual," ver. 18.1, General Electric, Apr. 2012.

[11] L. Pereira, D. Kosterev, P. Mackin, D. Davies, J. Undrill, and W. Zhu, "An interim dynamic induction motor model for stability studies in the WSCC," *IEEE Transactions on Power Systems*, vol.17, no. 4, pp. 1108 - 1115, Nov. 2002.

[12] B. K. Bose, "Global energy scenario and impact of power electronics in 21st centurary," *IEEE Transactions on Industrial Electronics*, vol. 60, no. 7, pp. 2638 - 2651, Jul. 2013.

[13] B. K. Bose, "Power electronics and motor drives: recent progress and perspective," *IEEE Transactions on Industrial Electronics*, vol. 56, no. 2, pp. 581 - 588, Feb. 2009.

[14] B. K. Bose, *Modern power electronics and ac drives*, Pearson Education Inc., NJ, 2002

[15] B. K. Bose, "Scalar decoupled control of induction motor," *IEEE Transactions on Industry Applications*, vol. IA-20, no. 1, pp. 216 – 225, Jan. / Feb. 1984.

[16] K. Hasse, "Zur dynamik drehzahlgeregelter antriebe mit stromrichtergespeisten asynchron-kurzschlublauferm-aschinen," Darmstadt, Techn. Hochsch., Diss., 1969

[17] F. Blaschke, "The principle of field orientation as applied to the new transvector closed loop control system for rotating field machines," Siemens Review, vol. 34, pp. 217 – 220, May 1972

[18] I. Boldea and S. A. Nasar, *Vector control of ac drives*, CRC Press, NY, 1992.

[19] W. Leonhard, *Control of electrical drives*, 3rd ed., Springer, Berlin, 2001.

[20] G. S. Buja and M. P. Kazmierkowski, "Direct torque control of PWM inverter-fed AC motors—A survey," *IEEE Transactions on Industrial Electronics*, vol. 51, no. 4, pp. 744–757, Aug. 2004.

[21] J. N. Nash, "Direct torque control, induction motor vector control without an encoder," *IEEE Transactions on Industry Applications*, vol. 33, no. 2, pp. 333 – 341, Mar. / Apr. 1997.

[22] D. Telford, M. W. Dunnigan, and B. W. Williams, "A comparison of vector control and direct torque control of an induction machine," *IEEE Power Electronics Specialists Conference (PESC)*, vol. 1, pp. 421 – 426, 2000.

[23] D. Casadei, F. Profumo, and A. Tani, "FOC and DTC: two viable schemes for induction motors torque control," *IEEE Transactions on Power Electronics*, vol. 17, no. 5, pp. 779 – 787, Sept. 2002.

[24] D. de Almeida Souza, W. C. P. de Aragao Filho, and G. C. D. Sousa, "Adaptive fuzzy controller for efficiency optimization of induction motors," *IEEE Transactions on Industrial Electronics*, vol. 54, no. 4, pp. 2157–2164, Aug. 2007.

[25] "EMTP Theory Book," [Online]. Available: http://www.google.com/url?sa=t&rct=j&q=&esrc=s&source=web&cd=1&sqi=2&ved=0CB4QFjAA&url=http%3A%2F%2Fwww.dee.ufrj.br%2FTransm_Energia%2FArquivos%2FEMTPTB.PDF&ei=gl-5VJ7dMc3xoATn0YHgAw&usg=AFQjCNHORnv6sWT0rAVNYyJqbnwlcMoVTg&bvm=bv.83829542,d.cGU

[26] "User's Guide on the Use of PSCAD," ver. 4.2.1, Manitoba HVDC Research Centre, Feb. 2010.

[27] "PLECS User Manual," ver. 3.3, Plexim, 2012.

[28] N. Mohan, T. M. Undeland, and W. P. Robbins, *Power electronics converters, applications, and design*, 3rd ed., Wiley, NJ, 2002.

[29] H. Garnier and L. Wang, *Identification of continuous-time models from sampled data*, Springer-Verlag, London, 2008.

[30] C. Concordia and S. Ihara, "Load representation in power system stability studies," *IEEE Transactions on Power Systems*, vol. PAS-101, no. 4, pp. 969 - 976, Apr. 1982.

[31] D. Kosterev and A. Meklin, "Load modeling in WECC," in *Proceedings of IEEE PES Power Systems Conference and Exposition*, Oct. 2006, pp. 576 – 581.

[32] D. Kosterev, A. Meklin , J. Undrill, B. Lesieutre, W. Price, D. Chassin, R. Bravo, S. Yang, "Load modeling in power system studies," in *Proceedings of IEEE PES General Meeting*, Jul. 2008, pp. 1 – 8.

[33] A. M. Stankovic, B. C. Lesieutre, and T. Aydin, "Modeling and analysis of single-phase induction machines with dynamic phasors," *IEEE Transactions on Power Systems*, vol. 14, no. 1, pp. 9–14, Feb. 1999.

[34] B. Lesieutre, D. Kosterev, and J. Undrill, "Phasor modeling approach for single phase A/C motors," in *Proceedings of IEEE PES General Meeting*, Jul. 2008, pp. 1–7.

[35] R. Bravo, R. Yinger, D. Chassin, H. Huang, N. Lu, I. Hiskens, and G. Venkataramanan, Final Project Report Load Modeling Transmission Research, Lawrence Berkeley National Laboratory (LBNL), Mar. 2010.

[36] Y. Liu and V. Vittal, "Distribution side mitigation strategy for fault induced delayed voltage recovery," in *Proceedings of IEEE PES General Meeting*, Jul. 2014, pp. 1 – 5.

[37] C.U. Ogbuka and M.U. Agu, "A modified closed loop V/f controlled induction motor drive," *Pacific Journal of Science and Technology*, vol. 10, no. 1, May 2009.

[38] K. Rajashekara, A. Kawamura, and K. Matsuse, *Sensorless control of ac drives*, IEEE Press, NY, 1996.

[39] C. Schauder, "Adaptive speed identification for vector control of induction motors without rotational transducers," *IEEE Transactions on Industry Applications*, vol. 28, no. 5, pp. 1054 – 1061, Sep. / Oct. 1992.

[40] Y. R. Kim, S. K. Sul, and M. H. Park, "Speed sensorless vector control of induction motor using extended Kalman filter," *IEEE Transactions on Industry Applications*, vol. 30, no. 5, pp. 1225 – 1233, Sep. / Oct. 1994.

[41] X. Xu, R. De Doncker, and D. W. Novotny, "A stator flux oriented induction machine drive," in *Proceedings of IEEE Power Electronics Specialists Conference*, pp. 870 – 876, 1988.

[42] I. Takahashi and T. Noguchi, "A new quick response and high efficiency control strategy of an induction motor*," IEEE Transactions on Industrial Application*, vol. 22, no. 5, pp. 820 – 827, Sept. / Oct. 1986.

[43] K. J. Astrom, "Theory and applications of adaptive control – a survey," *Automata*, vol. 19, pp. 471 – 486, Sept. 1983.

[44] M. Azab, "Decoupled control of active and reactive power for three phase PWM rectifiers," *International Conference on Electrical, Electronic and Computer Engineering*, pp. 901 – 904, Sept. 2004.

[45] M. Malinowski, M. Jasinski, and M. P. Kazmierkowski, "Simple direct power control of three-phase PWM rectifier using space-vector modulation (DPC-SVM)," *IEEE Transactions on Industrial Electronics*, vol. 51, no. 2, pp. 447 – 454, Apr. 2004.

[46] P. C. Krause, O. Wasynczuk, and S. D. Sudhoff, *Analysis of electric machinery and drive systems*, 2nd ed., IEEE Press, NJ, 2002.

[47] P. M. Anderson and A. A. Fouad, *Power system control and stability*, 2nd ed., IEEE Press, NJ, 2003.

[48] G. C. Hsieh and J. C. Hung, "Phase-locked loop techniques – a survey," *IEEE Transactions on Industrial Electronics*, vol. 43, no. 6, pp. 609 – 615, Dec. 1996.

[49] B. Wu, *High power converters and ac drives*, Wiley, NJ, 2006.

[50] A. V. Oppenheim, A. S. Willsky, and S. H. Nawab, *Signals and Systems*, 2nd ed., Prentice Hall, 1996.

[51] R. Pintelon, P. Guillaume, Y. Rolain, J. Schoukens, and H. Van hamme, "Parametric identifcation of transfer functions in the frequency domain – a survey," *IEEE Transactions on Automatic Control*, vol. 39, no. 11, pp. 2245 – 2260, Nov. 1994.

[52] H. Garnier, M. Mensler, and A. Richard, "Continuous-time model identification from sampled data: implementation issues and performance Evaluation," *International Journal of Control*, vol. 76, no. 13, pp. 1337 – 1357, May 2003.

[53] L. Ljung, Experiments with identification of continuous time models, Technical report, *Accepted for publication in 15th IFAC Symposium on System Identification*, May 2009.

[54] J. Gillberg and L. Ljung, "Frequency domain identification of continuous-time output error models, part I: uniformly sampled data and frequency function approximation," *Journal of the International Federation of Automatic Control (JIFAC)*, vol. 46, no. 1, pp. 1 – 10, Jan. 2010.

[55] J. D. Glover, M. S. Sarma, and T. J. Overbye, *Power system analysis and design*, 4th ed., Thomson Learning, 2008.

[56] "Matlab User Manual," [Online]. Available: http://www.mathworks.com/.

[57] M. Klein, G. J. Rogers, and P. Kundur, "A fundamental study of inter-area oscillations in power systems," *IEEE Trans. Power Syst.*, vol. 6, no. 3, pp. 914 - 921, Aug. 1991.

APPENDIX A

PARAMETERS USED IN THE RESEARCH

Table A.0.1 Parameters of Drive System for Simulations in Section 3.7

Rating of the drive
Rated power: 25 MVA, rated terminal voltage: 13.8 kV
dc-link reference voltage: 26.5 kV (rated modulation index: 0.85)
Line-side rectifier controllers
Line resistance $R_{src} = 0.015\ pu$, inductance $L_{src} = 0.03\ pu$
Line-side currents controllers $K_p = 0.016\ pu$, $K_i = 3.0\ s^{-1}$
dc-link voltage controller $K_p = 5.3\ pu$, capacitance $C_{dc} = 34.82\ mF$
Driven induction motor (single-cage)
Stator and rotor resistances $R_s = 0.013\ pu$, $R_r = 0.009\ pu$
Stator and rotor leakage inductances $L_{ls} = 0.107\ pu$, $L_{lr} = 0.098\ pu$
Mutual inductance $L_m = 2.0\ pu$, Inertia $J = 2H = 1.5\ s$
(Converted to PSLF MOTOR1 parameters format): $R_a = 0.013\ pu$, $L_l = 0.107\ pu$, $L_s = 2.107\ pu$, $L_{pp} = L_p = 0.2004\ pu$ $T_{p0} = 0.6183\ s$, $T_{pp0} = 0.0\ s$, $H = 0.75\ s$, $D = 2.0\ pu$
Machine-side inverter controllers
Rotor flux controller $K_p = 6.183\ pu$, $K_i = 10.0\ s^{-1}$
Stator currents controllers $K_p = 0.106\ pu$, $K_i = 2.6\ s^{-1}$
Speed controller $K_p = 0.0796\ s$

Note: the parameters of the driven induction motor are per-unitized based on the rated power and rated terminal voltage of the drive

Table A.0.2 Parameters of the Drive System for Chapter 4

Rating of the drive
Rated power: 25 MVA, rated terminal voltage: 13.8 kV
dc-link reference voltage: 26.5 kV (rated modulation index: 0.85)
Line-side rectifier controllers
Line resistance $R_{src} = 0.015\ pu$, inductance $L_{src} = 0.03\ pu$
Line-side currents controllers $K_p = 0.016\ pu$, $K_i = 3.0\ s^{-1}$
dc-link voltage controller $K_p = 5.3\ pu$, capacitance $C_{dc} = 34.82\ mF$
Driven induction motor (single-cage)
Stator and rotor resistances $R_s = 0.013\ pu$, $R_r = 0.009\ pu$
Stator and rotor leakage inductances $L_{ls} = 0.107\ pu$, $L_{lr} = 0.098\ pu$
Mutual inductance $L_m = 2.0\ pu$, Inertia $J = 2H = 1.5\ s$
(Converted to PSLF MOTOR1 parameters format): $R_a = 0.013\ pu$, $L_l = 0.107\ pu$, $L_s = 2.107\ pu$, $L_{pp} = L_p = 0.2004\ pu$ $T_{p0} = 0.6183\ s$, $T_{pp0} = 0.0\ s$, $H = 0.75\ s$, $D = 2.0\ pu$
Machine-side inverter controllers
Rotor flux controller $K_p = 6.183\ pu$, $K_i = 10.0\ s^{-1}$
Stator currents controllers $K_p = 0.106\ pu$, $K_i = 2.6\ s^{-1}$
Speed controller $K_p = 0.0796\ s$

Note: the parameters of the driven induction motor are per-unitized based on the rated power and rated terminal voltage of the drive

Table A.0.3 Dynamic Data for the Two-Area Power System in Section 4.6

Generator (GENROU)			
d-axis transient rotor time constant T_{pdo}	8.0 s	*d*-axis sub-transient rotor time constant T_{ppdo}	0.03 s
q-axis transient rotor time constant T_{pqo}	0.4 s	*q*-axis sub-transient rotor time constant T_{ppqo}	0.05 s
Inertia constant *H*	13.0 s	Damping factor *D*	0.0 pu
d-axis synchronous reactance L_d	1.8 pu	*q*-axis synchronous reactance L_q	1.7 pu
d-axis transient reactance L_{pd}	0.3 pu	*q*-axis transient reactance L_{pq}	0.55 pu
d-axis sub-transient reactance L_{ppd}	0.25 pu	Stator leakage reactance L_l	0.2 pu
Saturation factor at 1 pu flux $S1$	0.05	Saturation factor at 1.2 pu flux $S12$	0.3
Stator resistance R_a	0.0025 pu		
Exciter (ESDC1A)			
Filter time constant T_r	0.05 s	Gain K_a	20.0
Time constant T_a	0.055 s	Lag time constant T_b	0.0 s
Lead time constant T_c	0.0 s	Maximum controller output V_{rmax}	1.0 pu
Minimum controller output V_{rmin}	-1.0 pu	Exciter field resistance line slope margin K_e	0.1 pu
Exciter time constant T_e	0.36 s	Rate feedback gain K_f	0.125
Rate feedback time constant T_f	1.8 s	Field voltage value *E1*	2.8
Saturation factor at *E1*	0.08	Field voltage value *E2*	3.7
Saturation factor at *E2*	0.33		
Governor (TGOV1)			
Permanent droop *R*	0.005 pu	Steam bowl time constant T_1	0.5 s
Maximum valve position	1.5 pu	Minimum valve position	0.0 pu
Numerator time constant T_2	3.0 s	Reheater time constant T_3	10.0 s
Turbine damping factor D_t	0.005 pu		

The frequency modulation as performed in Section 4.6.1 only considers 0.1 – 5.0 Hz frequency range. In this section, a broader modulation frequency range that covers 0.1 – 40.0 Hz is considered to explore the peak magnitude of the measured frequency magnitude response. This simulation is performed to identify the stability of the drive system in observation of constrained peaks on the bode magnitude plots. The same system as constructed in Section 4.6.1 is used. The simulation details are provided in Table A.0.4. The bode plots of the measured frequency response for the four transfer functions are presented in Figure A.0.1 through Figure A.0.4 in linear *x*- and *y*- axes ranges.

Table A.0.4 Simulation Details of Modulation for Broader Frequency Range

Modulation range	0.1 – 40.0 Hz
Modulation frequency increment	0.8 Hz
Amplitude of voltage perturbation	0.03 pu
Amplitude of frequency perturbation	0.02 pu
Rest interval (between frequencies)	10 s
Number of cycles for each modulated frequency	15

It can be observed from the simulation results that each bode magnitude plot has a peak value. The corresponding peak-magnitude frequencies are located between 10.0 Hz and 40.0 Hz. The simulation results verify that the system is stable considering the bode magnitude curve is not monotonically increasing as modulation frequency increases.

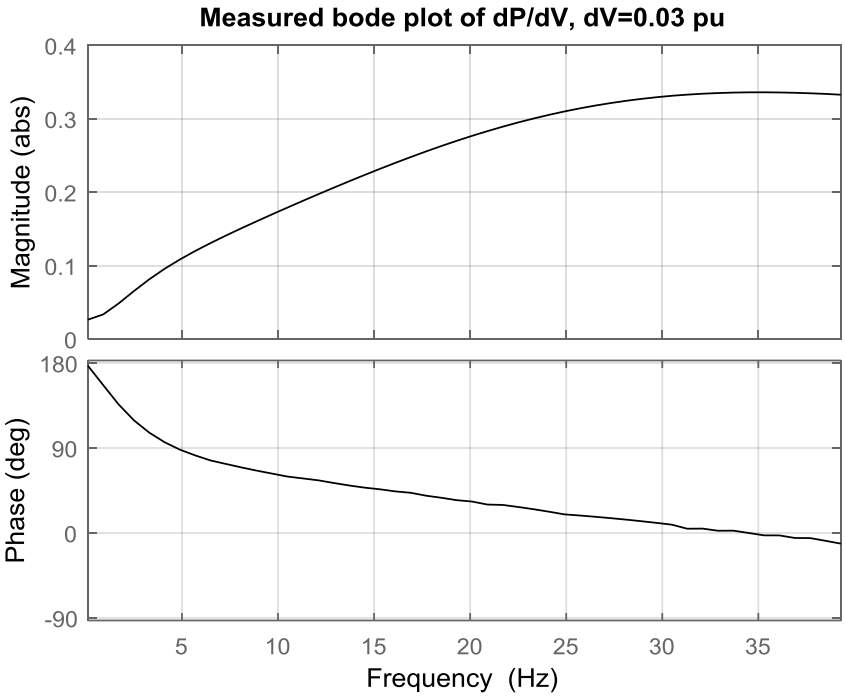

Figure A.0.1 Measured Bode Plot of *dP/dV* for 0.1 – 40.0 Hz Modulation

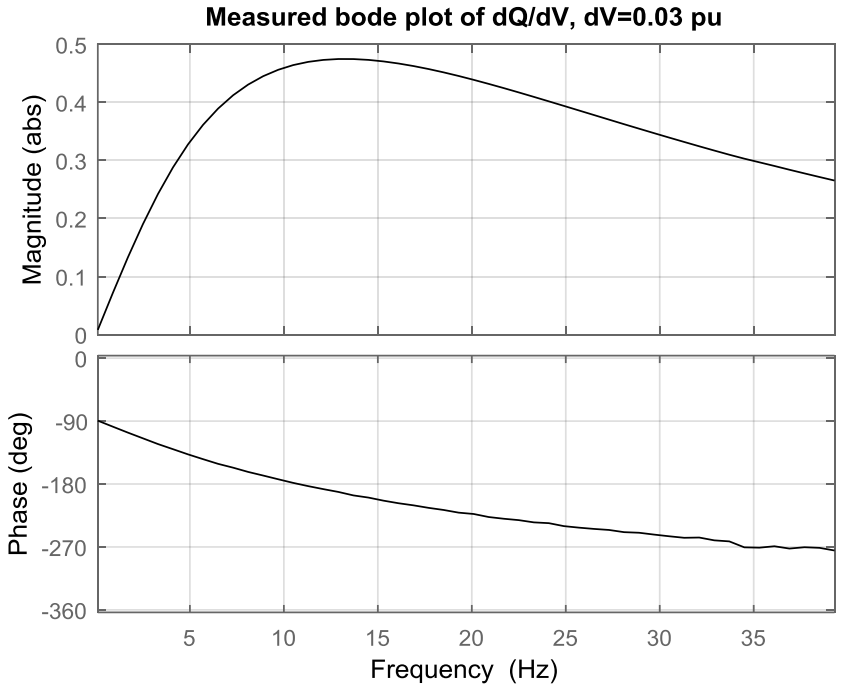

Figure A.0.2 Measured Bode Plot of *dQ/dV* for 0.1 – 40.0 Hz Modulation

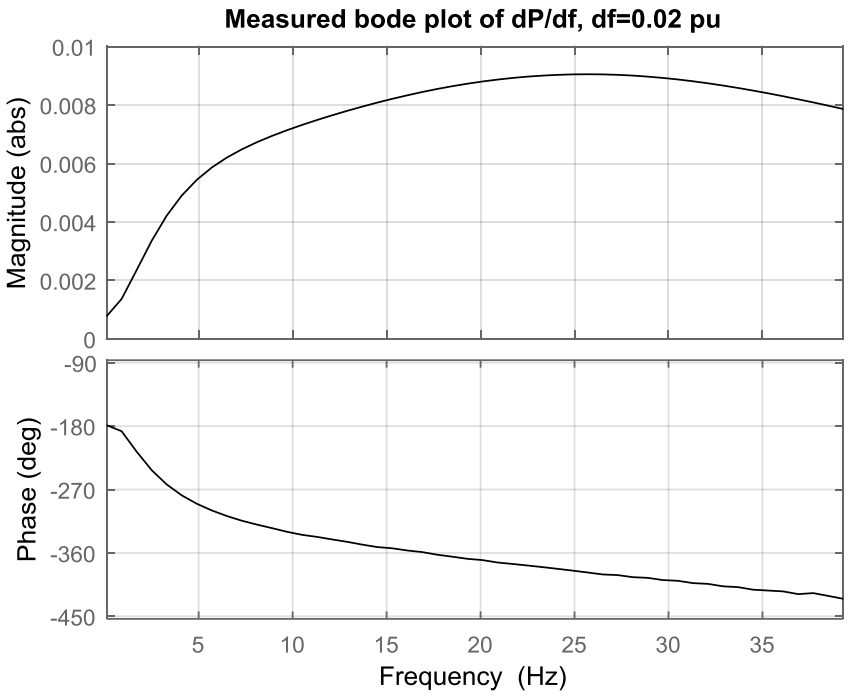

Figure A.0.3 Measured Bode Plot of *dP/df* for 0.1 – 40.0 Hz Modulation

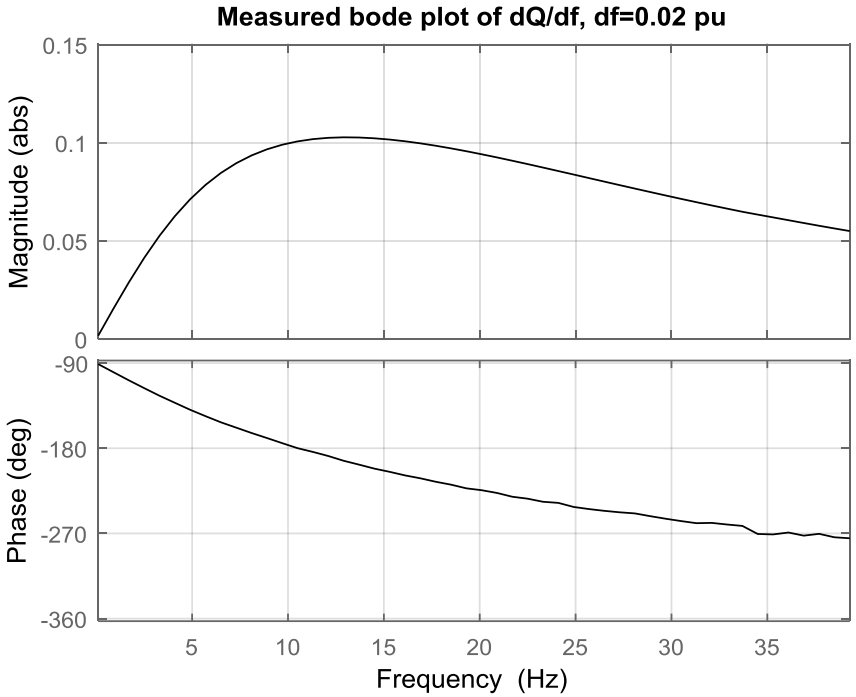

Figure A.0.4 Measured Bode Plot of *dQ/df* for 0.1 – 40.0 Hz Modulation

Table A.0.5 Parameters of the Drive System for Section 5.7.1

Rating of the drive
Rated power: 25 MVA, rated terminal voltage: 13.8 kV
dc-link reference voltage: 26.5 kV (1.92 pu, if normalized on the basis of the rated terminal voltage, which yields 0.85 rated modulation index)
Line-side rectifier controllers
Line resistance $R_{src} = 0.03\ pu$, inductance $L_{src} = 0.03\ pu$
Line-side currents controllers $K_p = 0.00252\ pu$, $K_i = 1.2\ s^{-1}$
dc-link voltage controller $K_p = 0.884\ pu$, capacitance $C_{dc} = 34.82\ mF$
Driven induction motor (single-cage)
Stator and rotor resistances $R_s = 0.013\ pu$, $R_r = 0.009\ pu$
Stator and rotor leakage inductances $L_{ls} = 0.107\ pu$, $L_{lr} = 0.098\ pu$
Mutual inductance $L_m = 2.0\ pu$, Inertia $J = 2H = 1.5\ s$
(Converted to PSLF MOTOR1 parameters format): $R_a = 0.013\ pu$, $L_l = 0.107\ pu$, $L_s = 2.107\ pu$, $L_{pp} = L_p = 0.2004\ pu$ $T_{p0} = 0.6183\ s$, $T_{pp0} = 0.0\ s$, $H = 0.75\ s$, $D = 2.0\ pu$
Machine-side inverter controllers
Rotor flux controller $K_p = 6.183\ pu$, $K_i = 10.0\ s^{-1}$
Stator currents controllers $K_p = 0.106\ pu$, $K_i = 2.6\ s^{-1}$
Speed controller $K_p = 0.0796\ s$

Note: the parameters of the driven induction motor are per-unitized based on the rated power and rated terminal voltage of the drive

Table A.0.6 Parameter of the Drive System for Section 5.7.2

Rating of the drive
Rated power: 25 MVA, rated terminal voltage: 13.8 kV
dc-link reference voltage: 26.5 kV (1.92 pu, if normalized on the basis of the rated terminal voltage, which yields 0.85 rated modulation index)
Line-side rectifier controllers
Line resistance $R_{src} = 0.03\ pu$, inductance $L_{src} = 0.03\ pu$
Line-side *d*-axis current controllers $K_p = 0.00252\ pu$, $K_i = 1.2\ s^{-1}$
Line-side *q*-axis current controllers $K_p = 0.05\ pu$, $K_i = 24.0\ s^{-1}$
dc-link voltage controller $K_p = 0.884\ pu$, capacitance $C_{dc} = 34.82\ mF$
Driven induction motor (single-cage)
Stator and rotor resistances $R_s = 0.013\ pu$, $R_r = 0.009\ pu$
Stator and rotor leakage inductances $L_{ls} = 0.107\ pu$, $L_{lr} = 0.098\ pu$
Mutual inductance $L_m = 2.0\ pu$, Inertia $J = 2H = 1.5\ s$
(Converted to PSLF MOTOR1 parameters format): $R_a = 0.013\ pu$, $L_l = 0.107\ pu$, $L_s = 2.107\ pu$, $L_{pp} = L_p = 0.2004\ pu$ $T_{p0} = 0.6183\ s$, $T_{pp0} = 0.0\ s$, $H = 0.75\ s$, $D = 2.0\ pu$
Machine-side inverter controllers
Rotor flux controller $K_p = 6.183\ pu$, $K_i = 10.0\ s^{-1}$
Stator currents controllers $K_p = 0.106\ pu$, $K_i = 2.6\ s^{-1}$
Speed controller $K_p = 0.0796\ s$

Note: the parameters of the driven induction motor are per-unitized based on the rated power and rated terminal voltage of the drive

Table A.0.7 Parameters Used in Section 5.8

Drive Load:
Line-side rectifier controllers
Line resistance $R_{src} = 0.03\ pu$, inductance $L_{src} = \ 0.03\ pu$
Line-side currents controllers $K_p = 0.0126\ pu$, $K_i = 6.0\ s^{-1}$
dc-link voltage controller $K_p = 2.0\ pu$
Driven induction motor (single-cage)
Stator and rotor resistances $R_s = 0.013\ pu$, $R_r = 0.009\ pu$
Stator and rotor leakage inductances $L_{ls} = 0.107\ pu$, $L_{lr} = 0.098\ pu$
Mutual inductance $L_m = 2.0\ pu$, Inertia $J = 2H = 1.5\ s$
(Converted to PSLF MOTOR1 parameters format): $R_a = 0.013\ pu$, $L_l = 0.107\ pu$, $L_s = 2.107\ pu$, $L_{pp} = L_p = 0.2004\ pu$ $T_{p0} = 0.6183\ s$, $T_{pp0} = 0.0\ s$, $H = 0.75\ s$, $D = 2.0\ pu$
Machine-side inverter controllers
Rotor flux controller $K_p = 6.183\ pu$, $K_i = 10.0\ s^{-1}$
Stator currents controllers $K_p = 0.106\ pu$, $K_i = 2.6\ s^{-1}$
Speed controller $K_p = 0.0796\ s$
Motor Load (PSLF MOTOR1 model):
$R_a = 0.02\ pu$, $L_l = 0.12\ pu$, $L_s = 3.5\ pu$, $L_p = 0.19\ pu$, $L_{pp} = 0.165\ pu$ $T_{p0} = 1.83\ s$, $T_{pp0} = 0.02\ s$, $H = 0.9\ s$, $D = 2.0\ pu$, $Se_1 = 0.01$, $Se_1 = 0.1$

Table A.0.8 Parameters Used in Section 5.9

Drive Load:
Line-side rectifier controllers
Line resistance $R_{src} = 0.03\ pu$, inductance $L_{src} = \ 0.03\ pu$
Line-side currents controllers $K_p = 0.0126\ pu$, $K_i = 6.0\ s^{-1}$
dc-link voltage controller $K_p = 2.0\ pu$
Terminal voltage regulator $K_p = 1.3\ pu$, $K_i = 0.01\ s^{-1}$
Driven induction motor (single-cage)
Stator and rotor resistances $R_s = 0.013\ pu$, $R_r = 0.009\ pu$
Stator and rotor leakage inductances $L_{ls} = 0.107\ pu$, $L_{lr} = 0.098\ pu$
Mutual inductance $L_m = 2.0\ pu$, Inertia $J = 2H = 1.5\ s$
(Converted to PSLF MOTOR1 parameters format): $R_a = 0.013\ pu$, $L_l = 0.107\ pu$, $L_s = 2.107\ pu$, $L_{pp} = L_p = 0.2004\ pu$ $T_{p0} = 0.6183\ s$, $T_{pp0} = 0.0\ s$, $H = 0.75\ s$, $D = 2.0\ pu$
Machine-side inverter controllers
Rotor flux controller $K_p = 6.183\ pu$, $K_i = 10.0\ s^{-1}$
Stator currents controllers $K_p = 0.106\ pu$, $K_i = 2.6\ s^{-1}$
Speed controller $K_p = 0.0796\ s$
Motor Load (PSLF MOTOR1 model):
$R_a = 0.013\ pu$, $L_l = 0.107\ pu$, $L_s = 2.107\ pu$, $L_{pp} = L_p = 0.2004\ pu$ $T_{p0} = 0.6183\ s$, $T_{pp0} = 0.0\ s$, $H = 0.75\ s$, $D = 2.0\ pu$